8-2011

Understanding the Role of a Bio-Inspired Surface Modification for Delayed Icing

Clayton Schenk
University of Arkansas, Fayetteville

Understanding the Role of a Bio-Inspired Surface Modification for Delayed Icing

Understanding the Role of a Bio-Inspired Surface Modification for Delayed Icing

A thesis submitted in partial fulfillment
of the requirements for the degree of
Master of Science in Microelectronics and Photonics

By

Clayton Schenk
Southeast Missouri State University
Bachelor of Science in Engineering Physics: Applied Physics, 2009

August 2011
University of Arkansas

Abstract

Atmospheric icing event is problematic for outdoor structures because it can damage, slow, impede, and danger general routine. For a wind turbine blade, it can damage, disrupt movement, and cause potentially dangerous ice throw. Anti-icing based on a surface texture is advantageous due to the low cost of maintenance and there is no additional requirement of energy output for preventing the icing problem. This work is based on the biomimicry of the superhydrophobic nature of the lotus leaf, whereas the limited wettability supports the water to flow freely from the surface structure. The phenomenon is based on a morphology and composition of the micro-nano scale hierarchical surface features: papilla, micro-pillars, coated in wax nanostructures.

The objective of this research is the creation and testing of a surface texture, similar to the lotus formed onto the surface structure of polyurethane coatings. The hypothesis is that a micron size surface texture will prevent the water from penetrating the surface features based on the water's surface tension. Also, it is hypothesized that due to the decreased wetting contact between the water and surface, there is a delay in the time for the water to freeze.

The thesis objective was realized through a soft lithography imprinting of a surface texture from a created template. A short timed acid texture created the additional submicron-nanostructure on the surface, resulting in a coating modification with similar structure to the lotus. Characterizations of the coatings were performed using Contact Angle Measurements (CAM), Atomic Force Microscopy (AFM), Scanning Electron Microscopy (SEM), Optical Microscopy (OM) and Surface Profilometer (SP).

The textured polyurethane surfaces showed an increase of the water contact angles as compared to the non-textured surfaces. The air trapped within the surface texture forced the water to bead-up on top of the surface structures. The texture surfaces gave a decrease in the ice to surface contact area consequently resulting in the delayed icing mechanism.

This thesis is approved for recommendation
to the Graduate Council.

Thesis Director:

_____
Dr. Ajay Malshe

Thesis Committee:

_____
Dr. Min Zou

_____
Dr. Z. Ryan Tian

_____
Prof. Ken Vickers *(ex offico)*

The following signatories attest that all software used in this thesis was legally licensed for use by Mr. Clayton Schenk for research purposes and publication.

_____	_____
Mr. Clayton Schenk	Dr. Ajay Malshe

This thesis was submitted to http://www.turnitin.com for plagiarism review by the TurnItIn company's software. The signatories have examined the report on this thesis that was returned by TurnItIn and attest that, in their opinion, the items highlighted by the software are incidental to common usage and are not plagiarized material.

_____	_____
Mr. Ken Vickers	Dr. Ajay Malshe

Thesis Duplication Release

I hereby authorize the University of Arkansas Libraries to duplicate this thesis when needed for research and/or scholarship.

Agreed_____
Clayton Schenk

Refused_____

Acknowledgements

I would first like to thank my major research advisor, Dr. Ajay Malshe, for words of wisdom throughout the cycle of the research project. The advice and conversations led me to think differently over the course of my time at the University of Arkansas. I am very fortunate to have the chance to work at the Materials and Manufacturing Research Laboratories (MMRL) and have the research funding available for the completion of this thesis. I would also like to thank my committee members Dr. Min Zou and Dr. Z. Ryan Tian for their support in my research efforts.

I am grateful for all the help and support I have had to complete this thesis. I would like to thank Dr. Anoop Samant for insightful conversations and help with research questions, Dr. Min Zou for the Goniometer usage, Drew Fleming for taking the time to help me learn the contact angle measurements, Corey Thompson for help with AFM work, Braden Harbin for the helpful suggestion of releasing agents, Josh Wilson for the financial and administration assistance, Dr. Vishwas Bedekar for the useful computer drawings and the microEP department and MMRL group for their advice and support.

A special thanks to Professor Ken Vickers for the funding, advisement and life training that will complement well with my educational skills. I am thankful for all the work Renee Jones-Hearon has done to ensure I graduate on time and that the necessary documents were completed.

Part of this research is possible through the help of Errol Porter, facilities manager, High Density Electronics Center at the University of Arkansas, Fayetteville campus, for teaching me the functions of the photolithography and DRIE procedures. As well, part of this research is possible through the help of Mourad Benamara, electron

microscopy facility manager, Institute for Nanoscale Materials Science and Engineering, University of Arkansas, Fayetteville campus, for helping me in ESEM images.

I would like to thank my family and friends for their encouragement throughout my education. I appreciate their undying support. I am grateful to my parents, Ronald and Donna Schenk for guiding me on this path in life. I am indebted to Melinda Vivian, through much encouragement and love, you have made everything else easy on me.

This program is financially supported in part by the National Science Foundation's Scholarships in Science, Technology, Engineering and Math (S-STEM) under Grant No. DUE-0728636. Any opinions, findings and conclusions or recommendations expressed in this material are those of the author and do not necessarily reflect the views of the National Science Foundation.

Table of Contents

List of Figures

List of Tables

Nomenclature

Polyurethane: PU

Deep Reactive Ion Etch: DRIE

Dichlorodimethylsilane: DMDCS

Trichloromethylsilane: TCMS

Nitric Acid: HNO_3

Contact Angle: CA

Water Contact Angle: WCA

Contact Angle Measurement: CAM

Scanning Electron Microscope: SEM

Atomic Force Microscope: AFM

Optical Microscope: OM

Surface Profilometer: SP

Chapter 1: Introduction

1.1 Appeal of Wind Power

Wind power is attractive because it is a renewable source of energy. Wind farms can contain hundreds of turbines each producing megawatts of power [1]. In 2009, wind power was the highest installed renewable energy source at 38 GW worldwide. The increase in 2009 factored into the existing wind generation totaling 159 GW worldwide. The 24% increase in 2009 proves the increase in demand from the economic and global market for clean renewable energy sources. Wind capacity only trails hydropower in existing renewable technologies. A comparison was made in Table 1.1 between the new and existing power capacities in 2009 [2]. Furthermore, a study shown in Figure 1.1 A was conducted comparing the power capacities of nuclear, fossil fuel and renewable energy sources. Renewable energy maintained 26% of the world capacity. For new capacities added in 2009, Figure 1.1 B shows that 47% of new energy capacity added in 2009 was renewable energy [2]. The increase in wind power is primarily due to the innovation of the new high capacity wind farms. Figure 1.2 images the immense size; blades typically 50-70 meters long [3].

Table 1.1. Comparison of renewable energy added and existing in 2009 [2].

Power Generation	Added During 2009 (GW)	Existing at end of 2009 (GW)
Wind	38	159
Solar	7	21
Hydro	31	980
Geothermal	0.4	11
Biomass	2-4	54
Ocean	≈ 0	0.3

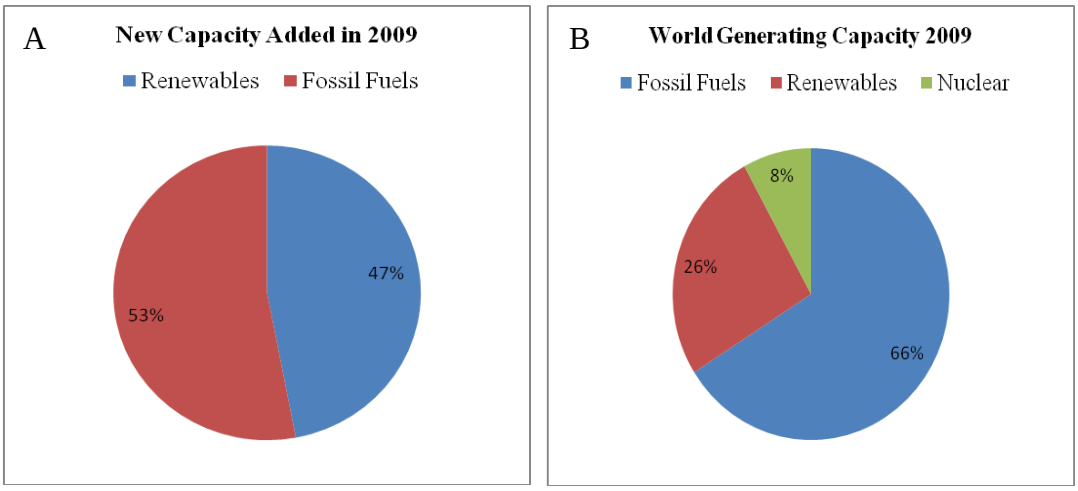

Figure 1.1. A. New capacity added in 2009. B. World generating capacity in 2009 [2].

Figure 1.2. Wind turbines of New York State [4].

1.2 Explanation of Blade Dynamics

Wind turbine blades are built to have a lightweight aerodynamic shape designed for improved efficiency. The structure is made of composite fiberglass or carbon fiber reinforced epoxies for lightweight strength. Low density wood such as Balsa is built into the blade for structural integrity. High quality polyurethane (PU) coating is used to form a protective coating on the blades' surface. Integrated together, the blade is expected to perform for a life span of at least 20 years [5, 6, 7].

The windfoil is the wind flow around the turbine blade. The curvature of the blade interacts with the windfoil in such a way to create lift (force) which turns the blade in a circular motion. The blades' design is for a smooth laminar flow of air around the blade. A disruption of this flow is problematic in that the forces that create the motion are destroyed, which cause a turbine to stall. Figure 1.3 describes the windfoil around the turbine blade and represents the lift from the cross section of the blade [8, 9].

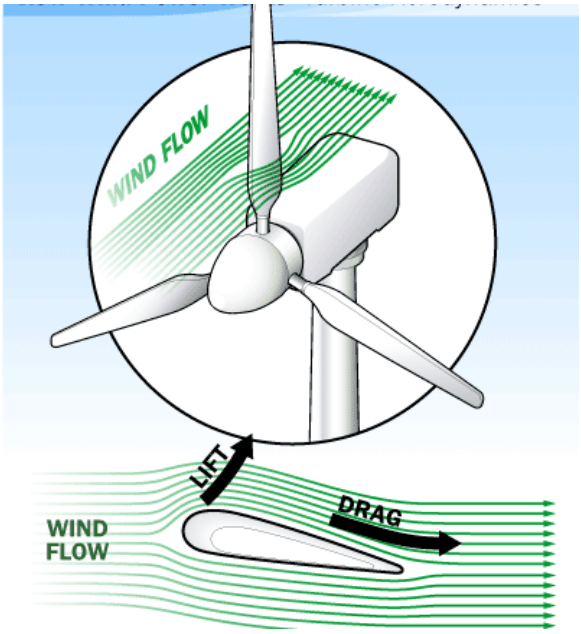

Figure 1.3. Flow of air around a wind turbine blade cross section [9, 10].

The working of a turbine is represented in Figure 1.4. The wind causes the blades to rotate about a center of axis from the lift created. The nacelle is the center hub in which the power is transformed. The input rotation mechanical energy is converted into the output electrical energy. The central axis shaft (Figure 1.4 label C) is connected to the gearbox (Figure 1.4 label D) transforming the rotation into a higher speed constant rotation (depending on the turbine size). The rotation is transformed into electrical energy via the generator (Figure 1.4 label G). The generator works by the rotation of a magnet inside a series of coils; this rotations produces current from the change in magnetic flux induced within these coils [8, 10]. The current produced in these coils is the created output of electrical energy.

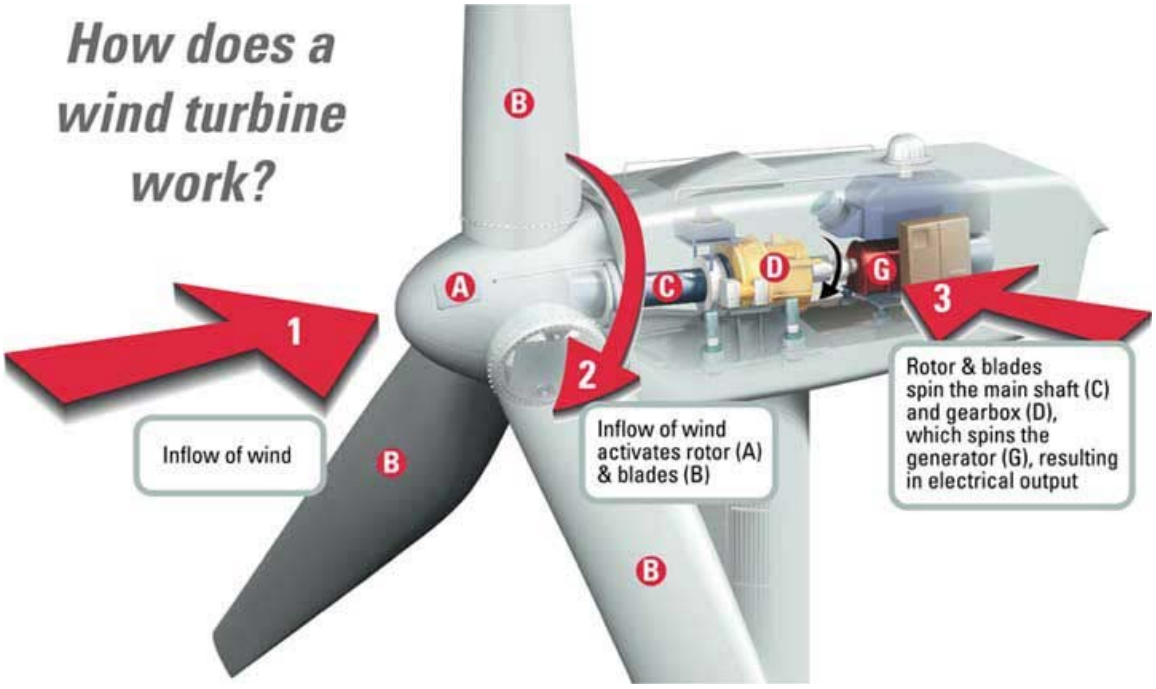

Figure 1.4. Wind turbine power generation [10, 11].

1.3 Existing and New Methods for Industrial Coatings

The surface coatings are very important to the blade design because it is the first line of defense against weather phenomenon. Coatings must have a robust design to protect against damage from windblown debris to severe weather conditions. The current industrial standard for coating the blade is aliphatic PU. Application of the coating to the wind turbine blades is achieved through sprayable technology [11, 12]. PU is mixed as a two part urethane hardener composition as specified by the coating supply company during the spray process. Standard coating cure thickness is typically around 100μm [11]. The chemistry composition is explained in the materials Section 3.1 of this thesis.

1.4 Ice Formation on the Blade

There are limited locations in which wind turbines can be placed because of the need for a constant air flow. Among these locations, there is a greater potential to build the wind farms in colder climate, however there is some concern of potential weathering conditions. But new research shows there are more benefits than space and airflow in these regions, as wind power is approximately 10% higher in regions of cold climate because of the increased air density [13].

The problematic weathering condition that is identified is the formation of ice on the turbine blade (Figure 1.5). As the wind turbine rotates through the air, the leading edge of the blades surface comes into contact with the water in various atmospheric icing and wetting events. Depending on the conditions, the ice freezes onto the blades surface at initial impact or upon traveling on the surface. The ice build-up will diminish aerodynamic blade performance by changing the windfoil from a laminar flow to a

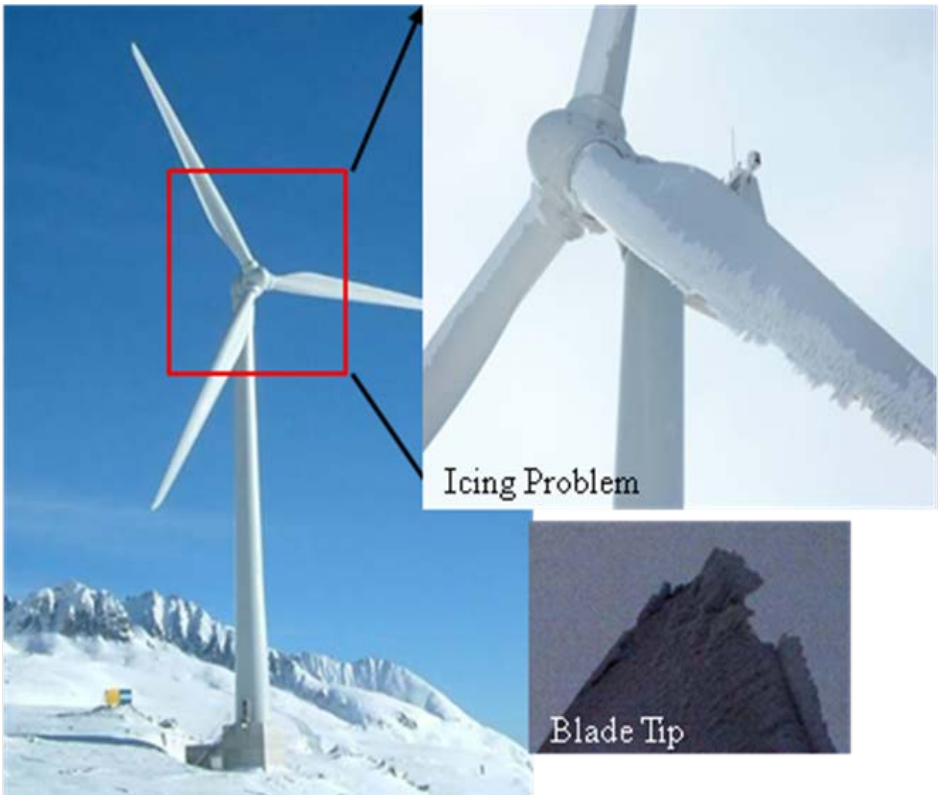

Figure 1.5. Wind turbine icing problem [14, 15]

turbulent one shown in Figure 1.6. This could result in the diminished power output as well as stall of a wind turbine. Ice mass has the potential to overload the blade increasing fatigue stress leading to mechanical failure. Problems also arise during the melting of the ice. As the ice melts, it becomes detached from the blade and can be tossed through the air landing several kilometers away, which creates a possibility for injury to people [16].

There are three particular weather events that can lead to this problem: in-cloud icing, freezing precipitation and frost [13]. For in cloud icing, soft rime icing event occurs when the temperature is well below 0°C having low density, low water content and adhesion. Hard rime has high density and is more difficult to remove because it has higher water content. Freezing precipitation includes glaze icing, when a portion does not freeze but runs along the surface and freezes later, and has very strong adhesion. Other precipitation events include: freezing rain which ice density and adhesion are high,

wet snow which is easy to remove at first but difficult once frozen. For frost, the classification is vapor solidification whereas it condenses and freezes directly on a cool surface [13]. The ideal solution to prevent or actively de-ice the wind turbine to avoid the problems associated with icing on the blades.

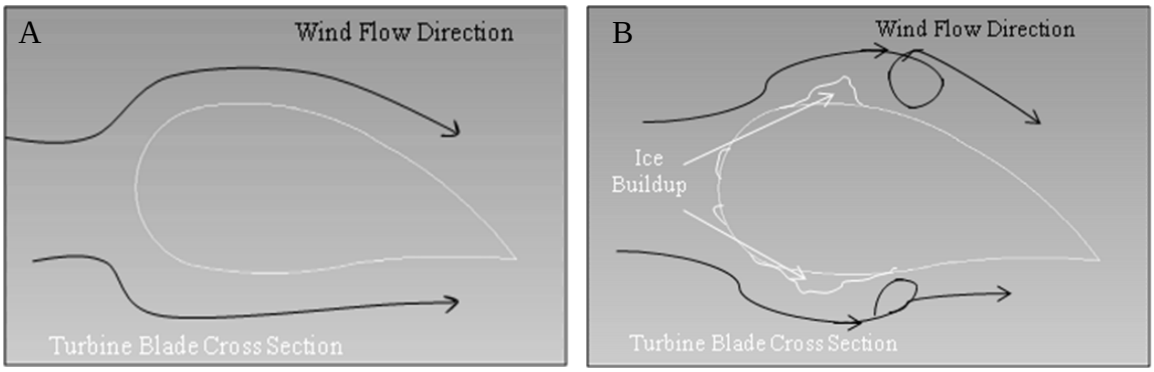

Figure 1.6. A. Laminar flow around the blade. B. Turbulent flow around the blade.

1.5 Preventive Techniques

Icing solutions are classified by two techniques: active and passive methods. Active methods involve addition of a form of energy to de-ice or prevent the formation of ice, anti-icing. Passive methods utilize unique surface properties of the blade to de-ice or anti-ice [13, 17].

Active methods include: an inflatable boot, electrical resistance heating, warm air flow through the inner structure and air flow through micron sized holes in the blades surface. With current technology development, the only active system that is being implemented is warm air flow through the blade and electrical resistance heating [13].

The inflatable boot is an attractive option due to the advanced technology developed for de-icing airplane wings. The design would enable a rubber boot on the surface to inflate and mechanically stress the ice, thus cracking and remove the ice

buildup on the surface [13]. This is unrealistic for a turbine blade because of the boots' lifespan, immense size and possible maintenance that would be required once installed.

Electrical resistance heating is researched as an option. By adding a conductive sheet design within the blade, passing a current through the conductive layer would result in joule heating to warm the blade [13, 18, 19]. Similar designs are observed on the rear windshields of vehicles. However, the system would require up to 14% of the total power generation under regular air flow to warm the blade during the icing occurrence [13].

Flowing warm air through the blade is a possible option for preventing ice formation. Circulating warm air from a base heater inside the nacelle through the length of the blade can warm the inside of the blade through convective heating. The interior passes the heat through conduction to the blades' surface. The effect will warm the exterior of the blade above the freezing temperature to prevent the ice from forming. However, the thickness of the blade will require on average 10-15% of the turbine's rated power output to circulate air necessary to de-ice the blades [14, 20, 21].

Air flow from the inner to outer blade structure through small holes is a unique concept. This hypothesized method solves the problem of heating the entire thickness of the blade via circulating air inside by engineering holes in which the air could pass through. The idea behind this solution is that the air flowing out of the blade will create an airflow pattern directing the water droplets from the surface. Furthermore, the air can be pulsating in order to remove the ice from the surface. More research is needed to bring the idea from concept to reality, and there is still the requirement on average of 10-15% of the turbine's rated power to circulate the air [22].

Passive methods include: specialized black paint coating, active pitching and novel surface engineering solutions. At the current stage of technology development none of the passive techniques are used in turbine design [13].

Black paint as the coating for the blade was conceptualized to harvest the energy from the sun to increase the temperature of the blade. Extra photons absorbed due to the larger band gap of the black color were the mechanism behind the idea. However, the idea seems to lack the foresight that during icing events there will be little or no sunlight [13].

Active pitching was used to mechanically shed the ice from the blades' surface. Sharp movement through power cycles in the blade was the methodology. There are few reports on the effectiveness and benefit from this method [13].

Novel surface engineering solutions, such as the one described in this thesis, is an area of increasing research and reality. To date, there are no truly icephobic surfaces or materials because of the complexity of the problem. There are several research publications on the superhydrophobicity for decreased contact area and ice adhesion, delayed freezing on micro/nano modified surfaces, low surface energy materials for decrease adhesion and ice prevention based on a nano roughness to prevent nucleation, discussed later in Chapter 2 [23-35]. More research testing must be realized before implementing a single method in order to determine manufacturing and product reliability, cost analysis, and testing under various icing conditions.

There are certain drawbacks to each of the current solutions for de-icing, anti-icing the wind turbine blades. The active systems require energy to work while passive

coating systems have not proved truly icephobic. The ideal case is to have a passive coating system to prevent ice formation.

1.6 Biomimetics

Biomimetics is the study and implementation of ideas imitating nature. The possibility to artificially create or reverse engineer the effects that nature has had millions of years to develop has become an area of high interest for economical and practical reasons [36, 37]. Several examples of nature inspired surfaces and their functions are represented in Figure 1.7: A water-strider uses micro/nano hair-like features on legs and the physics of surface tension to walk on water. Chinese researchers have created a similar surface on the bottom surface of mini-boats for high buoyancy [38]. A shark's skin uses micro/nano texture and aligned scales to glide through the water. Commercial products from Speedo can be purchased with the imitation design of a shark skin for the high-tech low drag swim wear [39]. A gecko uses super sticky nano hair-like projections and the physics of Van der Waals interaction to walk upside-down. Researchers at Berkley have commercialized Gecko-tape with extremely high pull off force that is inspired from the hair-like projections found on the Gecko [40]. A lotus leaf uses dual micro/nano projections and the physics of surface tension to propel water, beading it up on the surface [37]. In this thesis, the work imitates the surface structure of the lotus leaf for increased water repellence and ice formation delay.

By imitating the topography, the goal is to create functionality based on a surface modification. Creating a texture similar to the lotus leaf on a wind turbine blade could enable the water to roll off the surface before freezing. The surface texture design

A)

B)

C)

D)

Figure 1.7. A. Water Strider [41]. B. Shark [42]. C. Gecko [43]. D. Lotus Leaf [44].

produces less water to surface contact area because the water forms on top of the surface features. The water is so greatly repelled from the lotus leaf surface that it is deemed superhydrophobic, as is the goal to create onto the surface of the wind turbine blade.

1.7 Superhydrophobic Surfaces

The level of hydrophobicity is determined by the Water Contact Angle (WCA) to a solid surface. Water is strongly attracted to hydrophilic surfaces which have a WCA less than 90º. Hydrophobic surfaces repel water from the surface due to surface free energies and interaction at the interface creating a WCA greater than 90º. Highly hydrophobic surfaces are deemed superhydrophobic due to the increased WCA of greater than 150º [45-47]. This angle of contact is critical to understand how the droplet interacts between water to surface, which will help develop the interaction at the ice to solid interface.

The droplet Contact Angle (CA), θ, is governed by the surface free energies of the liquid vapor, γ_{lv}, solid vapor, γ_{sv}, and solid liquid interfaces, γ_{sl}. Young's State is the ideal case which finds the angle of contact to be a minimization of the energies at the interfaces described in Equation 1.1 [45-47]:

$$\cos\theta = \frac{\gamma_{sv} - \gamma_{sl}}{\gamma_{lv}} \qquad \text{(Equation 1.1)}$$

where the equation is theorized through the minimization of energy between the three phases present in the representation in Figure 1.8 A. Young's State does not account for the impact of surface roughness, swelling, dissolution or chemical heterogeneity [45-47]. Other models are used to factor in the surface roughness of the surface.

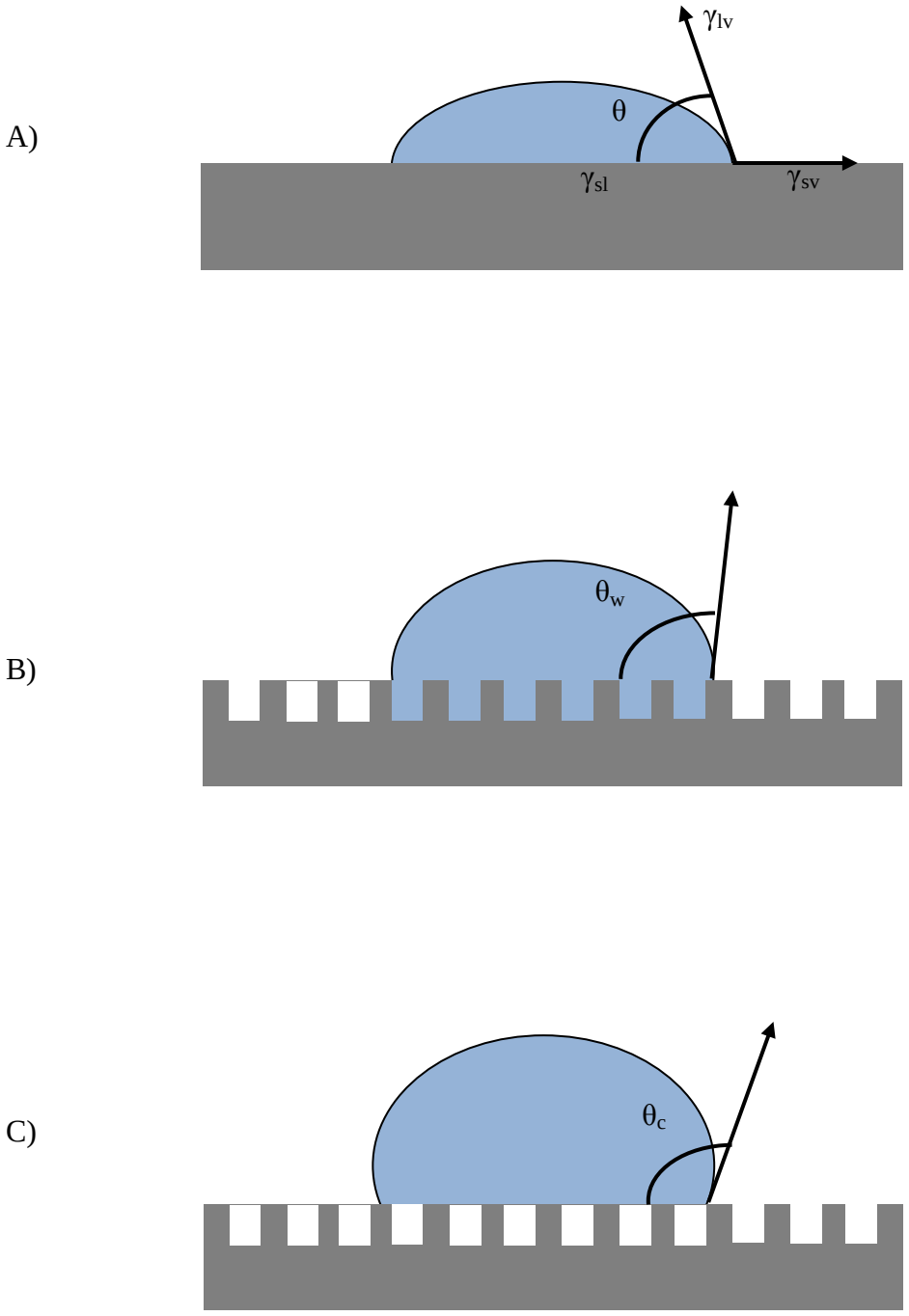

Figure 1.8. A. Water droplet in the ideal Young's State. B. Water droplet in the Wenzel State. C. Water droplet in the Cassie-Baxter State [45-47]

In the Wenzel State, seen in Figure 1.8 B, the water droplet completely penetrates the surface features of the solid. This creates more water to surface contact denoted by *r*, true surface area divided by apparent, in Equation 1.2 [45-47]:

$$\cos\theta_w = r\cos\theta \qquad \text{(Equation 1.2)}$$

where θ_w is the apparent contact angle on the rough surface and θ is the contact angle described by Young's State. Research shows that in the Wenzel State, wetting on a hydrophobic surface will yield a more hydrophobic surface or larger CA. On the other hand, a hydrophilic surface in the Wenzel State exhibits a more attractive surface yielding a lower CA [45-47].

In the Cassie-Baxter State (Figure 1.8 C), the water droplet is completely suspended on the tops of the surface features. This will completely trap a pocket of air within the surface features. The apparent contact angle, θ_c, is described in Equation 1.3 [45-47]:

$$\cos\theta_c = f_s\cos\theta_s + f_v\cos\theta_v \qquad \text{(Equation 1.3)}$$

where the Cassie-Baxter CA is a composite of the fraction and CA of the solid, f_s and θ_s, and fraction and CA of the vapor, f_v and θ_v. Water droplets sit on top of the surface structure when the force of surface tension is greater than that of gravity pushing the droplet into the surface features.

Superhydrophobicity is a highly researched area due to the anti-wetting and self cleaning properties. This research was based on mimicking the surface structure of the lotus leaf. The lotus owes its superhydrophobicity to the dual hierarchy of micro and nano-features on the surface. The lotus is covered in Papilla (micro pillars) with dimensions of 10-15 micron pitch, 8-12 micron height and 3-7 micron in diameter [48].

The Papilla are covered in wax nano-features completing the hierarchy and serving as the hydrophobic layer seen in Figure 1.7 D. The WCA of the lotus leaf (160º) will be the aim of the base surface in this research [46]. The unique properties of the Cassie-Baxter State realize from the lotus leaf allows the formulation of a research plan for the surface structure of a wind turbine blade.

1.8 Proposed Solution / Motivation and Hypothesis

The motivation behind this research was to prevent ice buildup on the blade of the wind turbine. Understanding the role of surface texture to create a superhydrophobic surface to delay ice accumulation was the methodology.

It was hypothesized that a micron size surface texture will prevent the water droplet from penetrating the surface features based on the surface tension of the droplet. The surface tension effects must outweigh the gravitational forces that tend to push the droplet into the surface texture. During the freeze process, the area of water contacting the surface can be decreased on the textured surface as compared to a flat surface, if the water is propelled in the Cassie-Baxter State. The increased time for the water to freeze was expected due to the decreased contact area with the surface. During cooling, the heat of conduction plays a critical role in cooling the water on the wind turbine blades' surface. Creation of a surface that forces the water into the Cassie-Baxter State should increase the ice freezing time by limiting heat of conduction [28]. Detailed explanations are giving in Chapters 2 and 4.

1.9 Objective of Thesis

The objective of this work was to create a dual micro-nano hierarchical surface texture similar to the lotus leaf on hydrophobic PU surface. This surface could be applied to wind turbine blades to decrease the wetting contact for water repellency and to delay the ice formation due to reduced area limiting cooling via heat conduction.

The specific objectives were:

1. Fabricate a surface texture similar to the Lotus Leaf onto a polyurethane surface.
2. Perform topography measurements through Atomic Force Microscopy (AFM), Scanning Electron Microscopy (SEM), Contact Angle Measurements (CAM), and Surface Profilometer Measurements (SPM).
3. Test WCA on the surface structure to fully understand the interfacial interaction and to describe the state the droplet is in.
4. Test ice formation on the various surfaces by characterizing the times for the water droplet to freeze onto the surface (static test).

This thesis is separated into five chapters. Chapter 1 gives a fundamental overview of wind turbine blades, coating mechanisms, problematic ice formation and possible solution in blades design, superhydrophobic structures and a possible way to create them from nature, “bio-mimicking,” followed by; the proposed solution, motivation, hypothesis and technical objectives. Chapter 2 will explore the root of the problem and proposed solutions of a surface texture for de-icing, uncovered through scholarly reviewed articles and the fundamental mechanism for de-icing. Chapter 3 will discuss the experimental method to create the proposed surfaces, and tests of WCA and

ice formation followed by a description of the analytical techniques used to prove the designs. Chapter 4 will include the results and discussion from the tests. Finally, Chapter 5 will summarize the conclusions and future direction of this work.

Chapter 2: Literature Review

2.1 Fundamental Mechanisms

Ice formation is a complex problem that depends on a variety of form factors. Section 1.4 detailed the icing events in the atmosphere, specifically on a wind turbine blade. For water to freeze, the nucleation size as well as the specific temperature and pressure requirement for the solidification of water is represented in a water phase diagram (Figure 2.1). The purpose of the diagram is to show the different temperatures and pressure can be attributed to the change between the three states: solid, liquid and gas. Water will form ice, when the temperature is below 0ºC at 1 atmosphere (atm) of pressure. Water vapor must first condense onto the surface as a liquid and form to ice at 0°C and 1 atm of pressure.

Ice formation begins with an initial embryo or cluster of water molecules that first

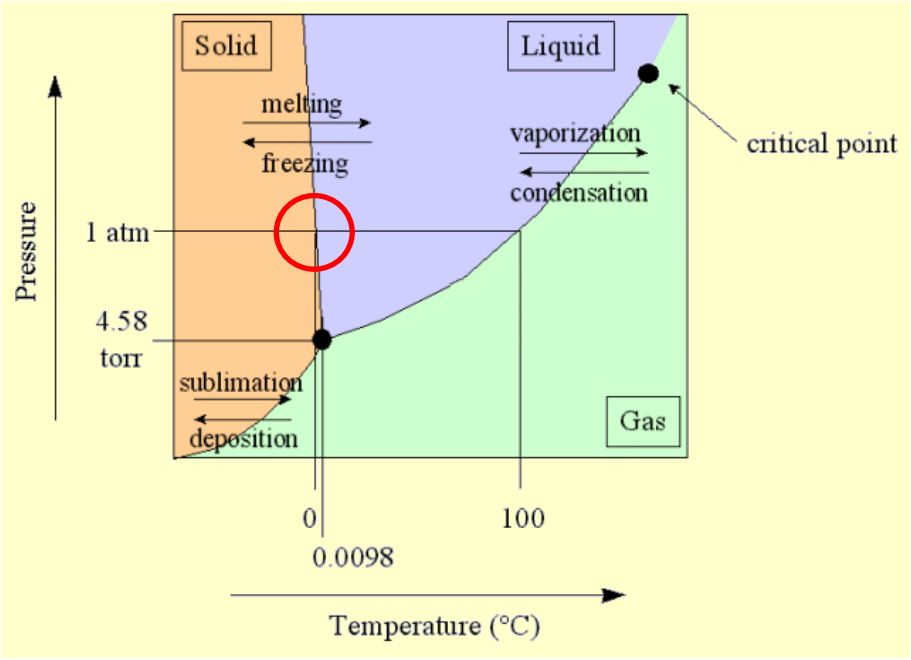

Figure 2.1. Water phase diagram [49].

solidify based on a temperature below 0°C and 1 atm of pressure described in Figure 2.1. After the first embryo, the ice will grow more readily without significant undercooling through clustering of the ice embryos, growing, forming dendrites and joining fractals [48].

In homogeneous nucleation (Figure 2.2), when the water cools below the freezing point, the energy of the crystalline structure is less than the energy of the liquid. The difference in energy is governed by the change in Gibbs free energy of volume (ΔG_v). The total change in energy Gibbs free energy of the system is ΔG in Equation 2.1 [50]:

$$\Delta G = \frac{4}{3}\pi r^3 \Delta G_v + 4\pi r^2 \sigma \qquad \text{(Equation 2.1)}$$

where the volume effects are decided by $\frac{4}{3}\pi r^3 \Delta G_v$ and surface effects are decided by $4\pi r^2 \sigma$, and r is the radius of the embryo and σ is the surface free energy. The first embryo will form when the radius of the water molecule is greater than the critical radius, r^*, Equation 2.2 [50]:

$$r^* = \frac{2\sigma T_m}{\Delta H_f \Delta T} \qquad \text{(Equation 2.2)}$$

where H_f, is the latent heat of fusion, T_m, is the equilibrium solidification temperature, ΔT is the undercooling when the liquid is at a temperature T less than that of the solidification temperature. Latent heat of fusion is the heat given up during the liquid to solid transformation. At the size greater than r^*, the total free energy of the system will decrease allowing for the molecule to solidify. Homogenous nucleation occurs when the undercooling is favorable to form the critical radius of nucleation.

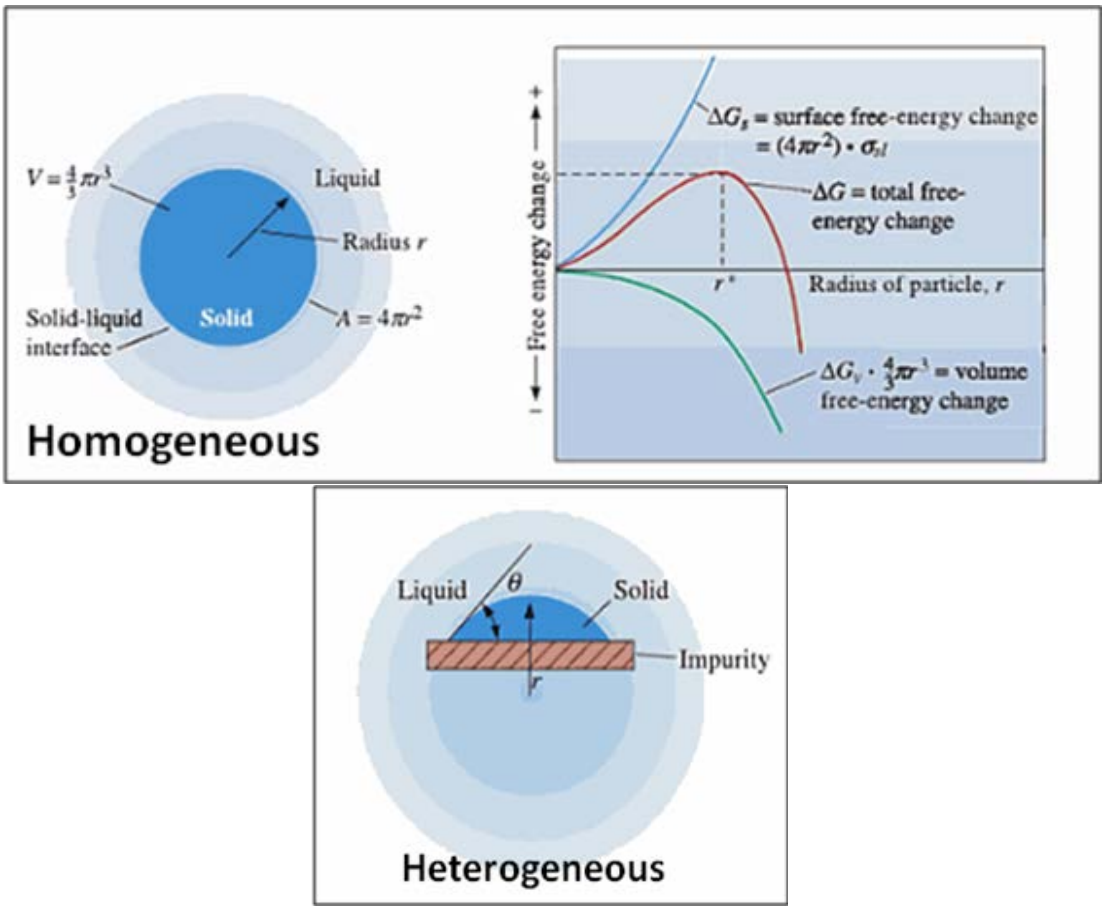

Figure 2.2. Comparison between homogeneous and heterogeneous ice nucleation [50].

Homogeneous nucleation is the ideal formation but the formation typically occurs via heterogeneous nucleation as it is difficult to a devoid liquid of any impurities and irregularities. Heterogeneous nucleation will form under the same conditions as homogeneous but at a critical radius in the range of 10 times smaller than homogeneous due to impurities within the liquid. The impurities allow the water molecules to form at a contact angle (θ) denoted in Figure 2.2. The radius of curvature for the liquid depending on θ allows the first embryo to form at a fraction of the critical radius and undercooling.

Once ice forms it is very difficult to remove. The adhesion is governed by the interaction at the ice-surface interface. The physical mechanisms behind ice adhesion can be classified into four main groups: mechanical interlocking, covalent or chemical

bonding, Van der Waals forces and electrostatic forces. Mechanical interlocking is highly dependent on how the ice conforms to the surface. A greater force will be required to remove ice build-up from a surface where there is ice trapped in asperities on the surface. This mechanism is very important to avoid when designing a surface texture for de-icing, and caution must be taken to not increase the ice formation within the surface features. Covalent bonding is directly dependent on the number of hydrogen bonds attached at the ice-surface interface. Van der Waals forces are the attraction between dipole moments, long range interaction between surface and water molecule. It has been found that this is the weakest force at the interface [51]. Electrostatic force is the interaction of charges from the ice to induced charge on the substrate. The electrostatic force (F) is described Equation 2.3 [48]:

$$F = \frac{q_1 q_2}{r^2} \qquad \text{(Equation 2.3)}$$

where q_1 and q_2 are the charge of the ice and surface material respectively and r is the distance separating the two charges. A few research articles described in Section 2.2 have experimented with materials with low dielectric constant such as Teflon to reduce the induced charge on q_2 with some good results on reduced ice adhesion [31, 48].

The temperature change that initiates solidification of water for rime, freezing rain and vapor condensation is convective cooling, while glaze ice depends on convective and conductive cooling from the blade's surface. The cooling due to conduction of heat through the blade's surface was found to be the dominating cooling mechanism in glaze freezing. Convective cooling from the air around the water plays a less dominating role in this particular freezing process [28].

2.2 Review of Research on Surface Modification for De-Icing

Application of surface modifications for de-icing is the focus of this research. Prior research has shown the feasibility of creating a surface coating for de-icing applications, while need for passive de-icing systems specifically for wind turbines has also been discussed by Dalili et al. [52]. As the power loss for wind blades associated with active de-icing systems was of concern, passive technique gained more attention. However, to date there are no truly icephobic coatings that depend solely on a passive system was concluded by Noormohammed [48].

Current research efforts have made progress in developing attractive surface coatings based on their ice formation and adhesion properties. Cao et al. developed a nanoparticle polymer composite that was based on a nano surface roughness to delay the ice nucleation onto the surface [23]. The test of pouring supercooled water on the surface did not account for all hydrodynamic conditions and ice adhesions. Kuinich & Farzaneh found a rough low surface energy fluoropolymer and titanium dioxide nanoparticles exhibited a lower ice adhesion strength [24]. Multiple tests led to degradation of the surface and higher adhesion. Thus, mechanical properties must also play a role in the adhesion. Kuinich & Farzaneh similarly found that ice adhesion was reduced with low surface energy fluoropolymer and zirconium dioxide nanoparticles coating [25]. Kuinich & Farzaneh claimed that surfaces cannot be completely ice repellent but can have decreased ice adhesion [26]. The test that proved their theory included the measurement of wetting hysteresis on various superhydrophobic surfaces. The researchers believed that reduced ice adhesion to be valid only for surfaces with this low testing value. The reduced adhesion in glaze icing on the surfaces showed a trend for the surfaces with low

hysteresis. The result gave pointed conclusion that the reduced adhesion was due to the reduced contact area. Safaee presented findings on coating and passivation, effect of passivation and coating with nanoparticles, and ice adhesion results [27]. Plasma modification included polytetrafluoroethylene (PTFE or Teflon) onto the nanostructure as thin films deposition. The research concluded ice adhesion was four times lower on the Teflon surface than on the bare surface. Ice adhesion values would increase dramatically due to the breakdown of the Teflon by repeating the experiment due to the low mechanical properties it possesses. Tourkine et al. tests uncovered that superhydrophobic coatings on an aluminum substrate induced a delay in freezing [28]. The findings suggested that conditions such as glaze icing will have an increased chance to roll off the structure before freezing.

The findings reinforce the need to research the area of high strength, weather resistant coatings. Although pervious authors were able to show a reduced ice adhesion on low surface energy materials, the possibility for a more robust system is possible. For the research area of coatings for wind turbine blades, the delayed freezing mechanism discovered by Tourkine et al. was very attractive due to the dynamic forces acting on the water/ice blades' surface, moving water from the surface [28]. Zwieg et al. mimicked a nature inspired freeze avoidance and freeze tolerance species [29]. The novel idea was to create ice nucleating and ice mitigating coating in one. By preparing the coatings with particular areas of ice nucleation attractive nanoparticles, the researchers were able to control where the ice would grow and form dendrites. When the dendrites reached a certain size, a flow of freezing point depressant solutions (propylene glycol, ethylene glycol, and ethanol) was released to de-ice the surface. The ice nucleation coatings were

able to release the ice from the nucleation point before fusion of the crystals with the de-icing fluid flow.

The current state-of-the-art in micro-nano engineering coatings for de-icing has limited application because of the base material selected. In this work, value was added to the research area through additions of novel texturing design to base manufacturing processes and materials. In order to understand the role of a surface modification, it was important to study the science involved in ice formation and adhesion. An additional value added approach aimed in this thesis is a surface texture on a robust PU polymer via an imprinting technique. Table 2.1 describes the uncovered research articles for a surface texture for de-icing.

Table 2.1. Literature review on texture for de-icing.

Texture for De-Icing Reference
Cao et al. (2009). Anti-icing superhydrophobic coatings. [23]
Kuinich & Farzaneh. (2011) On Ice-releasing properties of rough hydrophobic coatings [24].
Kulinich & Farzaneh. (2009a). How wetting hysteresis influences ice adhesion strength on superhydrophobic surfaces [25].
Kulinich & Farzaneh. (2009b). Ice adhesion on super-hydrophobic surfaces [26].
Safaee. (2008) Nanostructured metal surfaces and their Passivation for superhydrophobic and anti-icing applications [27]
Tourkine et al. (2009). Delayed Freezing on Water Repellent Materials [28].
Gou et al. Frost formation on a bionic super-hydrophobic surface under natural convection conditions [30].
Karmouch et al. Icephobic PTFE coatings for wind turbines operating in cold climate conditions [31].
Kietzig et al. Ice Friction: The Effects of Surface Roughness, Structure, and Hydrophobicity [32].

Matsumoto & Daikoku. Fundamental Study on Adhesion of Ice to Solid Surface: Discussion on Coupling of Nano-Scale Field with Macro-Scale Field [33].
Sarkar & Farzaneh. Superhydrophobic Coatings with Reduced Ice Adhesion [34].
Wang et al. A Facile Superhydrophobic Surface for Mitigating Ice Accretion [35].

The physical mechanisms and literature review on the ice formation and adhesion provided several facts on how to prevent or mitigate the problem.

1. Prevent the formation of the critical radius: create an ultra rough nano texture in order to prevent the initial embryo from forming.
2. Decrease the area of water-surface contact: limit the amount of contact, thus limiting the four mechanisms of adhesion (mechanical interlocking, electrostatic, Van der Waals and chemical bonding forces). This will also limit the amount of conductive cooling needed to give the energy required for solidification, as in glaze icing.
3. Modify the surface with low dielectric materials: decrease in dielectric strength will decrease the electrostatic forces at the ice-surface interface.
4. Reduce the freezing point of water: using chemicals such as propylene glycol or other freezing point suppressants, the water must be cooled further for freezing to initiate.

Chapter 3: Experimental Approach

This research was conducted using an overall parameter matrix that was broken down within each subsection of Table 3.1. Chapter 3 was separated according to the series of events for fabricating surface features and design of testing parameters as described in the parameter matrix. The surface profilometer provided the information of the micro pillar height. SEM gave visual justification of the surface topography. CAM measurements were used to determine the angle of the water on the surface giving the hydrophobicity of the surface. AFM determined the nanometer scale surface roughness. For the ice measurement, freeze times were monitored with a video recorder.

Table 3.1. Parameter matrix for the creation of micro-nano surface features on PU

Surface Modification Parameter Matrix		
Condition	**Experimental Phase**	**Justification**
Surface Texturing	"Soft Lithography" Pillar Diameter (45) µm Pitch (70-100) µm Height (12, 23) µm	Base micro surface texture for molding polyurethane. Create micro-pillars on the surface for trapping air.
Chemical Surface Texturing	"10N HNO_3, 30min" Non uniform chemical texture Sub-micrometer range	Creation of nano features within the micro texture on the polyurethane. Dual hierarchy
Experimental Measurement	Contact angle measurement	Describes the level of hydrophobicity
Experimental Measurement	Record droplet freeze time	There is expected to be a time freeze delay for a droplet on the textured surface
Measurement Parameters		
Topography Measurements	Atomic Force Microscope (AFM), Surface Profilometer, Scanning Electron Microscopy (SEM), Contact Angle Measurements (CAM)	
Ice Measurements	Time for a water droplet to freeze	

3.1 PU Surface Modification

Soft lithography was the technology used to form the base microstructure onto the polyurethane (PU) during the curing process. The steps for the imprinting process were: (i) etch a silicon wafer template as the mold; (ii) apply DMDCS (releasing agent) to the mold; (iii) pour the liquid PU over the mold; (iv) remove the fully cured PU from the template.

3.1.1 Description of Materials

Highly hydrophobic surfaces were produced using a single imprinting technique of PU from the surface of an etched silicon wafer. The hierarchy structure was created from a chemical treatment of nitric acid (HNO_3) under sonication for 30 minutes. The PU, AUE-50000, was supplied by Pittsburgh Plate Glass Company (PPG) as the working topcoat. The 10 molar HNO_3 99% purity, acid texture, and dichlorodimethylsilane (DMDCS) 99% purity, release agent, were purchased from VWR.

PU was chosen as the base material for modification because it's use on a wide range of coatings on outdoor structures and specifically wind turbine blades [12]. PU has superior mechanical and coating properties including proven high performance characteristics such as toughness, flexibility, abrasion resistance, chemical resistance, water repellence and UV light stability [53]. Table 3.2 lists some of the advantageous properties of AUE-50000 PU as supplied from PPG [54].

Table 3.2. Material properties of the PU as supplied from manufacturer, PPG [54].

Test	Test Method	PPG-Polyurethane
% Adhesion	ASTM D3359	100%
Pull off Strength	ASTM D4541	5 MPa
Humidity Adhesion	ASTM D4585	340 Hr - No Defects
Impact Resistance	ASTM D2794	100 in/lbs

PU was interesting due to its ability to form various polymer linkages. In general, the reaction between a hydroxyl group (-OH) and an isocyanate urethane linkage (-N=C=O) forms PU represented in Figure 3.1. The specific properties in Table 3.2 of PU are determined by the isocyanate group. PU can be grouped into two categories: aromatic or aliphatic isocyanate. Aromatic groups contain some form of a hydrocarbon, benzene or phenol group [56]. Aliphatic groups were those with non-aromatic carbon containing

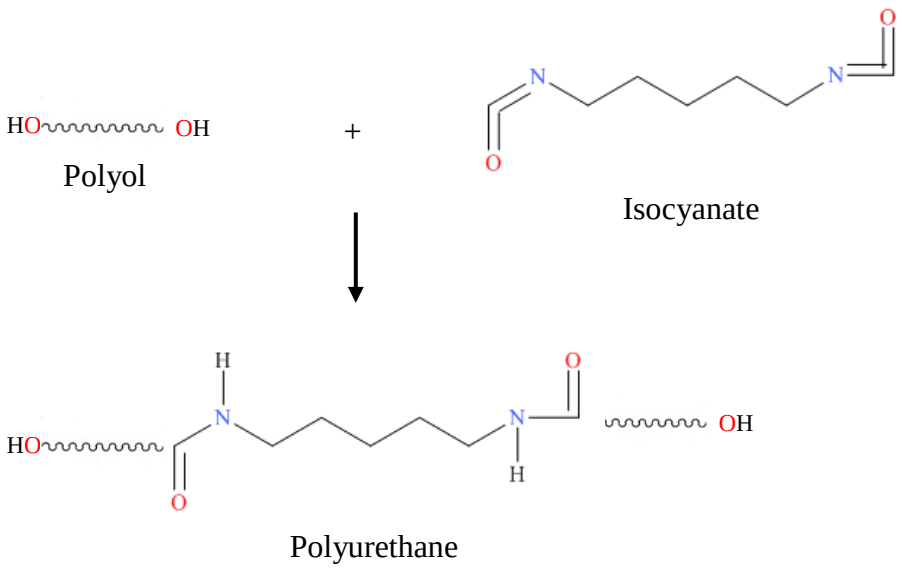

Figure 3.1. Fundamental polymer linkage for the creation of PU [55]

compounds. In this work, Aliphatic polyurethane was used due to the higher resistance to ultraviolet light than that compared to the aromatic groups [53, 55, 56].

The chemical release agent DMDCS was chosen as produced from other research works [57-59]. The process of forming a protective coating is described in Figure 3.2 from Ahn et al. (2009) [59]. A reiteration of their explanation is that the silicon chloride bonds (Si-Cl) break to form silicon hydroxide (Si-OH) bonds. Hydrochloric acid (HCl) is produced with trace amounts of water as shown in the reaction in Figure 3.2 A. HCl does not interact with the silicon surface or impede the silanization. The silanol groups can be covalently attached to the free hydroxyl groups on the surface by swabbing the surface.

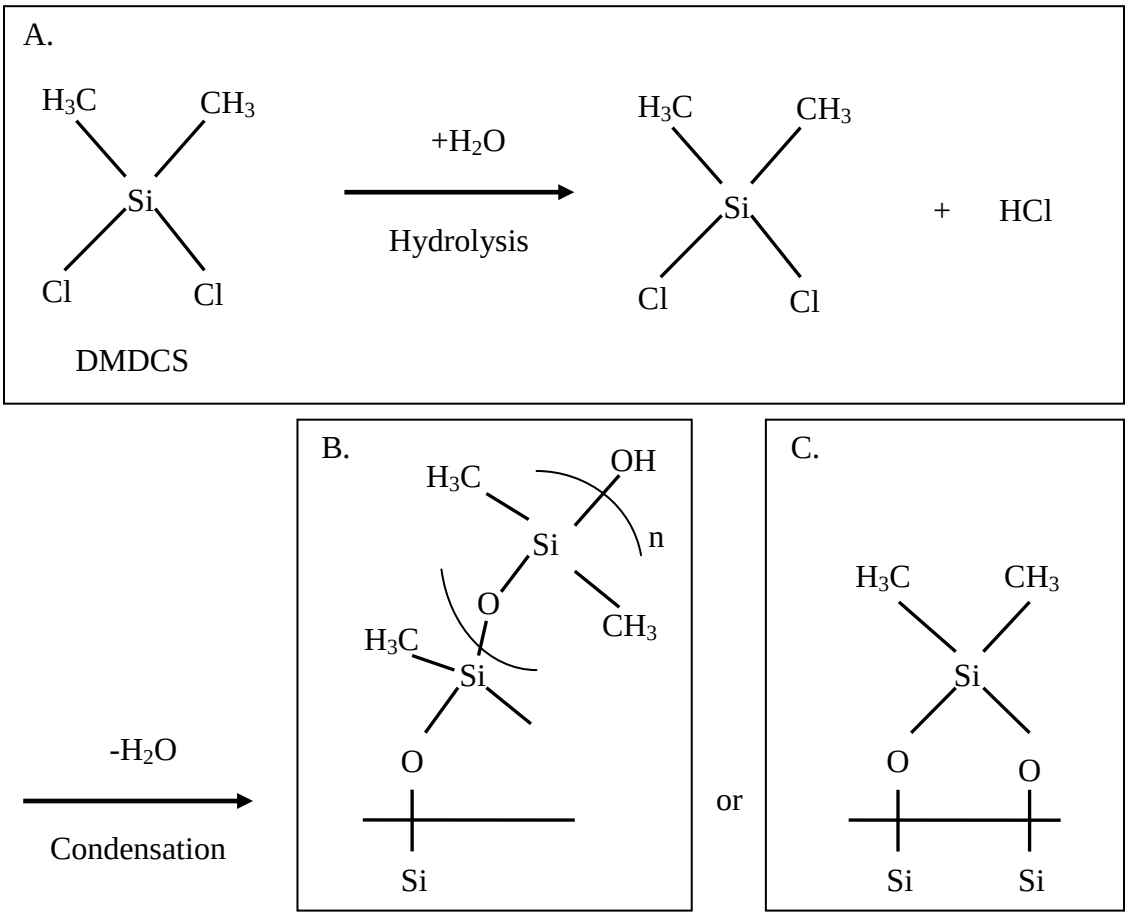

Figure 3.2. Formation of DMDCS on the silicon substrate A. DMDCS hydrolysis. B. Monolayer formation. C. Binary covalent attachment [59].

Di-trichlorosilanes tend to polymerize vertically with available unbound silanol groups resulting in multilayer formation as shown in Figure 3.2 B. Otherwise, monolayer of DMDCS molecules can be formed by binary covalent attachment in the absence of unbound silanol groups as shown in Figure 3.2 C. The resultant was the successful coverage of the silicon substrate by DMDCS.

3.1.2 Soft Lithography

The objective was to form the base microstructure seen in the SEM surface analysis of the lotus leaf, Figure 3.3. The superhydrophobic nature of the lotus leaf is based on a dual micro-nano hierarchy structure with the micro structure as the leaf and over-coating in hydrophobic three-dimensional wax nanostructures [37].

An illustration on the soft lithography technique is described in Figure 3.4. A template was fabricated with holes etched into the template in Figure 3.4 B. The template was the “negative” imprint, while the “positive” replica is denoted in Figure 3.4 A. The idea was that an inverse replica could be formed during the curing process of the polymer. The replica in Figure 3.4 A was an image of the lotus leaf microstructure surface whereas the polymer was formed with a similar surface microstructure. Additional nano-hierarchy features were added later by a chemical surface processing.

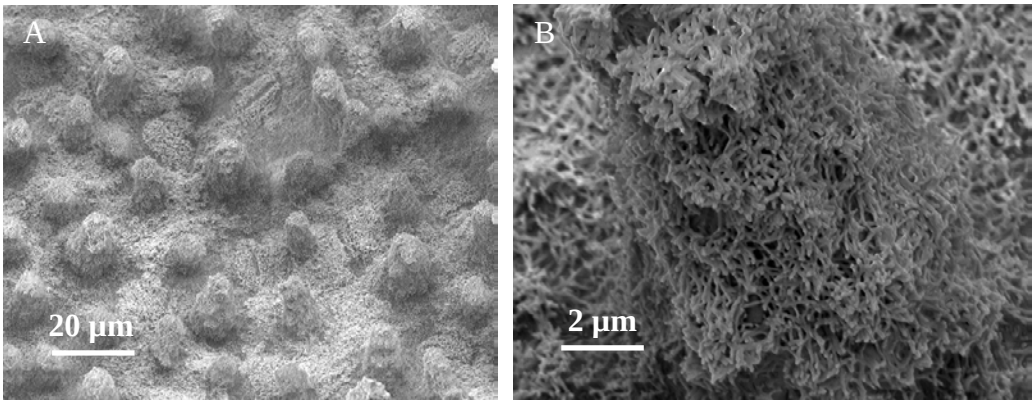

Figure 3.3. Surface topography of a lotus leaf, magnification A. 1000x B. 10000x

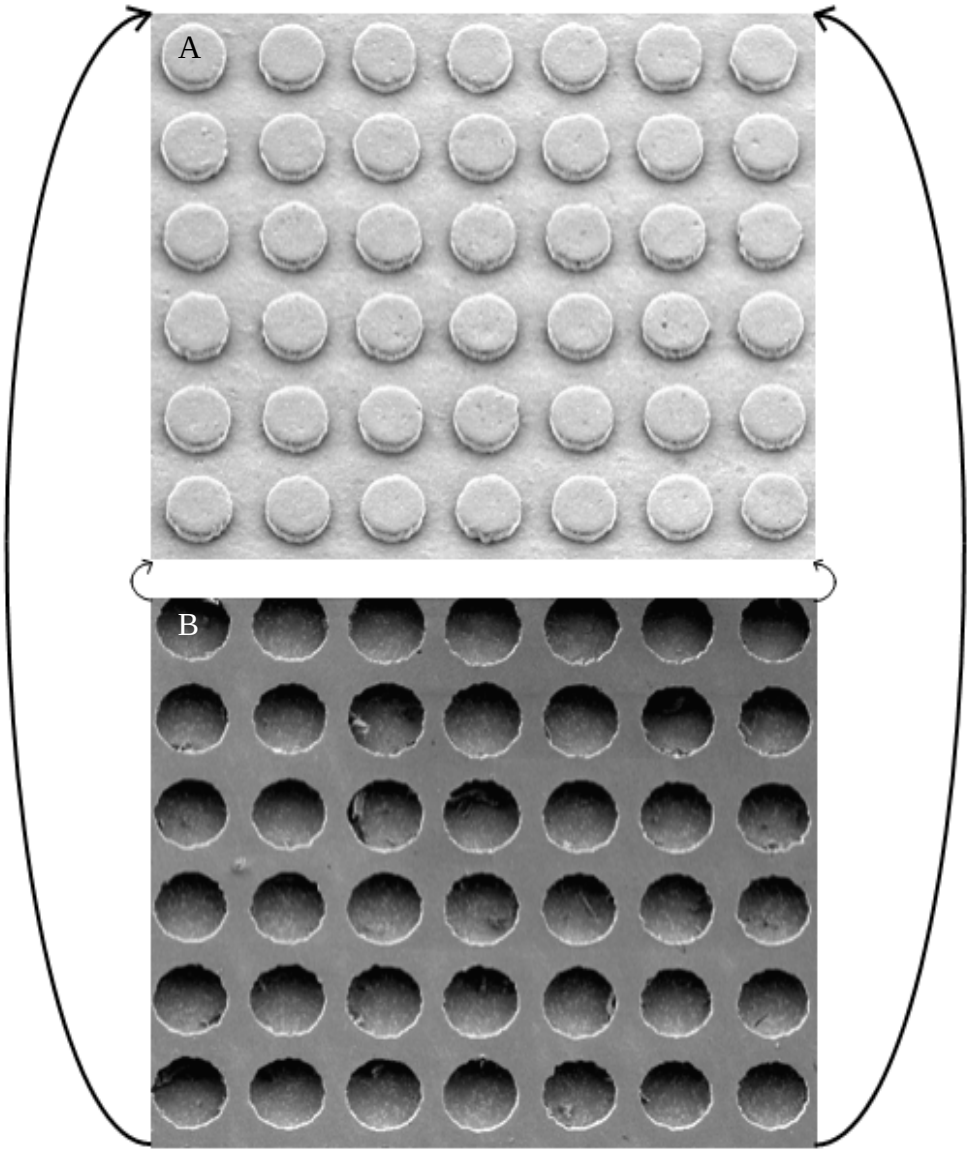

Figure 3.4. Soft lithography process. A. Replicated topography of PU surface. B. Etched silicon template from which the surface is replicated

3.1.3 Template Fabrication

The first attempt at fabricating the template was by way of laser machining. Laser machining was the first option for creating the template because of the ease of adding another manufacturing step in the coating process for wind turbine blades. Aluminum samples were mirror polished and sent to JPL Lasers to be laser processed with an excimer laser. From the literature, many research articles described the laser obliteration and removal of materials from a substrate. The excimer laser was an attractive option because of the small size the diameter of the laser could focus (down to single microns) [60-62].

An AutoCAD drawing with the feature size was sent with the aluminum substrate, Figure 3.5. The design mimicked the size of the lotus microstructure: five micron diameter, 10 µm pitch, and 10 µm depth, the precise creation was ideal. The laser machined samples were received with the required pitch and diameter. However, the energy density required to produce the depth of the holes could not be achieved.

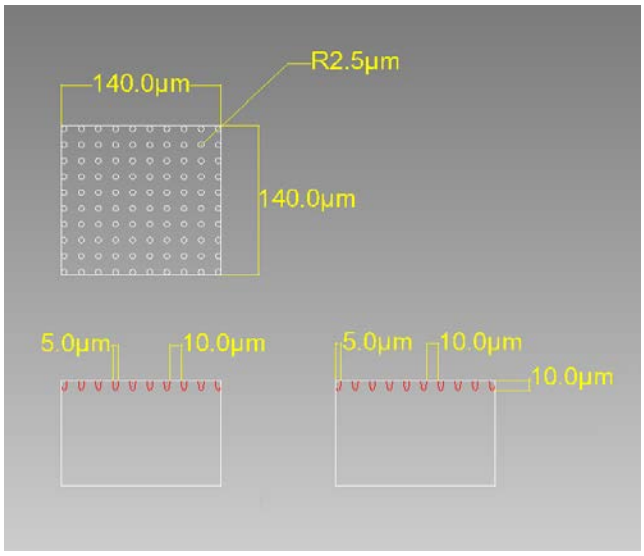

Figure 3.5. AutoCAD dimensioning of the laser machined template

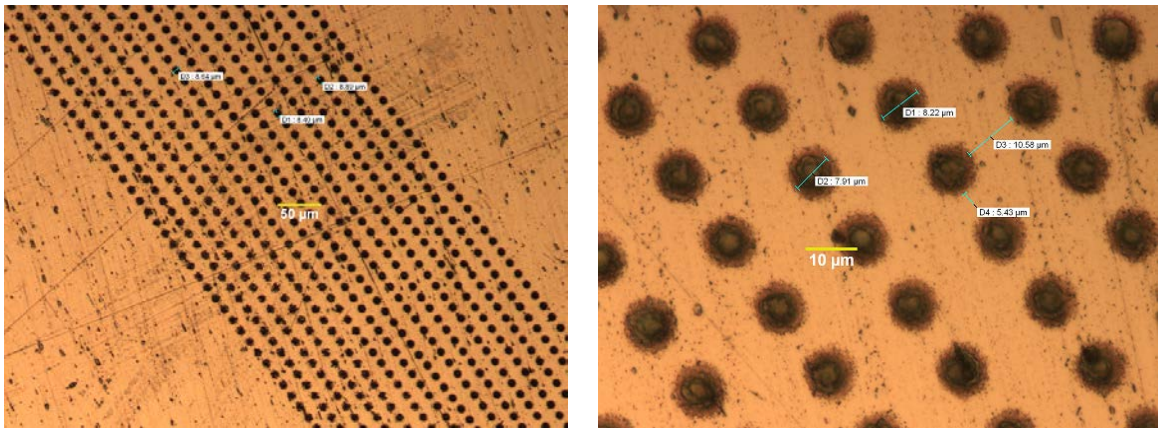

Figure 3.6. Optical microscopy of the laser machined sample. Magnification A. 10x, B. 50x

Figure 3.6 images the precise pitch and diameter that was achieved through laser machining. However, the depth achieved was 1-2 µm, which was 8 µm less than needed.

The required depth of the features were not met via laser machining, so the second method tried was a photolithography/deep reactive ion etching process (DRIE), available at the University of Arkansas. In this work, precise etching of holes in the wafer was desired. Using the high density electronics center (HiDEC) facilities at the University of Arkansas, a photolithography process was developed to create a particular pattern of holes for this purpose as represented in Table 3.3.

Table 3.3. Process flow for the photolithography

Photolithography Process	
Task	**Justification**
Clean wafers	Rid the wafers of any foreign particles
Apply AZ-4620 photoresist	10 µm Thickness (2500 rpm) to protect wafer during DRIE
Bake	Cures photoresist
Expose	Exposed photoresist can be developed (positive resist) Time = Energy / Intensity
Develop	Removes exposed photoresist
Clean wafers	Rid the patterned wafers of any foreign particles

Photolithography was used to cover a pattern on a particular area on the template. Photoresist, a light sensitive polymer, was exposed to light through a patterned mask. In Table 3.3, AZ 4620 was chosen as the photoresist due to the required thickness needed to protect the unexposed areas on the template during the DRIE process as previously developed in the HiDEC facilities. Patterned masks were purchased for the exposure step from Advanced Reproductions. The AutoCAD file used to print the mask contained four areas with equivalent diameter circles and various pitches. The minimum features that could be achieved through the photo-plot design of the mask was an 20 µm diameter with a 25 µm spacing yielding a minimum pitch spacing of 45 µm (Table 3.4). The spacing of the mask in the photolithography process was labeled in Figure 3.7 A, C and E. The photo mask images with varying pitch were omitted in this thesis due to the similarities in appearance.

Table 3.4 The dimensions of the photolithography masks for template creation.

Feature Diameter	20 µm	35 µm	45 µm
Feature Pitch	45 µm	55 µm	70 µm
	55 µm	65 µm	80 µm
	65 µm	75 µm	90 µm
	75 µm	85 µm	100 µm

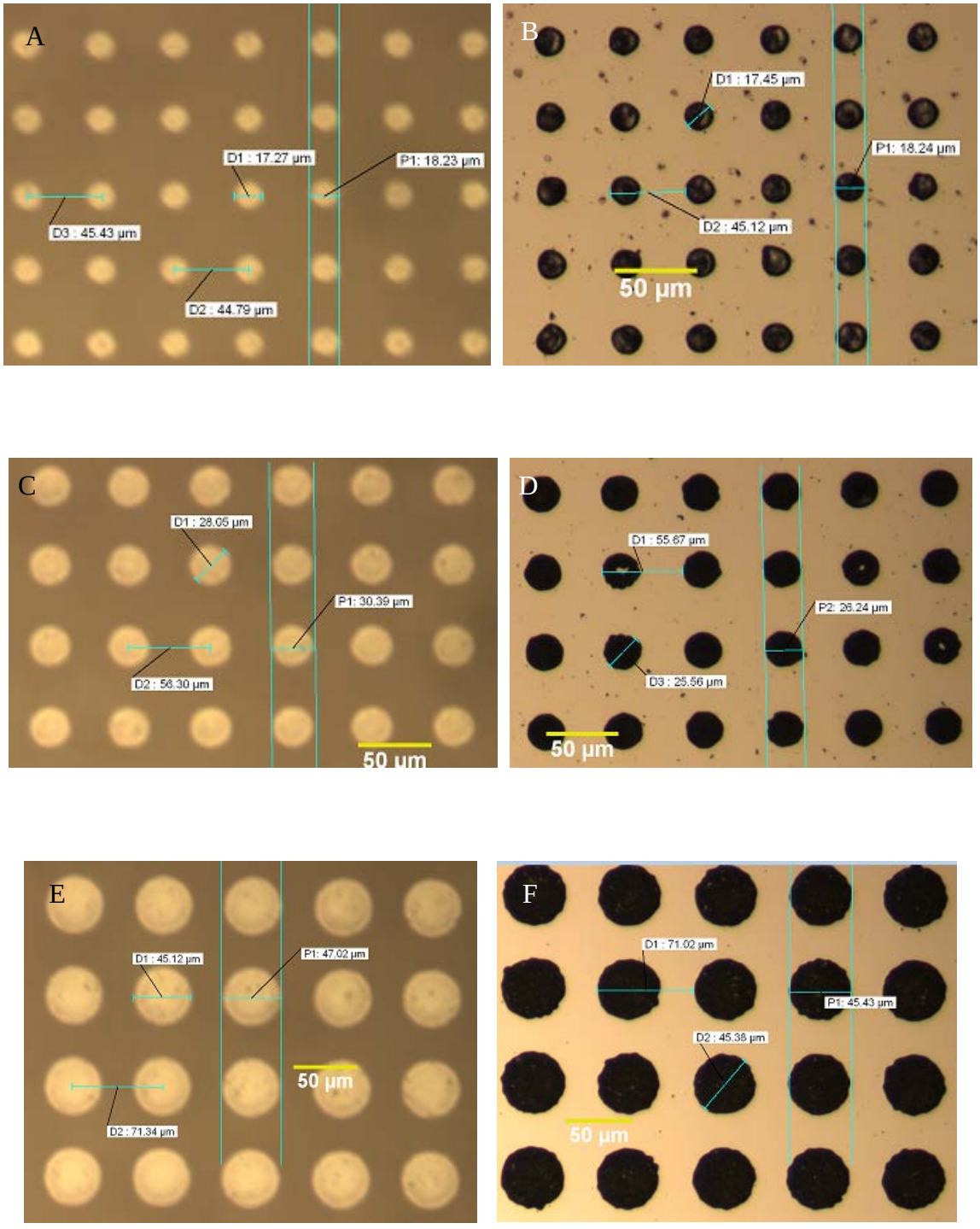

Figure 3.7. Optical microscopy of the photolithography masks A. 18 µm diameter. C. 28 µm diameter. E. 45 µm diameter. Optical microscopy of the etched silicon wafer. B. 18 µm diameter. D. 28 µm diameter. F. 45 µm diameter.

Etching is the removal of material by chemical means [46]. The silicon etch parameters that were developed by HiDEC were verified through this work and produced an etch rate of 1 µm/min as graphically represented in Figure 3.8. The AZ4620 pattered onto the wafer (10 µm height) in the photolithography process protects the particular areas it covered on the wafer during the DRIE process. The DRIE process was controlled through various gas flows and an RF voltage. Octafluorocyclobutane (C_4F_8) was deposited for side passivation of the holes and mask protection of lateral etching during the cycles. Sulfur Hexafluoride (SF_6) as the etchant and Oxygen (O_2) plasma were used for etching into silicon wafer. The RF supplies power bias to the electrode which supports the wafer. The bias between the wafer and plasma directs the positively charged etchant ions to the surface of the wafer for a z-directional vertical etch.

Figure 3.8 displays a snapshot of the etch cycle that produced high aspect ratio holes into silicon. Wafers were then cleaned with the solvent (AZ300T) at 90°C for 10 minutes to remove excess photoresist and any C_4F_8 that remained on the wafer upon

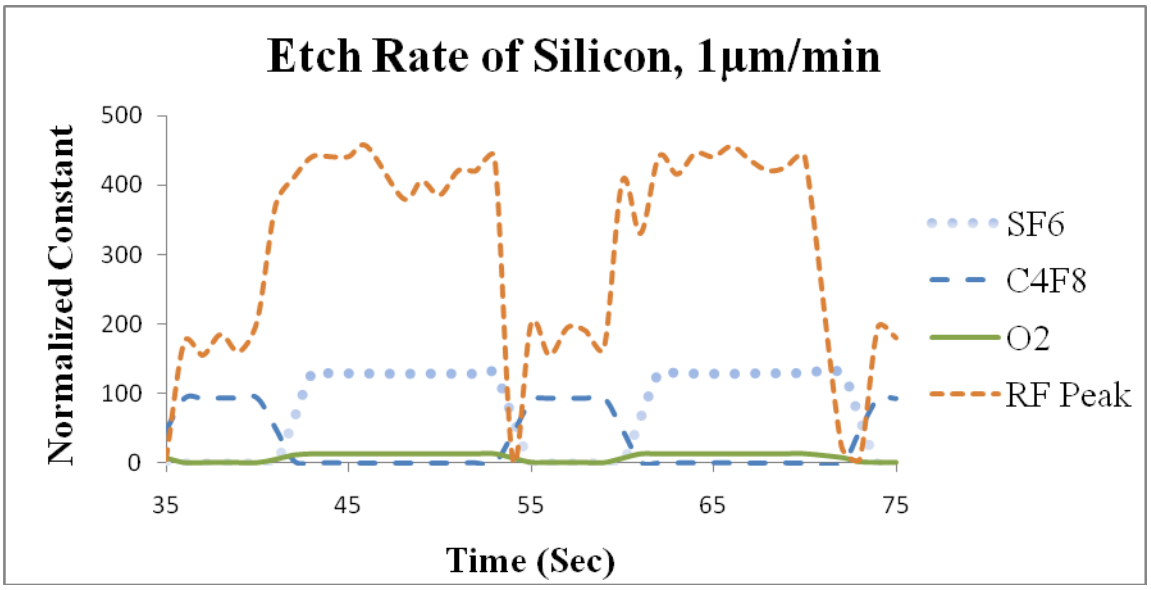

Figure 3.8. Etching cycle, gas flow and RF voltage, for the DRIE

completion of the etching process. Figures 3.7 B, D and F depicts the created templates from the particular photolithography masks and etching process. The measurements of the created holes in the template matched within a micron of the mask, which showed the anisotropic etching in the process. The holes appeared dark, Figures 3.7 B, D, F, in the optical microscopy due to the focus of the reflected light.

After initial problems in the molding procedure, the successfully created molds from the templates were characterized with holes of 45 μm in diameter (Table 3.5). The feature pitch was varied to study the effect it would have on wetting. Because this work was the first on experimentation with the pitch on PU, it was decided to find the limit of the wetting before the transition from the Cassie-Baxter to the Wenzel State (refer to Figure 1.8). The variable feature depth which determined the feature height was varied in the experiment for the same reasoning.

The templates were characterized using a surface profilometer (Dektak 3 by Veeco) to measure the pitch and depths of the sample. The feature depth measured to be within ± 0.5 μm and the pitch measured within 1 μm as shown in Figures 3.9 B and 3.10 B. SEM analysis was also performed on both templates as shown in Figures 3.9 A and 3.10 A. The variable pitch was omitted in this thesis due to the similarities of images. The results from the measurement of the surface profile and were 12 and 23 μm respectively.

Table 3.5. Final creation of the etched templates for soft lithography.

Feature Diameter	45 μm	
Feature Depth	12μm	23 μm
Feature Pitch	70 μm 80 μm 90 μm 100 μm	

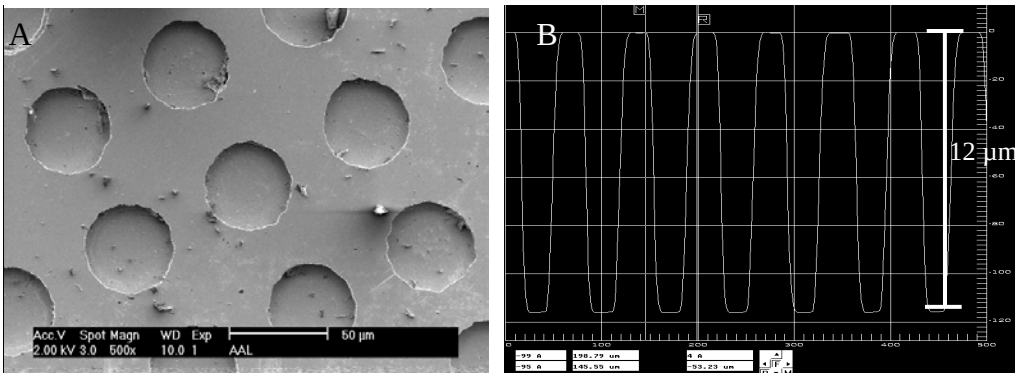

Figure 3.9. A. SEM image of the etched silicon template 12 µm height, mag. 500x. B. Profile measurement characterizing the depth of the etched wafer.

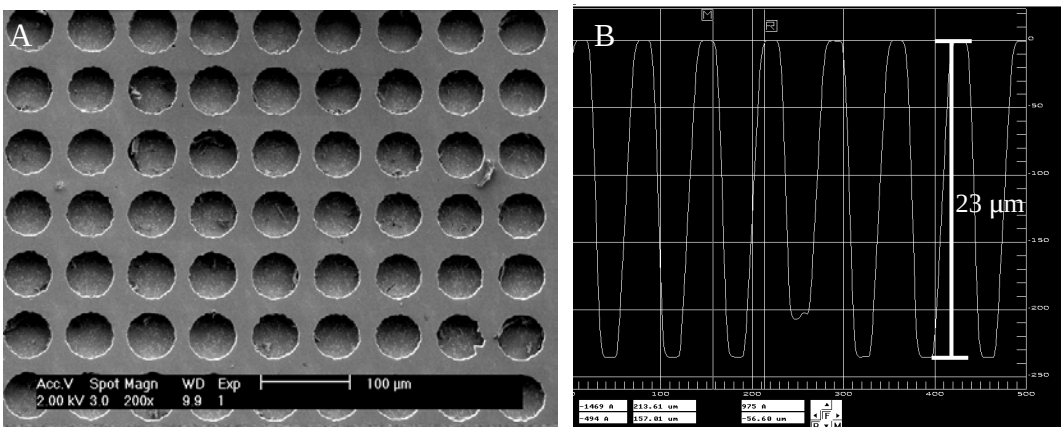

Figure 3.10. A. SEM image of the etched silicon template 23 µm height, mag. 200x. B. Profile measurement characterizing the depth of the etched wafer.

3.1.4 Molding Process

The molding process was described in Figure 3.5, which explained the removal of a "positive" imprint from a "negative" template. Both pouring and spraying the PU as detailed in the process diagram Figure 3.11 produced equally good results. The first moldings were created from the laser machined samples. Although the templates were not of the required depth, the molding process flow was developed during the replication of this template. From the literature, it was found that a range of molding polymer materials including PU was achieved using the release agent, trimethylchlorosilane (TMCS) [64].

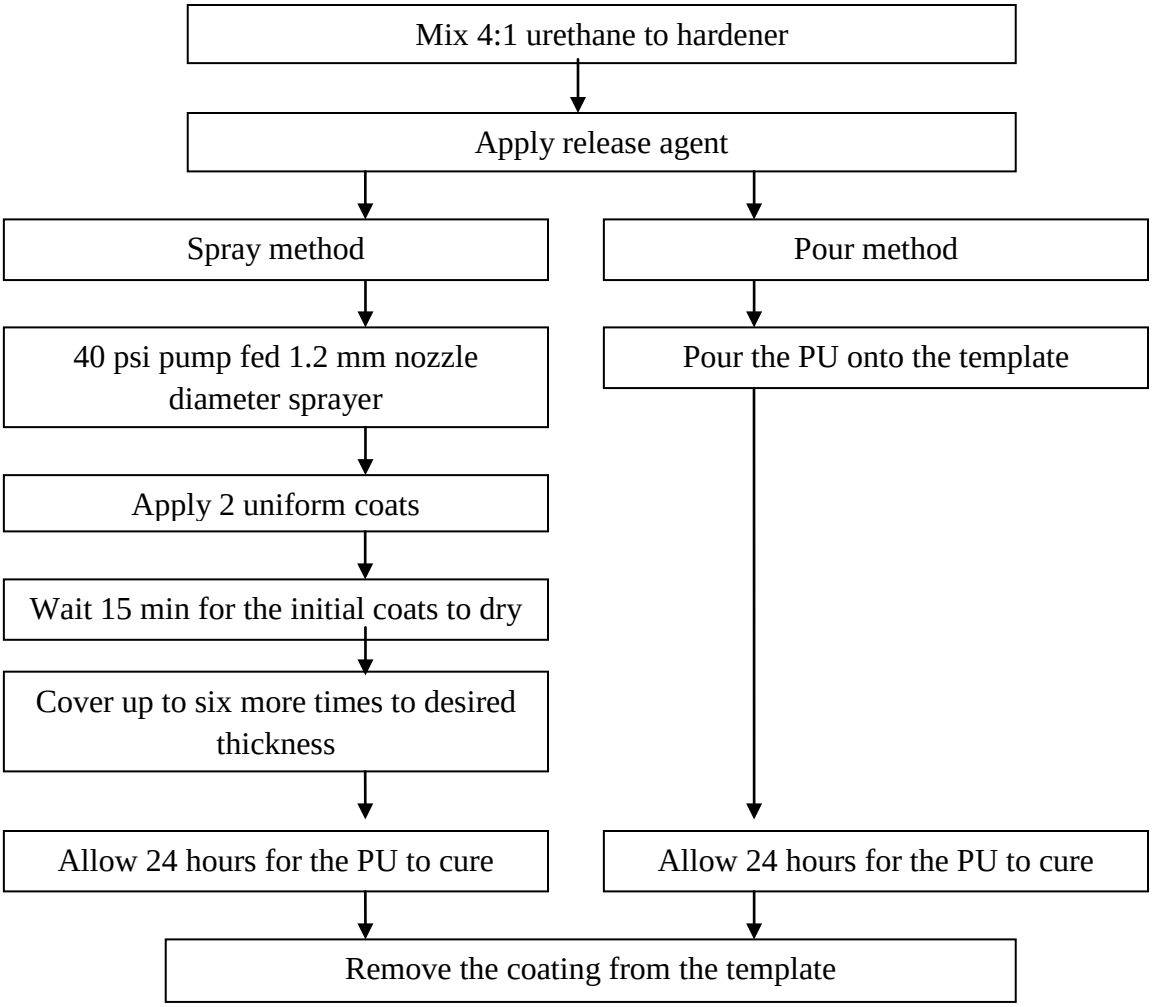

Figure 3.11. Process flow of the soft lithography process.

Following the procedure in Figure 3.11, the replica from the aluminum template did not turn out as expected. Figure 3.12 shows that there was deformation at the tip of the PU. It was thought that there could be some issues with the PU ability to flow into these features because of trapped air bubbles in the small 5 µm diameter. Even with the imperfect results, replication could be achieved by varying some measurement parameters, such as an airless chamber, heat or pressure to flow the PU into the mold.

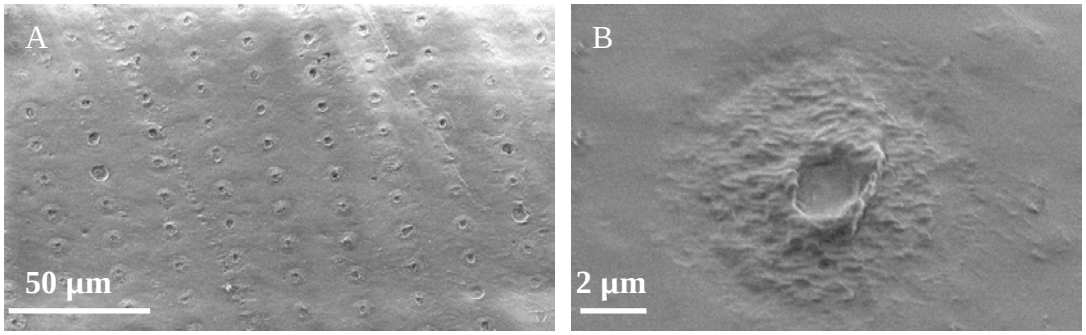

Figure 3.12. PU replicas from the laser machined template, magnification A. 650x, B. 8000x.

The first template fabricated in Table 3.4 were used to replicate the PU. The initial template created using this process had a diameter of 10 µm and a depth of 4 µm due to underexposing of the photoresist and short etching time of the template. Upon first replication, the features did not replicate from the mold as shown in Figure 3.13. The locations where the holes in the template were formed created with no pillar formations.

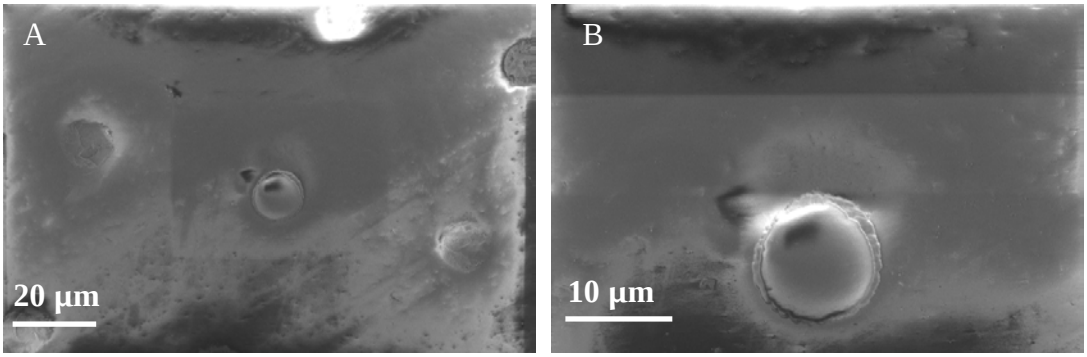

Figure 3.13. PU replicas from the etched silicon template, magnification A. 1000x, B. 2500x.

From these results, a new parameter was added to address the air trapped in the micron size holes of the template. The idea was to remove air from chamber with a vacuum pump inside the glove box during the pouring and curing of the polymer. However, Figure 3.14 shows there was no micro-pillar formation on the PU replica.

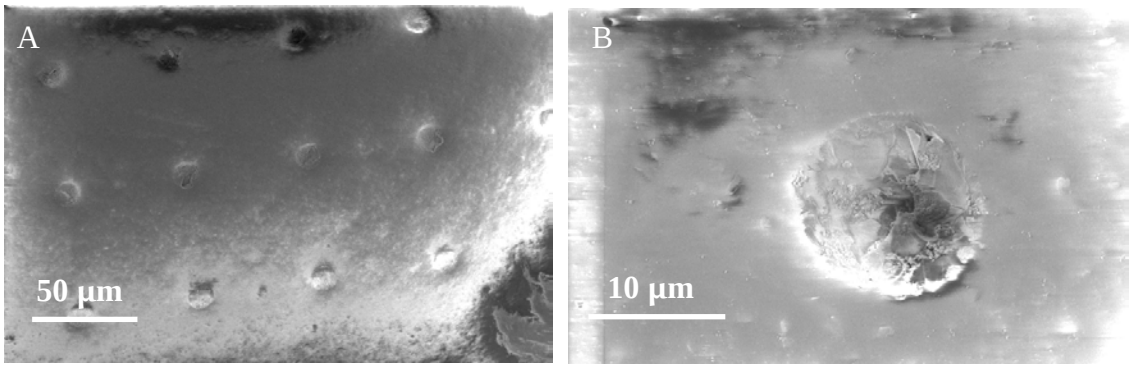

Figure 3.14. PU replicas from the air depleted template, magnification A. 500x, B. 3500x.

It was discovered from Figure 3.13 and 3.14 that there was much charging on the PU samples due to the nonconductive properties. Even at low SEM beam voltage of 2 keV the samples produced charging. Before further experimentation, a coating technique to sputter the PU samples with 5 nm of Gold and Palladium (Au/Pd) particles was developed. The Anatech LTD sputter coater was used to perform this technique. In a vacuum chamber shown in Figure 3.15, the PU samples were sputtered for 2.5 minutes in an 80mT Argon rich chamber. The particles were coated onto the PU after replication to increase the conductivity thus decreasing sample charging during SEM analysis.

Figure 3.15. Au/Pd sputter system.

The application of force was the next parameter that was varied. Force was used to press the PU into the micro-cavities of the template. Using the same template, a 1 kg weight was applied to the sample during the curing process. Again, the PU did not form into the micro-cavities of the template shown in Figure 3.16.

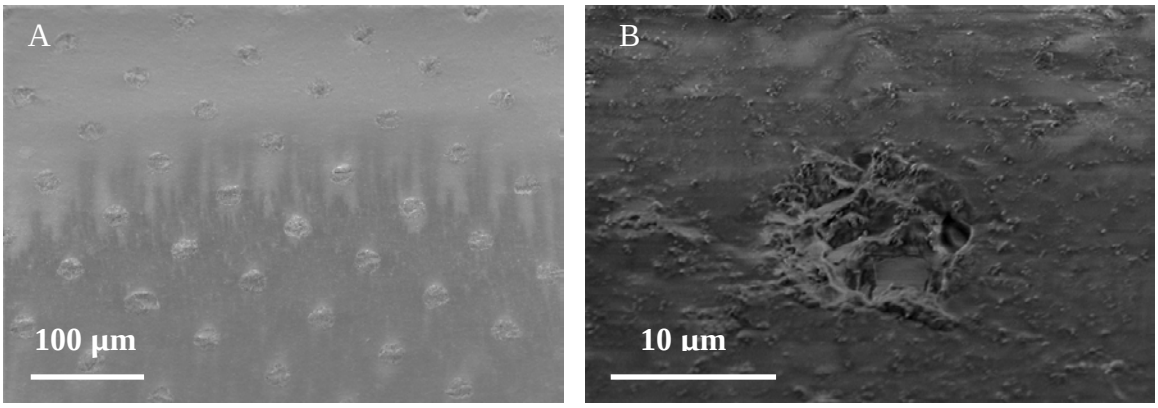

Figure 3.16. PU replicas with force applied to the polymer, magnification A. 250x, B. 3500x.

The next parameter varied was curing the polymer with supplied external heat. The reasoning for using heat was that the liquid PU would become more viscous during the curing process, thus able to more readily flow in the holes of the etched template. In an oven, the applied heat during the PU cure process was at 60°C for 1.5 hours. There were some replications seen in Figure 3.17, but the heat destroyed the surface.

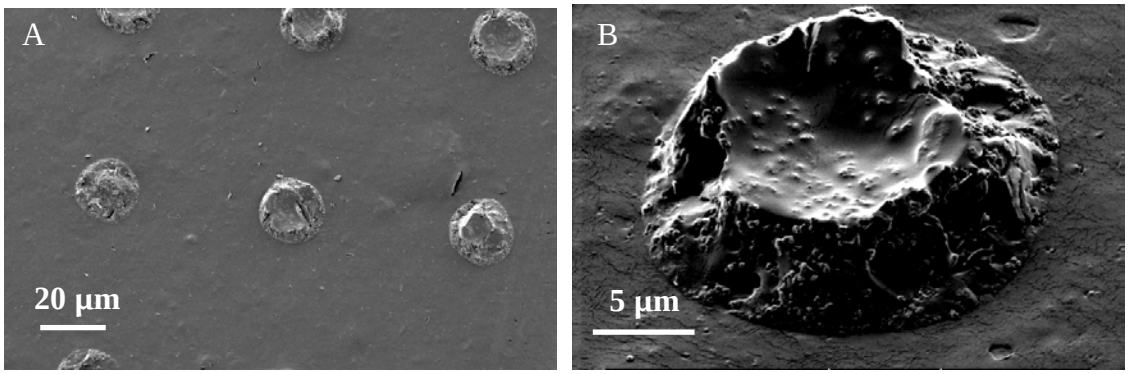

Figure 3.17. PU replicas heat curing during molding, magnification A. 800x, B. 5000x.

Throughout the imaged PU surface, there were cracks formed because of the heat supplied during curing.

Because of the unsuccessful attempts at curing the PU into small 5 and 10 µm diameter holes, the next parameter that was varied was the diameter of the etched region. The first replication of the 45 µm diameter mold cured at room temperature. The thought was that the polyurethane could flow into the larger spaces. Upon SEM verification, it was found that no pillar replication occurred seen in Figure 3.18.

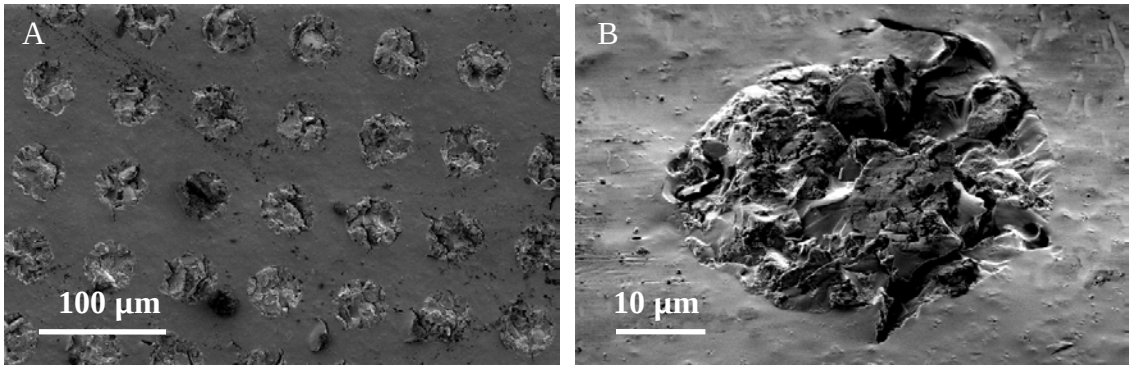

Figure 3.18. PU replicas from the 45 µm surface features, magnification A. 200x, B. 1500x.

There were few literature references on the molding of PU while molding of Polydimethylsiloxane (PDMS) is a highly researched polymer known for its ability to replicate features to the nanometers in size [65]. Thus, PDMS was cured to the etched template using TMCS as the release agent. The resultant was patterned micron size pillar that were a true replication of the template in Figure 3.19. The pillars formed were not an addition to the surface material, rather they were an extension of the PDMS. This proved that the templates were not the limiting factor in replicating; rather the only variables left were the release agent or more probably the material PU.

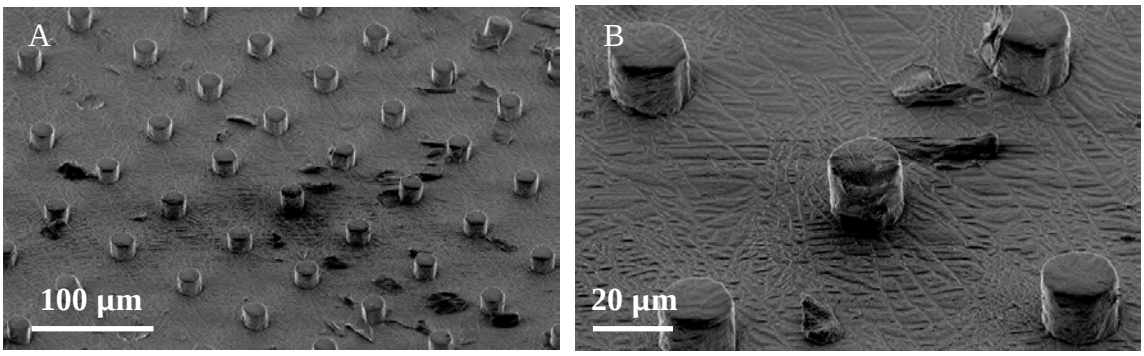

Figure 3.19. PDMS replicas from the etched silicon wafer, magnification A. 200x, B. 1000x.

The goal of this thesis was to form a high strength polymer with a surface texture. So, altering the release agent in the experiment to produce the replicas on the PU surface was attempted experimentally. According to the literature, other polymer materials were successfully replicated using the Buehler Release Agent [66]. Using the new release agent the PU was difficult to remove from the surface of the template. The area that was successfully removed showed no pillar formation on the replica as seen in Figure 3.20.

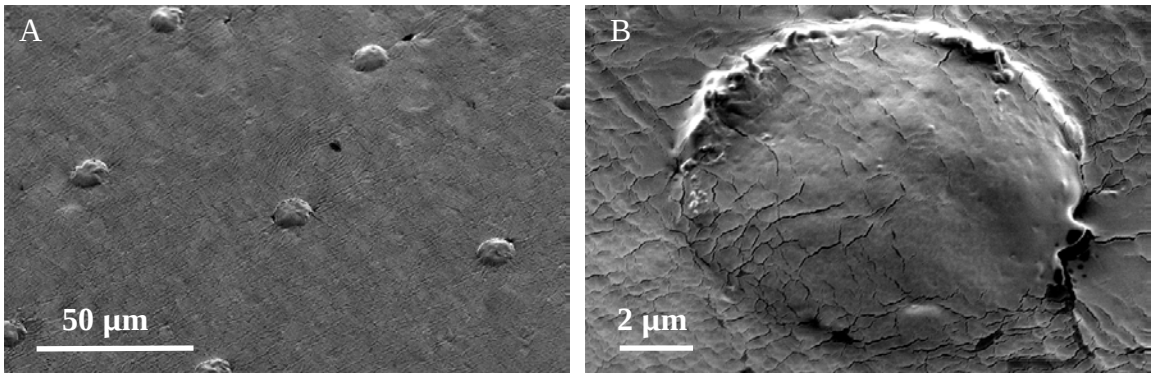

Figure 3.20. PU replicas from the 45 µm surface features, magnification A. 500x, B. 5000x.

Decent replications in Figure 3.17 spurred the idea of a heating parameter matrix using the larger diameters templates. To see the role heat played into the pillar formation, three separate molds were created again using the TMCS releasing agent at temperatures of 55°C for 1 hr, 45°C for 1 hr and 35°C for 1 hr. The SEM images are

shown in Figures 3.21, 3.22 and 3.23 respectively. All three images had good pillar formation regardless of the heating used in the experiment. Examination of the area on the PU image showed that the pillars appeared torn upon release from the molding templates. Difficulty of the PU to flow into the mold was not the problem, rather replication problems of surface features seemed to be from the PU adhering to the template within the holes.

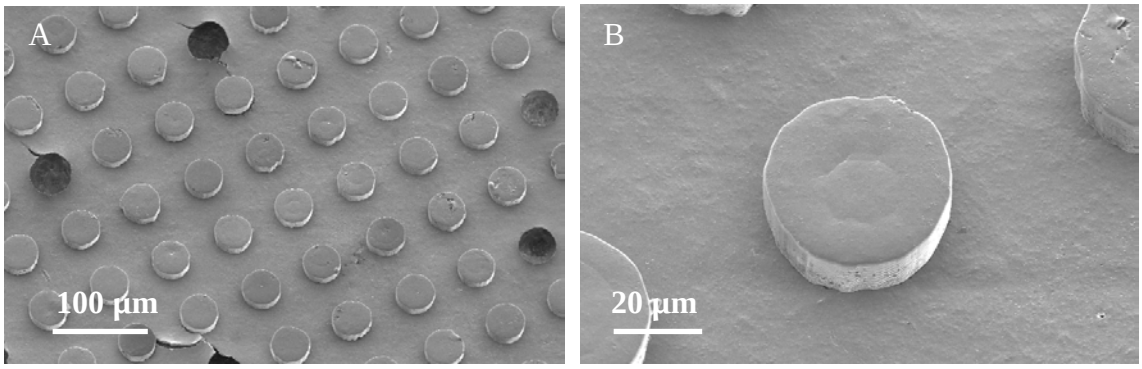

Figure 3.21 PU replicas 55ºC heat curing during molding, magnification A. 200x, B. 1000x.

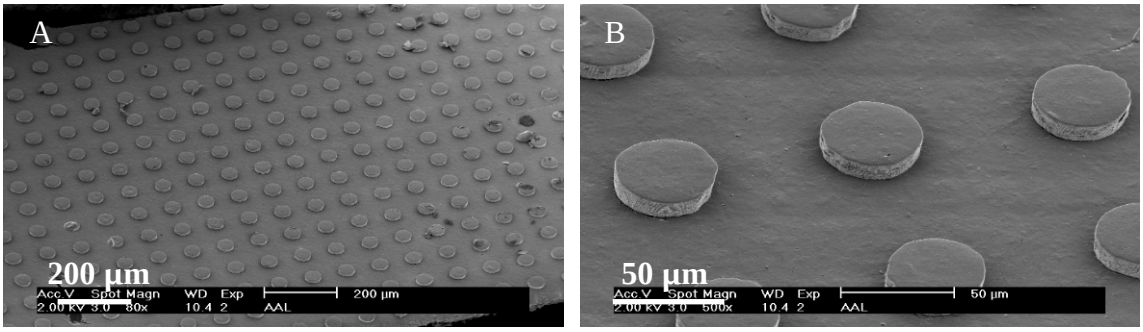

Figure 3.22. PU replicas 45ºC heat curing during molding, magnification A.80x, B.500x.

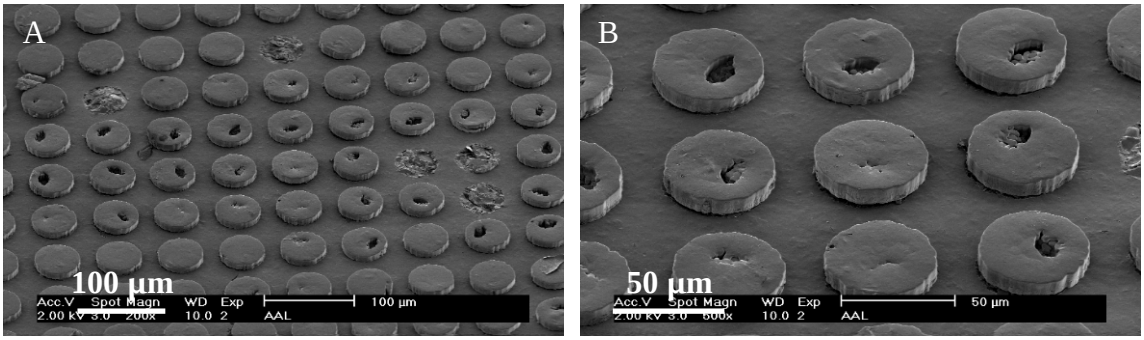

Figure 3.23. PU replicas 35ºC heat curing during molding, magnification A.200x, B.500x.

The next step was to verify the newly formed problem: the pillars were being torn upon release from the molds. An SEM imaging confirmed the problem. Figure 3.24 displays the SEM image of the etched silicon wafer with PU remaining in various locations of the etched holes on the wafer. This build-up was the first sign that the releasing agent TMCS was not fully coating the entire area of the wafer, thus not allowing the full release of PU.

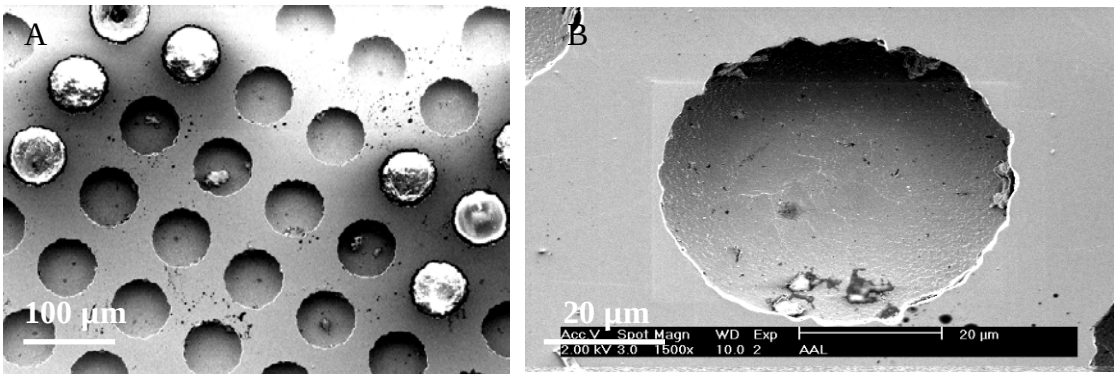

Figure 3.24. Etched templates before cleaning, magnification A. 200x, B. 1500x.

Cleaning the silicon wafer required the application of a lacquer thinner directly to the surface. The lacquer thinner broke down the bonds within the PU allowing for the dissolving of the PU left behind in the template. Acetone was then used to clean any additional impurities left on the surface. Results of the clean templates were verified using SEM imaging in Figure 3.25.

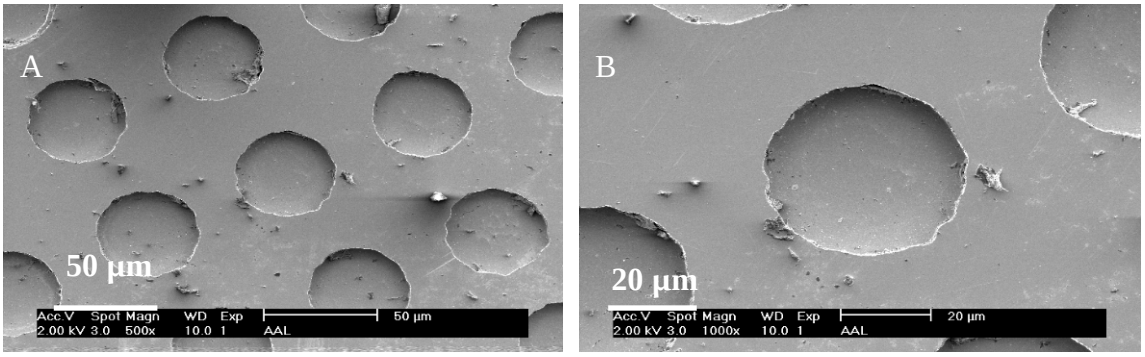

Figure 3.25. Etched templates after cleaning, magnification A. 500x, B. 1000x

Extensive literature review uncovered another release agent that has been used in the recent past for replicating polymers, Dimethyldichlorosilane (DMDCS) [57-59]. The releasing agent adheres to the silicon template with attached methyl groups protecting the PU from adhering to the silicon template shown in Figure 3.2. The control test for the release agent was performed on a polished non-etched silicon wafer. The procedure followed was the same as described in Figure 3.11, with the only change being the releasing agent. There were no problems using the new agent. The produced replicas were verified using SEM images in Figure 3.26. Visually there didn't appear to be any major disturbances in the surface of the PU.

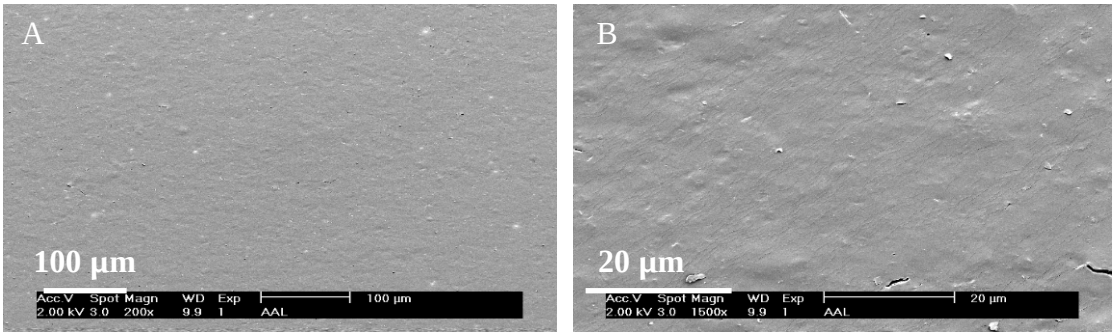

Figure 3.26. PU replicas molded from polished silicon wafer, magnification A. 200x, B. 1500x.

A verification of the roughness on the flat molded PU sample was performed using AFM. The polished silicon template from which the PU was replicated had a Ra roughness of 5 nm. AFM results of the PU replica over the 50 µm shown in Figure 3.27 gave a RMS roughness of 100 nm, Ra roughness of 78 nm and Rmax of 0.91 µm. The roughness of the sample was replicated from the roughness of the wafer. Also, additional roughness was formed due to the build-up of the releasing agent or the orientation of the polymer chains linked during the curing process [59]. It should be noted that the height change displayed was less than 1 µm difference with a uniform surface.

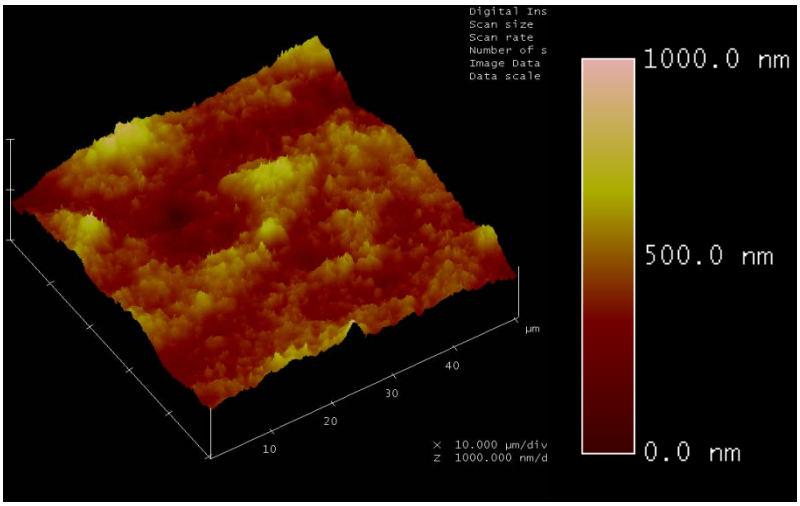

Figure 3.27. AFM topography, PU replicas molded from polished silicon wafer in a three dimensional view.

Using DMDCS as the releasing agent, the next step was to mold the PU to the etched templates. The procedure was followed as represented in Figure 3.11, only replacing the old releasing agent (TMCS) with DMDCS. The 45 µm diameter features molded are shown in Figure 3.28 (height of 12 µm), and 3.29 (height of 23 µm). The other PU surfaces created with variable pitch described in Table 3.5 gave similar results and hence omitted. It was found using SEM, the area (1 cm x 1 cm) produced 99% pillar formation across the surface.

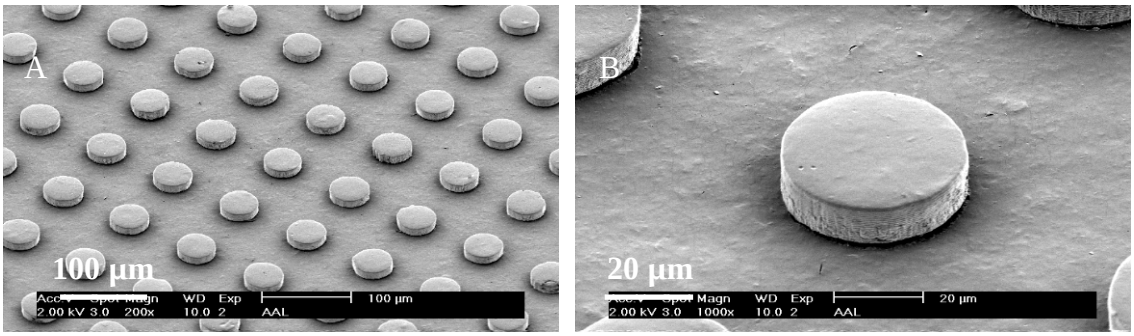

Figure 3.28. PU replicas molded using DMDCS height 12 µm, magnification A. 200x. B. 1000x.

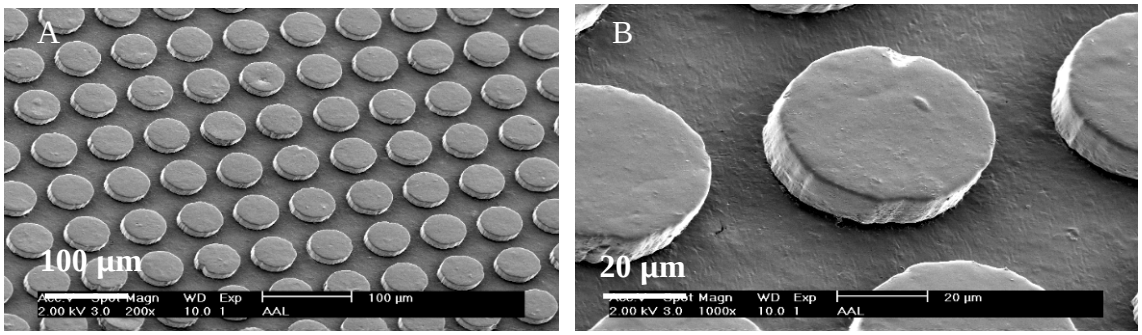

Figure 3.29. PU replicas molded using DMDCS height 23 µm, magnification A. 200x. B. 1000x.

These successful replicas generated replications of the other etched templates given in Table 3.4 using the same process. The replicas on the 25 µm diameter template and 35 µm diameter templates are shown in the SEM images (Figure 3.30 and 3.31) respectively. The resultant features were not fully developed because the template had some buildup of PU from pervious experiments, even after using the cleaning process described earlier. There seemed to be some difficulty in cleaning the templates with the smaller features.

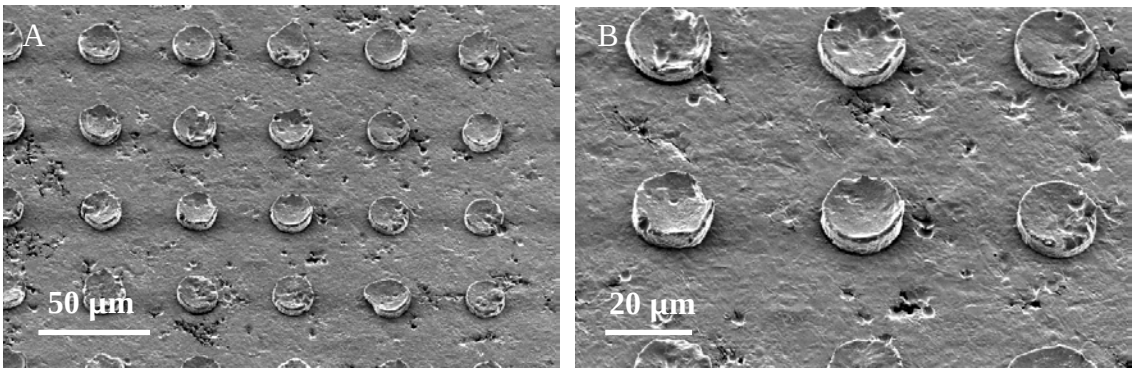

Figure 3.30. PU replicas molded using DMDCS diameter 18 µm, magnification A. 500x. B. 1000x.

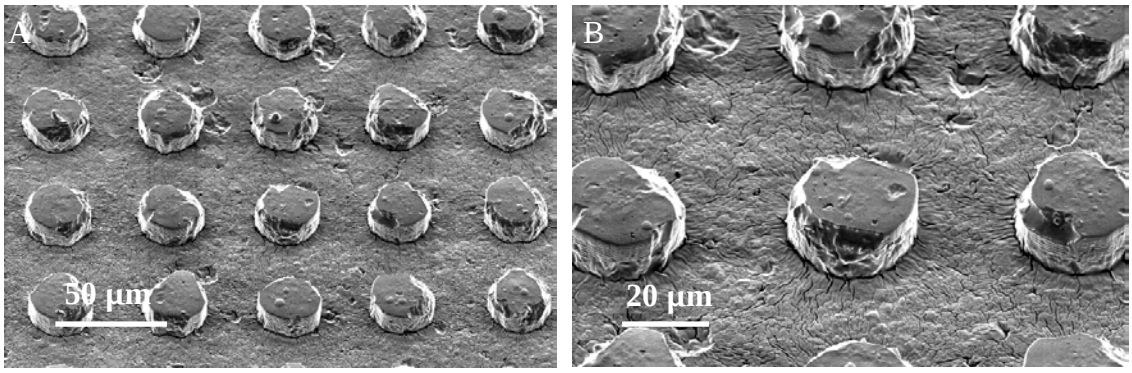

Figure 3.31. PU replicas molded using DMDCS diameter 35 µm, magnification A. 500x. B. 1000x.

An attempt could have been made to refabricate the smaller diameter templates, however there was a need for testing and charaterization of the already created good replicas. Thus, the replication experiment was repeated five more times on the 45 µm diameter, which achieved the same perfect replications described in Table 3.5. The features produced near perfect replicas for the 45 µm diameter, with heights of 12 and 23 µm as shown in Figures 3.32 and 3.33 respectively. It was also shown that Figure 3.33 with 23 µm pillars has surface features not perfectly cylindical. This arose from the slight under etching of the template in that particular area.

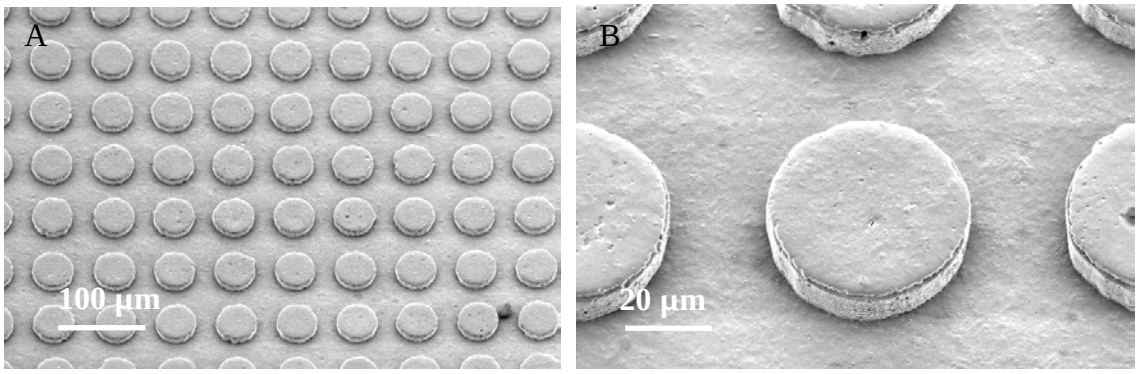

Figure 3.32. PU replicas molded using DMDCS height 12 µm, magnification A. 200x. B. 1000x.

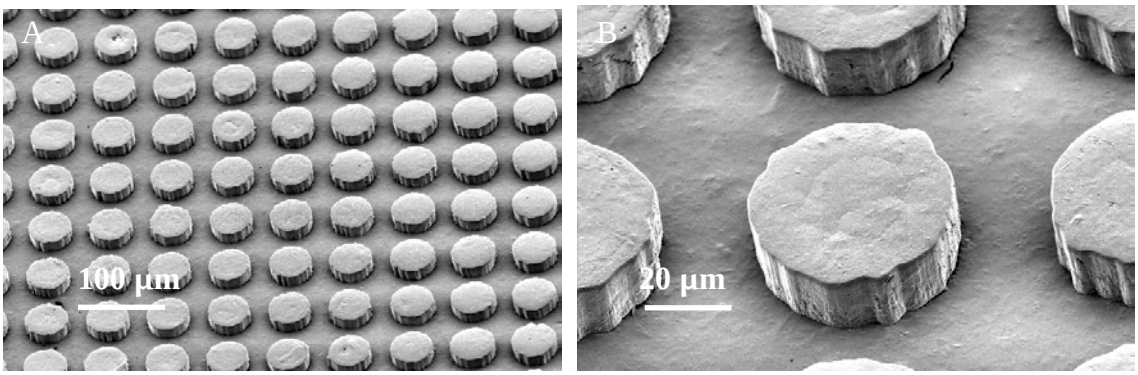

Figure 3.33. PU replicas molded using DMDCS height 23 µm, magnification A. 200x. B. 1000x.

A surface profilometer was used to ensure that the heights of the pillars matched the depths of the templates used. The surface scans for the height and pitch measurements produced were 12 µm and 23 µm as described in Figures 3.34 B and 3.35 B respectively. Figures 3.34 A and 3.35 A are the SEM images of the scanned PU surface. The results confirmed the precise measurements of the template given in Figures 3.9 and 3.10.

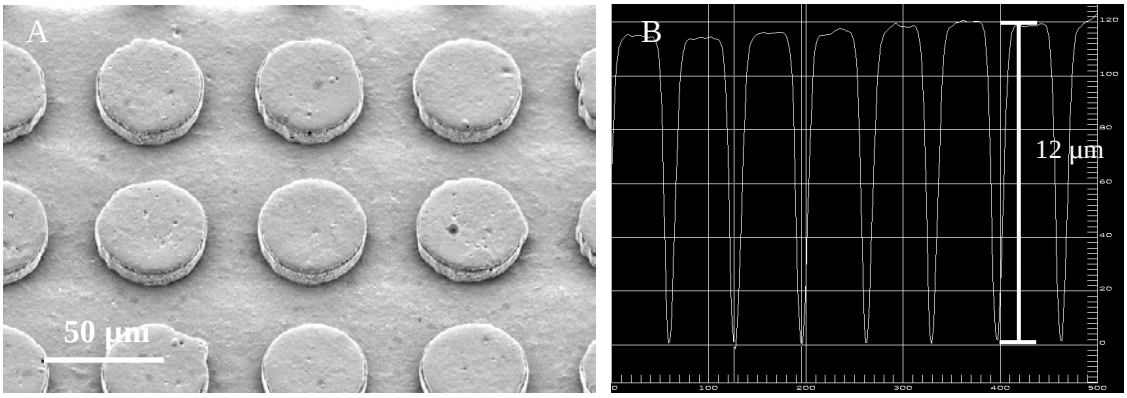

Figure 3.34. PU replicas molded using DMDCS height 12 µm, magnification A. 500x. B. Surface profile measurement of the shown PU replica.

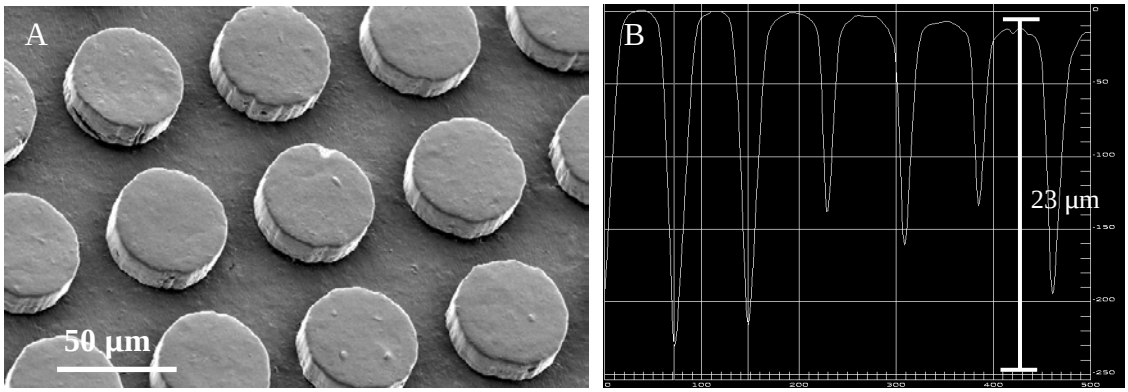

Figure 3.35. PU replicas molded using DMDCS height 23 µm, magnification A. 500x. B. Surface profile measurement of the shown PU replica

The conclusion from the soft lithography experiments was a process to mold surface texture onto the surface of PU. The successful replicas were formed through a process described in Figure 3.11. Using DMDCS as the release agent the molds that were created were described in Table 3.5. The created PU coupon in Figure 3.36 showed no aesthetic differences between the non surface texture and textured coatings. The reflection of light on the micro textured sample was due to the location of the image in proximity to the light.

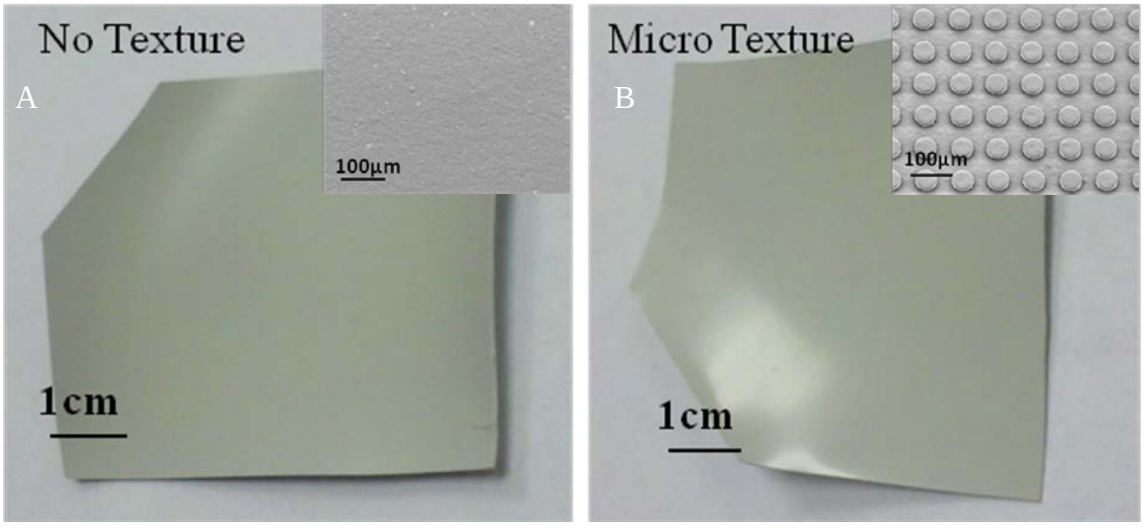

Figure 3.36. PU replica comparing the appearance. A. No surface texture with SEM image magnification 200x. B. Micron sized texture with SEM image magnification 200x.

3.1.5 Chemical Surface Texture

Chemical surface texturing of the PU coating was performed to complete the hierarchy roughness similar to that of the lotus leaf. The creation of submicron-nanometer roughness on the polyurethane samples by nitric acid (HNO_3) infiltration was described elsewhere in the literature.[67, 68] As described, the acid destroyed the PU surface on a submicrometer-nanometer scale due to the bond scissoring of the polymer chain boundary randomly on PU polymer surface. For this experiment, two concentrations of nitric acid by varying the times 0 – 60 minutes are described in Table 3.6. The samples were sonicated to ensure the movement in the bath. A variation of the concentration was used because the precise chemical composition of the PU was unknown.

The chemical surface treatment was initially preformed on the PU molded from the polished silicon wafer. The results were analyzed with AFM and SEM for the level of surface roughness and pitting. The four etch times using 1 molar HNO_3 solutions were

Table 3.6. Parameter matrix for the chemical surface treatment experiments.

PARAMETER MATRIX – Chemical Surface Treatment				
TEST CONDITIONS				
Treatment (HNO_3)	10 Molar Solution Under Sonication			
Treatment (HNO_3)	1 Molar Solution Under Sonication			
Timed Etch	0 min	10 min	30 min	60 min
Measurement Parameters				
Surface Roughness - Visual SEM imaging Surface Roughness - AFM				

imaged and showed no change in surface roughness as a function of etch time. The samples etched in 10 molar HNO_3 solution showed that the 0 and 10 minutes surface treatment did very little to the overall roughness. While the 10 molar HNO_3 solutions preformed that the 30 and 60 minutes surface treatment produced additional surface roughness, there was no discernable roughness change between these samples. Thus, the chemical surface texturing of nitric acid for 30 minutes under sonication was chosen as the method for surface treatment for all remaining tests. Figure 3.37 shows the SEM analysis of the chemical treatment on the molded flat PU replicated from the polished silicon wafer. Comparing the images to the non functionalized PU in Figure 3.26 it can be seen that there was increased micron sized surface roughness. To prove this statement, AFM was performed on the chemically treated flat PU mold in Figure 3.38. The surface roughness increased over the scanned area to a RMS roughness of 127 nm, Ra roughness 99 nm, and Rmax of 1.5 µm chemically treated from RMS of 100 nm, Ra of 78 nm, and a Rmax of 0.91 µm untreated. More importantly of the three dimensional AFM image shown in Figure 3.38B, very sharp peaks on the surface in the range of 1 µm where observed, which was an increase in roughness compared to the untreated PU replica, Figure 3.27

.

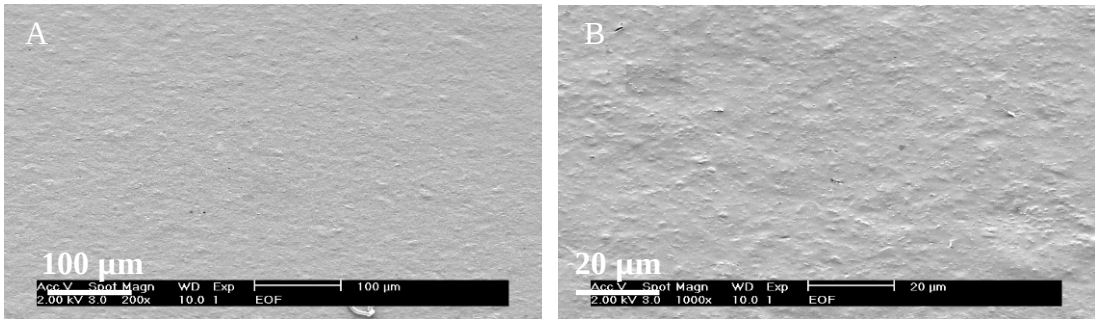

Figure 3.37. PU replicas molded from polished silicon wafer applied chemical treatment, magnification A. 200x. B. 1000x.

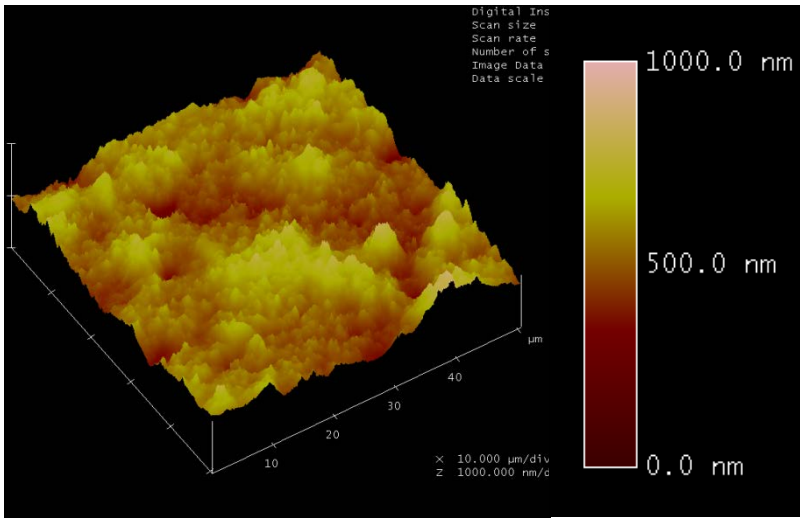

Figure 3.38. AFM topography, PU replicas molded from polished silicon wafer post chemical modification in a three dimensional view.

The analysis for the surface treatment of HNO_3 for 30 minutes was performed on molded surface textures described in Table 3.6. The results of the chemical treatment are shown for the textured in Figure 3.39 with 45 µm diameter, 70 µm pitch and height of 12µm, while Figure 3.40 having a height of 23 µm. The acid treatment performed a similar micrometer-nanometer roughness onto the textured samples. The introduced roughness of chemical treatment completed the dual hierarchy scale roughness of 45 diameter micron pillars with submicron-single micron surface pitting roughness.

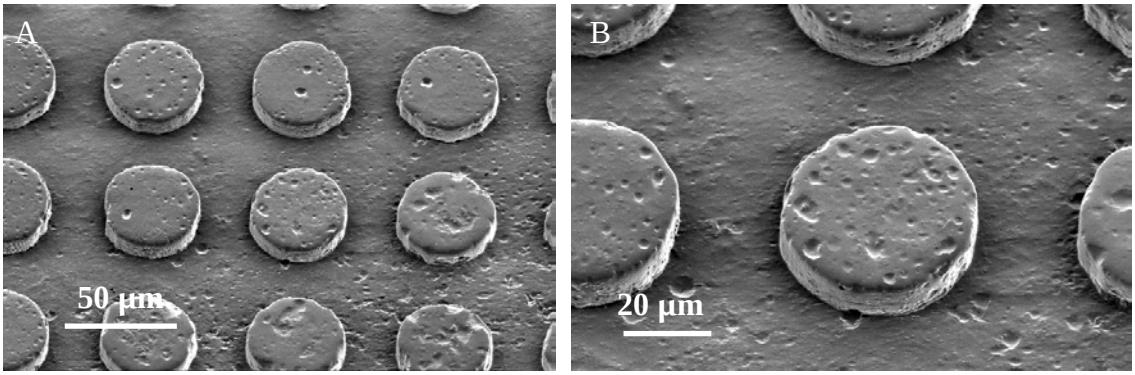

Figure 3.39. PU replicas molded height 12 µm post chemical treatment, magnification A. 500x. B. 1000x.

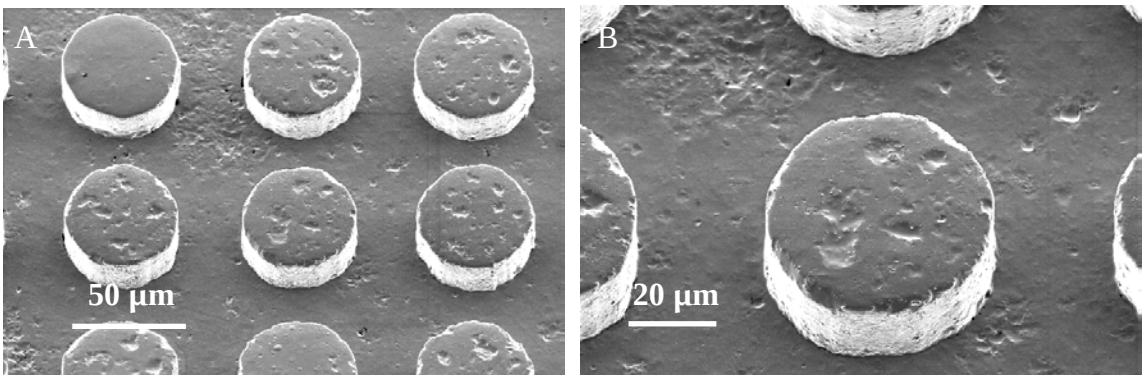

Figure 3.40. PU replicas molded height 23 µm post chemical treatment, magnification A. 500x. B. 1000x.

3.2 Contact Angle Measurements

Water Contact Angle (WCA) measurements were made with a Goniometer from Future Digital Scientific Corporation (Model OCA 20) as shown in the photos Figures 3.41 A and B. The Goniometer's basic function was to measure the contact angles between the water and substrate as described in Figure 1.7. This describes the level of hydrophobicity, as well as which state the droplet was in: Wenzel or Cassie-Baxter.

Water droplets of 3 µL were placed on the PU surfaces at the rotation point of the three point axis adjustable surface via a computer controlled syringe. The Camera in Figure 3.41 B allowed examination of how the droplet formed on the surface. Using the

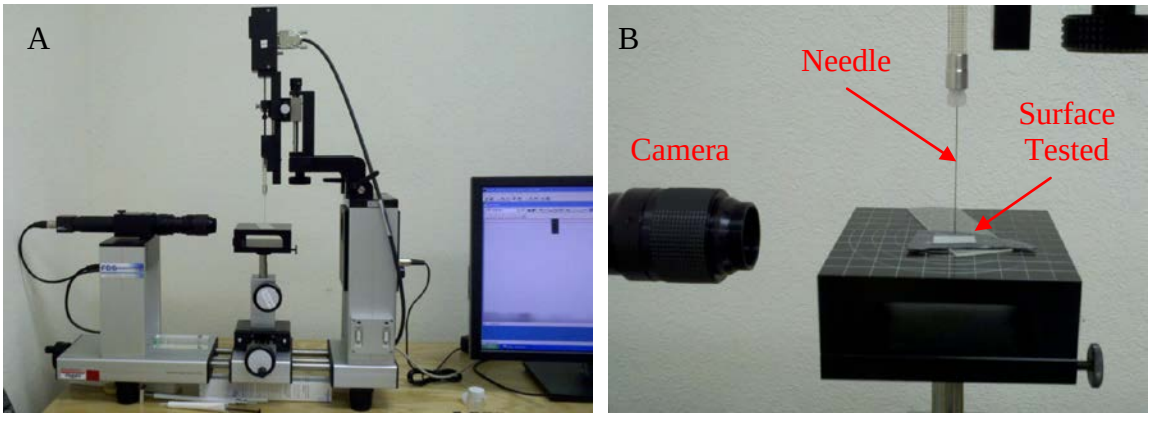

Figure 3.41. Goniometer setup used for WCA measurements. A. View of the entire set-up. B. View of the stage. Taken in Dr. Min Zou's Lab at the University of Arkansas

image that was displayed on the computer screen, it was possible to capture the droplet and measure the WCA. The syringe is accurate to within 0.1 µL per droplet.

For this experiment, the surfaces analyzed were molded flat PU, molded flat chemically functionalized PU, textured PU samples as described in Table 3.5, and textured PU with 45 µm diameter, 70 µm pitch with 23 µm height chemically functionalized with HNO_3 for 30 minutes. Four static WCA's from a single sample were averaged to find the mean angle for each element of the experimental matrix.

3.3 Ice Formation Tests

The purpose of the ice formation tests was to measure the time for the droplet to freeze onto the PU surfaces. The relationship between the static and dynamic test is shown in Figure 3.42. The static test is used to examine how the water interacts with the surface while freezing. This test does not account for extra form factors of the dynamic icing conditions for the wind turbine blade. The results provided insights that can be used in future works to help explain the dynamic conditions for droplet freezing. The dynamic test is dependent on droplet temperature, impact velocity and rotating dynamics.

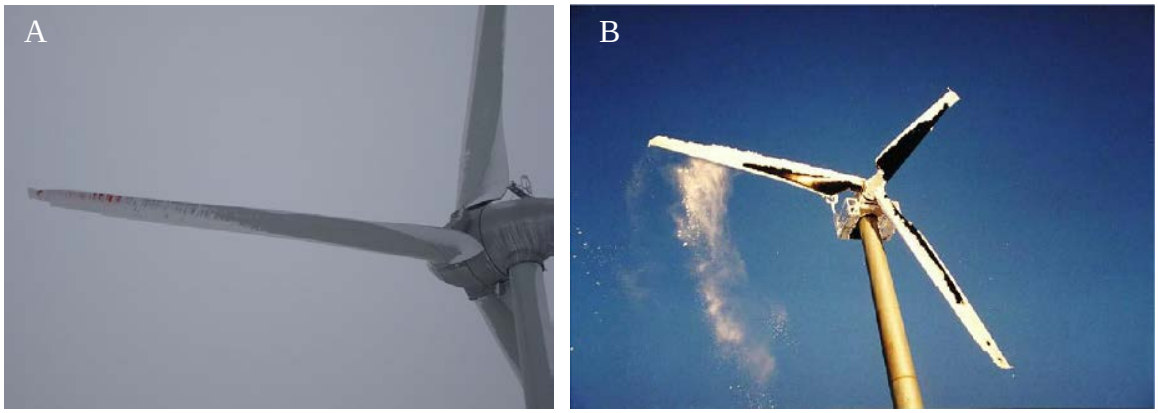

Figure 3.42. A. Static conditions for a wind turbine. B. Dynamic conditions for a wind turbine [69-70].

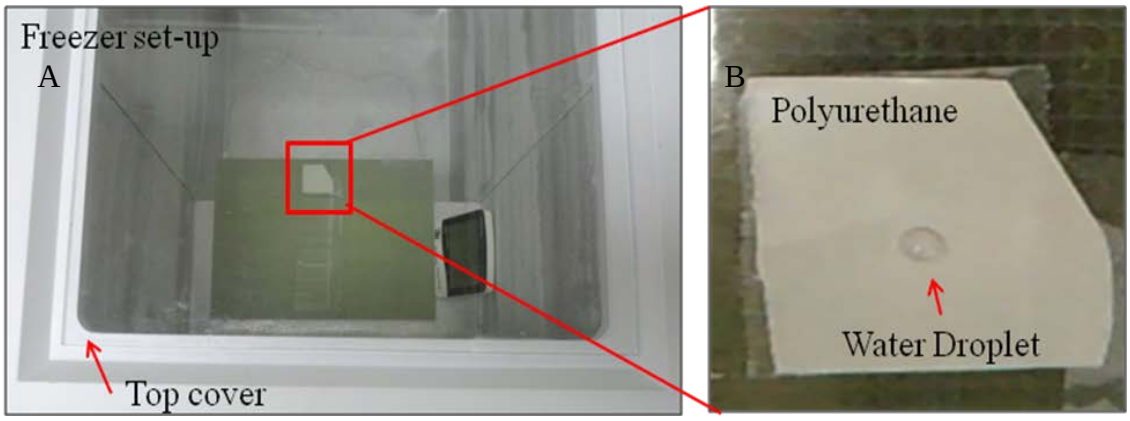

Figure 3.43. Static ice formation test setup. A. View of the entire freezer set-up. B. View of the droplet on the surface.

The static test displayed in Figure 3.43 is tested by placing a droplet of water on the surface of the PU from a syringe at a constant droplet size of 10 ± 0.5 µL. The droplet volume was found by weighing 20 droplets and assuming standard water density of 1 g/mL. The temperature of the ice chamber remained constant at -10 ± 1ºC. The freezing time of the water droplet was measured in the experiment.

Seven droplets were analyzed from one sample for each of the experimental matrix elements. The matrix included modifications on PU: flat, chemically modified flat, textured PU and chemically modified textured samples. The time for 21ºC tap water placed onto the stable cold surface to freeze was measured. Tap water was used due to the greater number of impurities to prevent significant undercooling as found in the DI water.

3.4 Brief Description of Analytical Techniques Used

3.4.1 Surface Profilometer

A Surface Profilometer measures the surface texture or topography of the material. This was a measure of the vertical changes along a single horizontal axis. The

profilometer scans the surface of the material by dragging a pointed probe along the line of measurement. The input of vertical variations was measured through a cantilever displacement that outputs as an electrical signal acquired, displayed as an output as shown in Figure 3.34.

In this thesis, a surface profilometer was used to measure the height and surface profile of the textured PU, as well as the templates created. The horizontal scanned along a 500 μm horizontal axis with maximum height measurement of 100 μm. The accuracy of the measurement was within ± 250 nm due to the finite sharpness of the scanning tip.

3.4.2 Scanning Electron Microscope (SEM)

The Scanning Electron Microscope (SEM) uses an electron beam to image the surface topography of a material. Electromagnetic lens focuses the electrons to specific areas on the sample being imaged. The benefit of SEM over optical microscopy was that the samples did not need to be reflective and typical magnification can image features down to the nanometer scale, 100,000x magnification. FEI Company-XL30 ESEM equipment was used in this thesis to image the created surface textures onto the PU surface. ESEM stands for Environmental Scanning Electron Microscope and works similarly to the SEM. The difference was the broader range of materials which could be imaged, including nonconductive samples. Even with this equipment benefit, the PU samples were coated with 5 nm of Au/Pd particles to make the sample conductive and produce images of less surface charging. In this thesis a low electron voltage of 2 keV was used due to the non-conductivity of the samples. All images were taken at an angle of 30 degrees normal to the surface. This technique was employed to clearly image the changes of the textured samples in a qualitative fashion.

3.4.3 Atomic Force Microscope (AFM)

The Atomic Force Microscope (AFM) uses a cantilever and functions similar to the profilometer. However, the AFM tip is on the order of single nanometers and the cantilever vertical deflections are measured through the laser diffraction from the cantilever connected to the pointed probe facing the surface. In the tapping mode used in this thesis the tip does not come into contact with the surface but within 10 nm. Electrostatic and Van der Waals force cause some deflection in the AFM tip. The tip was then set to scan an area of 50 x 50 μm and the output of the surface scan was as shown in Figure 3.27. The benefits of AFM over the surface profilometer was the ability to image small features of 100,000x, limited only by diameter of the tip and environmental conditions. While the disadvantage as found in this work was the ability to measure height differences of greater than 5 μm. The accuracy in the x and y direction of the tool is ± 25 nm and the z direction is ± 5 nm.

3.4.4 Optical Microscope

Optical microscopy depends of the light reflected from the surface of the image as seen through a series of optical lens. A Nikon Epiphot 200 was used to image initial samples including the laser machined samples, photolithography masks and created templates. The Nikon microscope was limited to these uses because the precise imaging needed for the PU samples were unable to reflect the light required to observe the surface features. The benefits of the optical microscope over the SEM was the speed of imaging, while it was limited to only 1000x magnification, and by the reflective nature of the sample imaged.

Chapter 4: Results and Discussions

4.1 Contact Angle Measurement Results

The measured WCA was the angle at which the water droplet surface met the surface of the PU. A comparison is shown in Figure 4.1 between the WCA prior to chemical modification between the molded flat, initial irregular formation of 45 µm diameter with 12 µm height pillars (TMCS as the release agent), and the perfect formation of the 45 µm diameter with 12 µm height pillars (DMDCS as the release agent). The WCA is shown on the left and the SEM image is to the right in Figure 4.1. These images showed that there was a higher contact angle from the textured surfaces. The contact angles were 88°, 113° and 144° Figure 4.1 A, B, and C respectively for the PU substrates. More specifically, the results showed the droplet transition from the Wenzel regime full wetting of the surface features in Figure 4.1 B, to the Cassie-Baxter regime wetting only on top of the pillar formation in Figure 4.1 C. This result was critical in creating a surface that was more hydrophobic with less surface wetting. More wetting implies that there will be an increase in the surface to water contact (WC), thus increasing the mechanisms of adhesion. Lower WC in the Cassie-Baxter state will decrease the surface adhesion mechanisms and avoid the increase in mechanical interlocking that inhibits the ice from detaching from the surface. The design for the surface texture was intended to limit the mechanisms for adhesion while providing less surface area contact for the droplet to freeze by decreasing the conductive heat transfer from the water to the surface of the wind turbine blade.

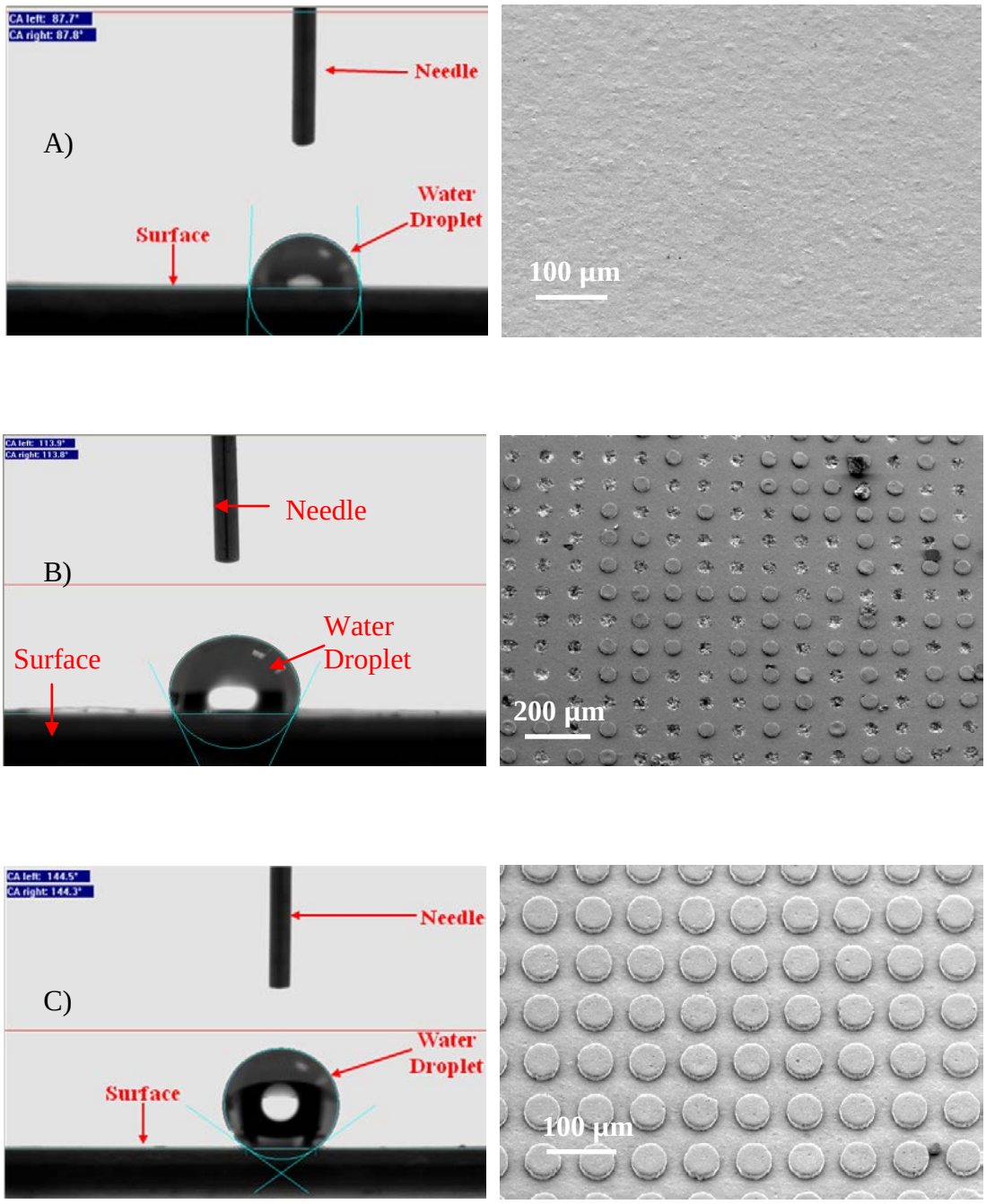

Figure 4.1. A. WCA image of PU replica from a polished silicon wafer using DMDCS magnification 200x. B. WCA image of PU replica from 45 µm diameter mold using TMCS, magnification 100x. C. WCA image of PU replica from 45 µm diameter mold using DMDCS, magnification 200x.

WCA results were analyzed comparing the molded flat PU surface to the textured PU surface. The water droplets were obseved to remain in the Cassie-Baxter state for the pillared features which resulted in an increase in the WCA. Figure 4.2 showed an average of a 60% increase between these surfaces respectively. The graph displayed was a box and wiskers plot of the upper quartile (top 75%) and lower quartile (bottom 25%) with error bars extending to the greatest and least measurement achieved.

The replicated surface textures using DMDCS (perfect replicas) as depicted in Table 4.3 were analyzed by measuring the static WCA. The increase in pitch and pillar height were the variables. It was expected that pillar pitch and height variation should not have an effect on the WCA as long as the water droplet remained in the Cassie-Baxter state. The similarity was expected because the angle at which the droplet sits was the

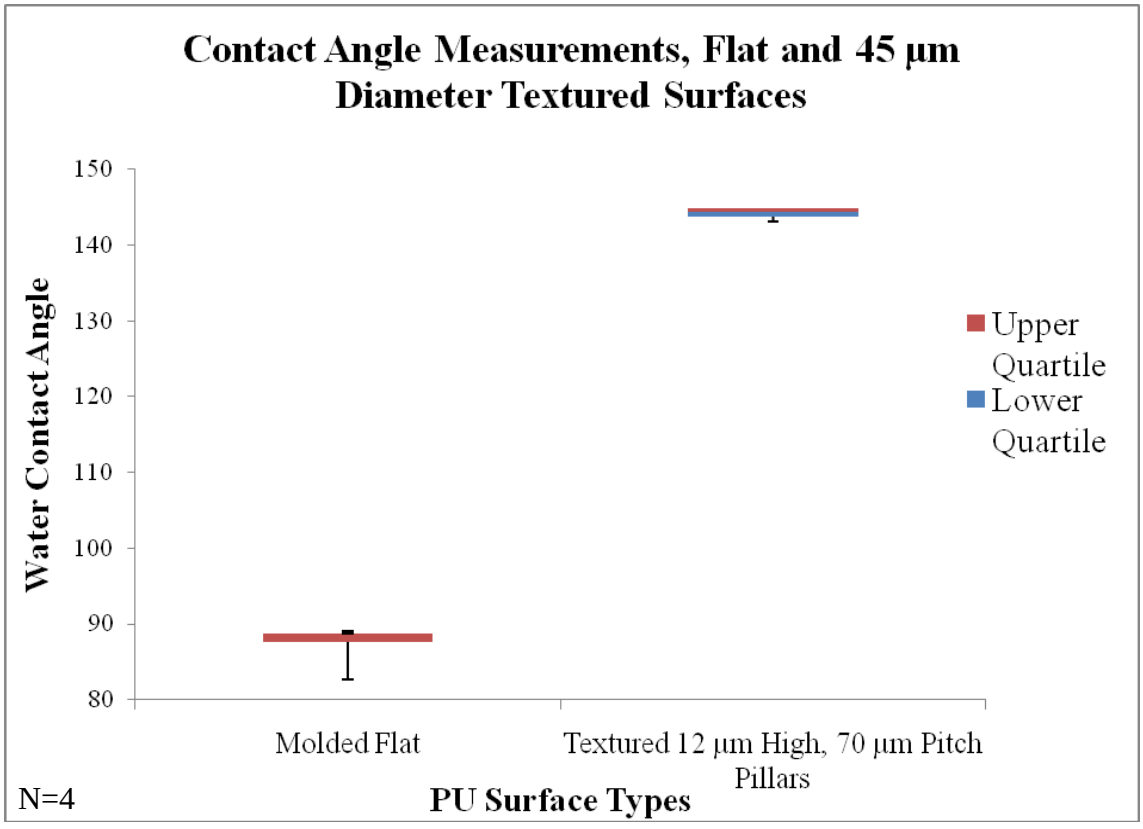

Figure 4.2. WCA measurements on PU comparing the flat to the textured PU surface

same on the pillar geometry, because they were of the equal pillar diameters. However, the goal was to vary the pitch and height was to find the lowest heat conduction through the pillars that the water will be in contact. The WCA measurement remained near 140° for all the surfaces tested shown in Figure 4.3. The results also showed the water droplet remained on top of the pillar formation keeping them in the Cassie-Baxter regime. The data were collected from a single sample for each variation. Displayed are the four measurements obtained for each element.

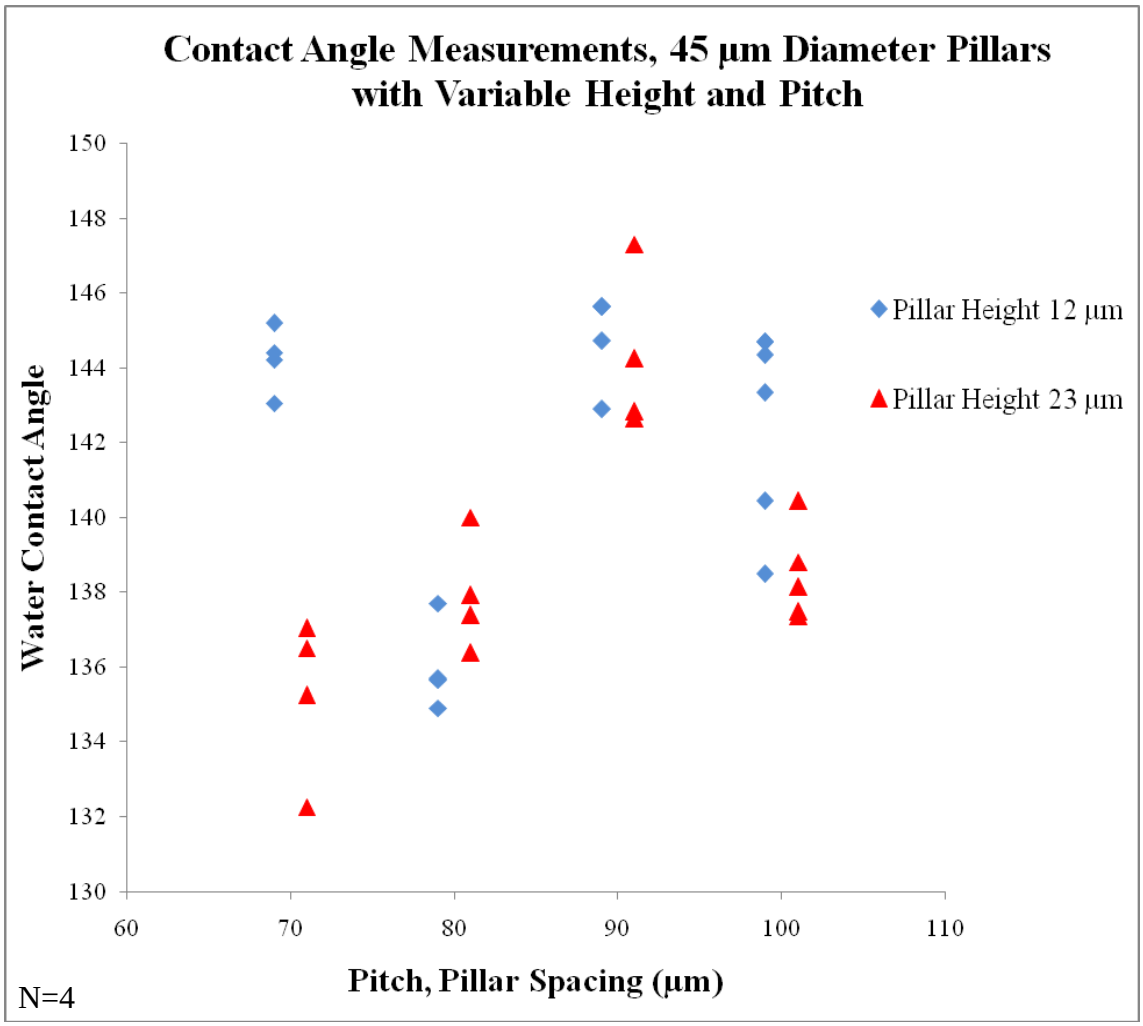

Figure 4.3. WCA measurements on PU with variable pillar pitch and height using DMDCS release agent. Pitch is equal for both heights but separated for clarity.

To evaluate the impact of the chemical texture on the PU, a comparison was made between the chemically modified molded flat and chemically modified textured PU. Figure 4.4 shows the WCA of the chemically functionalized surfaces on the flat and textured. The WCA was shown on the left and the SEM image of the surface to the right. It was observed that the WCA did not change significantly from the flat surface (WCA 88°) to (WCA 91°) on the functionalized surface. There was a decrease in WCA from the textured surface (WCA 138°) to (WCA 134°) on the functionalized surface. The expectation that a dual hierarchy micro-nano structure would create a higher WCA and lower wetting was not met. It was visually observed during the WCA measurement (Figure 4.4) that on the dual textured PU surface the wetting conformed to portions of the

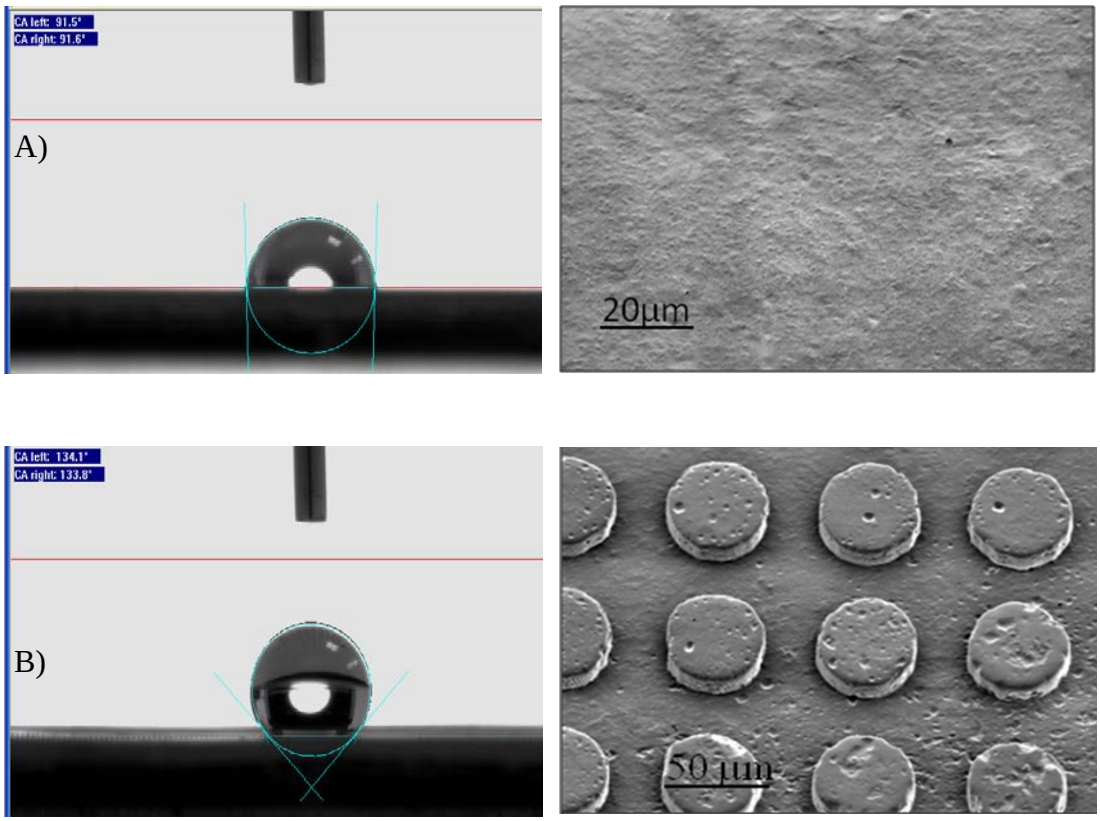

Figure 4.4. A. WC image of PU replica post chemical treatment from a polished silicon wafer using DMDCS magnification 100x. B. WC image of PU replica post chemical treatment from 45 µm diameter mold using DMDCS, magnification 500x.

PU surface, thus creating the unwarranted transition to the Wenzel Regime (full wetting).

There was a discernable impact from creating functionalized flat molded or a textured structure shown in Figure 4.4. Figures 4.5 and 4.6 compared the WCA of the flat and textured PU surfaces versus their functional counterparts. The graphs displayed that there were no discernable change in the WCA between each surface. A similar interaction was shown for all pitch and height samples however; experiments were not fully characterized because of the disadvantageous results. Moreover, the surface morphology of the lotus leaf that was examined may not only rely on a dual scale hierarchy that decides the large WCA, but the combination of surface feature and chemical composition. Or, it may be inferred the hierarchy does indeed play a role, rather the scale of 45 µm features with much smaller submicron additional functional submicron features

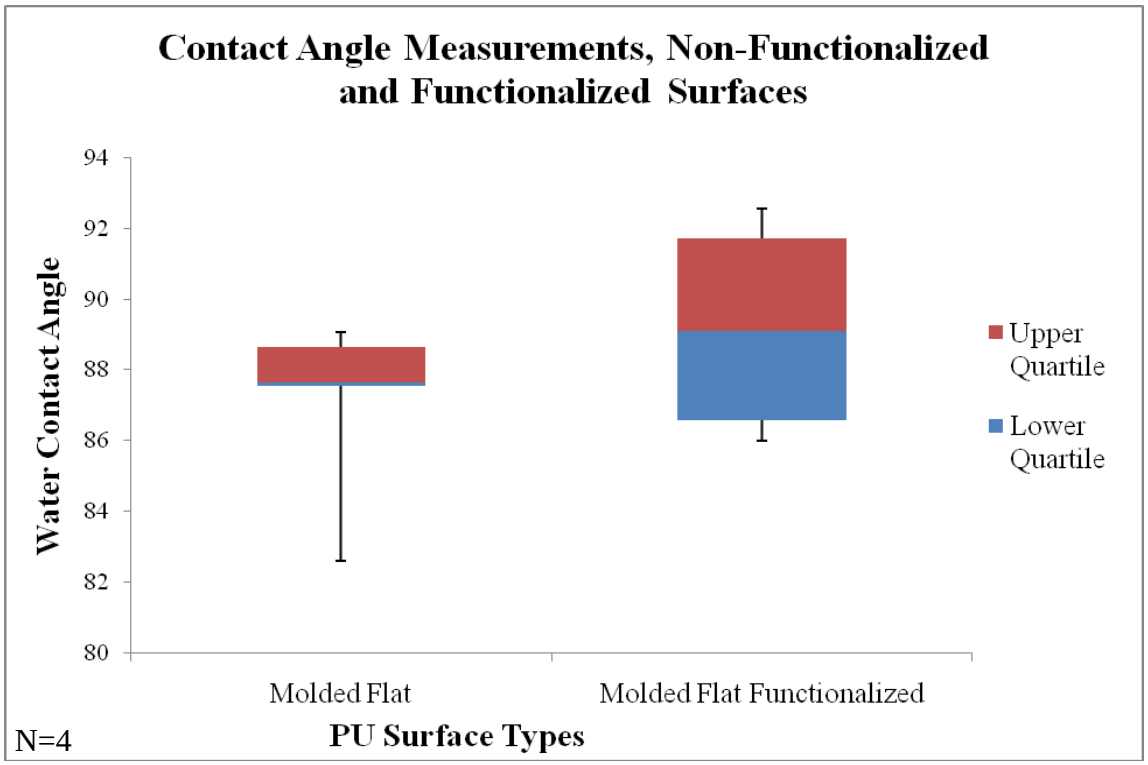

Figure 4.5. WCA measurements comparing the effect of chemical treatment on flat PU surfaces.

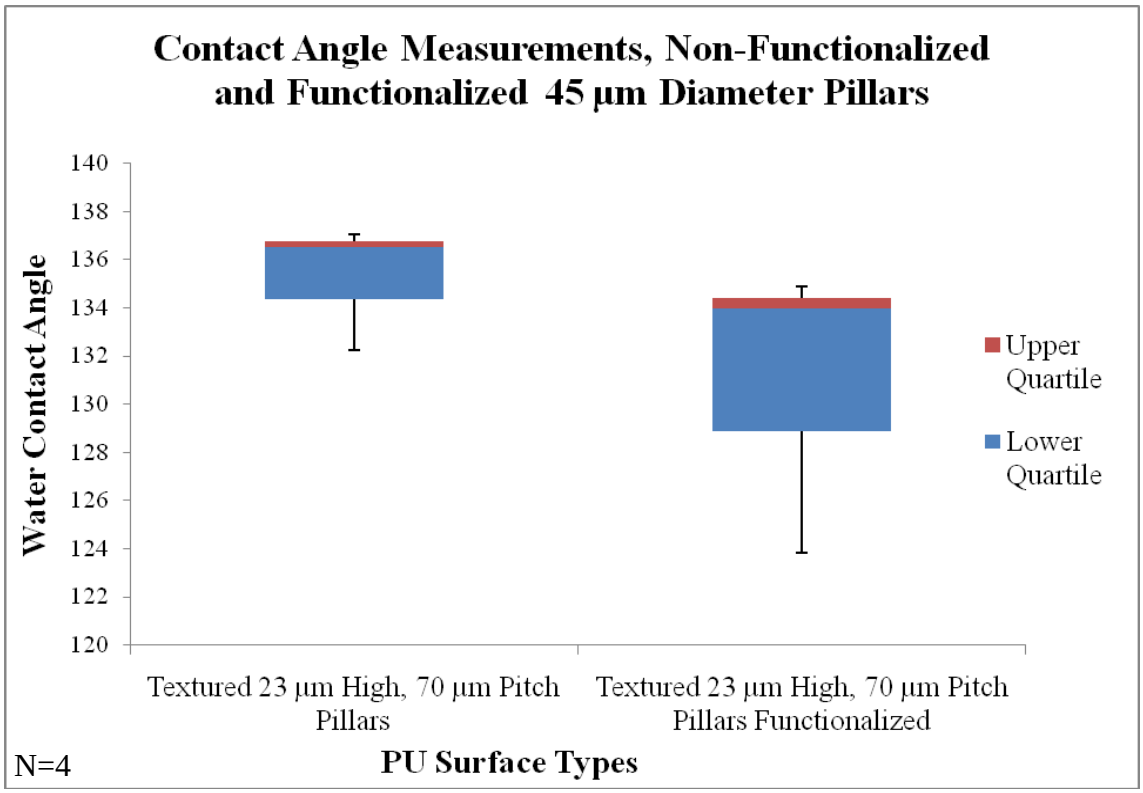

Figure 4.6. WCA measurements comparing the effect of chemical treatment on textured PU surfaces.

have no benefit. Although one of these may be the interaction, more testing would be needed to determine which factors play strong roles.

4.2 Droplet Freeze Time Results

Water droplet freeze times were recorded with a video recorder mounted within the freezer setup. Figure 4.7 displayed time to freeze on the flat PU replica as labeled with the time scale. At time 0 seconds, the water droplet was placed on the PU. At time 5 seconds, the water droplet shows the reflection unchanged from the start time. At time 75 seconds, the water droplet shows a change in reflection because it begins to freeze. At time 90 seconds, droplet shows a complete change of internal reflection. The water droplet's light reflection was completely distorted once frozen at time 90 seconds, thus giving the time to freeze for the water droplet with an error of ± 1 second for recording.

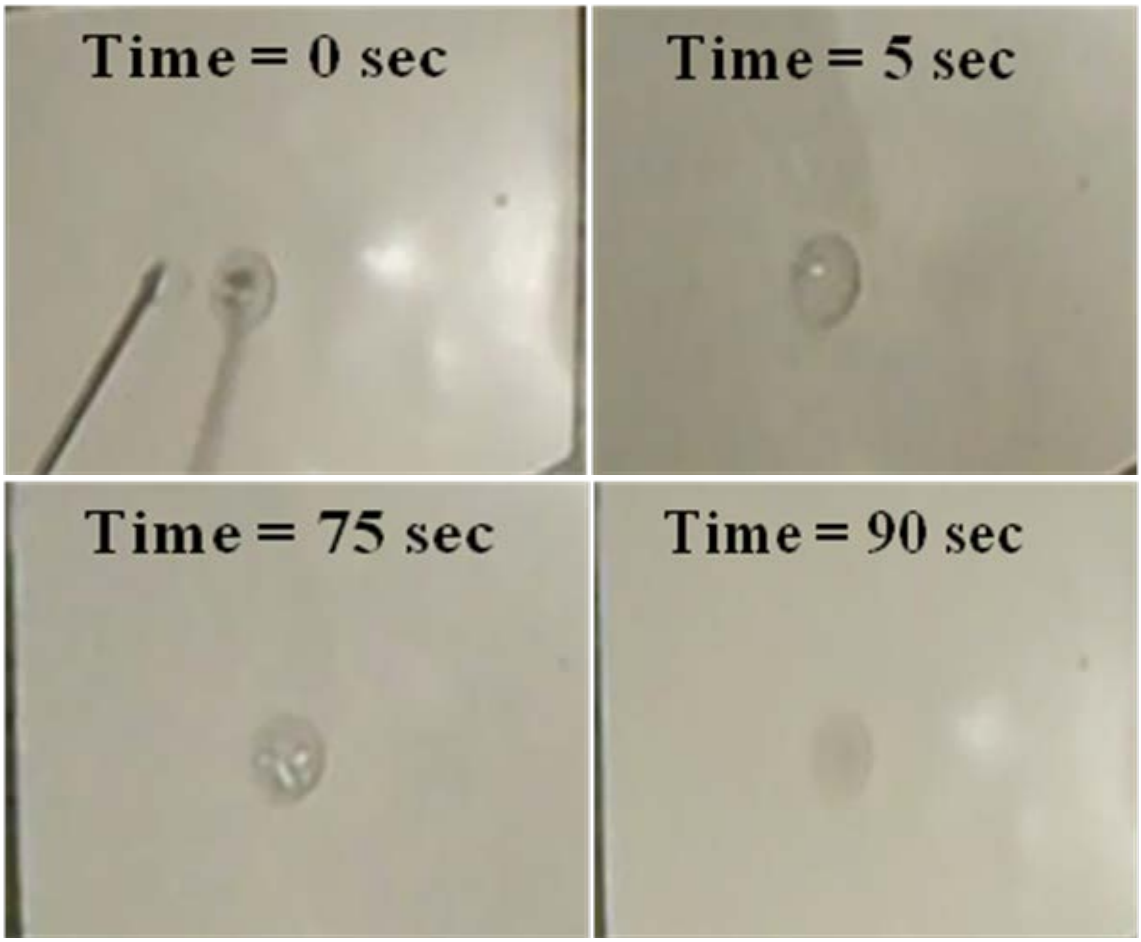

Figure 4.7. Water droplet freezing observed through the change in light reflection.

Using the controlled droplet size already described in Section 3.5, the freeze time was measured on the various PU samples as shown in Figure 4.7. The molded flat sample compared to the chemically treated molded flat PU gave a similar median time to freeze of 90 sec. The higher variation of the upper and lower measurement was due to the way the water droplet conformed onto the surface feature. The chemically functionalized flat surfaces were shown to have a higher roughness described between Figures 3.27 and 3.28. The submicron-nano roughness will enable the droplet to either conform to a greater surface area or conform to a lower surface area over the induced roughness. The randomness of the roughness created from the chemical modification

differed over the surface, thus creating a difference in the upper and lower bounds in freezing time. The difference over these areas was the water conforming and propelling respectively.

The WCA measurements of the textured chemically functional surface showed a decrease of contact area and partial transition from the Cassie-Baxter state to the Wenzel state. The freezing time over this surface was expected to decrease the freeze time as compared to the textured non-chemically functional surface. There is no discernable data to show the effect of chemically texturing over each of the surfaces.

The partial objective of the thesis was achieved as shown in Figure 4.8 delayed freezing time from the flat to textured PU surface. Due to the water droplets reduced area

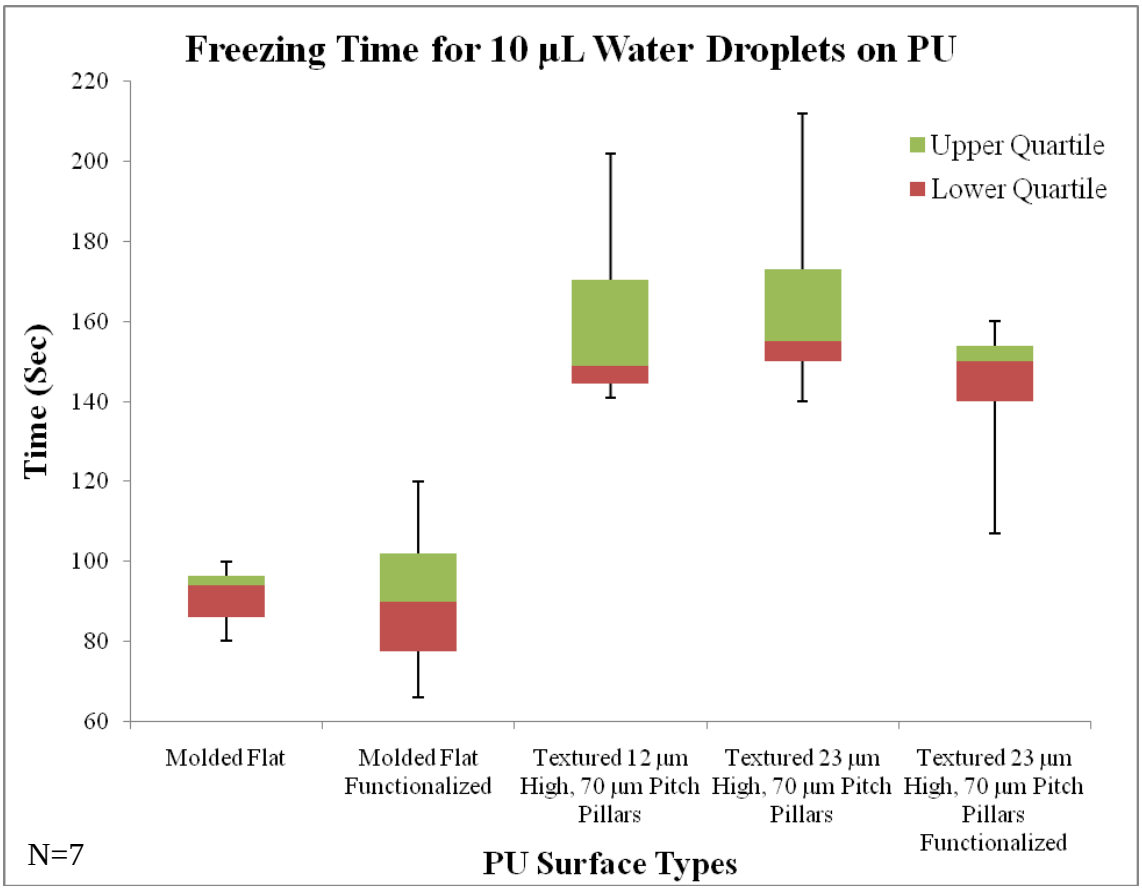

Figure 4.8. Water droplet freezing delay on textured surface.

the flat. Up to 20% deviation was shown for the given measurements. Comparing with of contact to the PU on the textured surface, there was a freeze time delay compared to the literature [32], this was a common variation. The error associated can be drawn from the precise temperature and size of the droplet that play into this value.

The textured PU samples showed an 80% delay in the time to freeze. The increase from 90 seconds on the flat PU to 160 seconds was an increase that could have application to coatings on wind turbine blades. A surface texture created on the blades' PU coating could delay the glaze ice from solidifying on the blades' surface, and thus limit a major destructive form of icing. However, more testing with dynamic icing conditions is needed to confirm this hypothesis.

The mechanism for the freeze delay was the area of water to surface contact, as explained below. There was a slight decrease in the chemical treatment on the textured PU sample. It was found that the droplet began to transition into the Wenzel state as recorded in the WCA measurements. This enabled the increase the area in water to PU contact. The fraction in droplet area can be calculated from the unit cell of the sample. The fraction of water in contact on the texture surface was found through Equation 4.1:

$$\frac{Area\ of\ the\ Pillar}{Area\ of\ the\ Unit\ Cell} = \frac{(D/2)^2 * \pi}{P^2} \qquad \text{(Equation 4.1)}$$

where the diameter of the pillar, *D*, and spacing of the unit cell, *P*, are described in Figure 4.8. The water will sit on less of the surface of the textured sample as compared to the flat given by the ratio in Equation 4.1. This leads to a decrease in area for heat of conduction (Fourier's law) given in Equation 4.2 [71]:

$$\frac{Q}{t} = \frac{\kappa A \Delta T}{d} \qquad \text{(Equation 4.2)}$$

where the amount of heat transferred, Q, over time, t, is the thermal conductivity, κ, times the area, A, and change in temperature, ΔT, divided by the thickness, d. The experimental area, A, varies indirectly with time, t. Cooling due to convection was disregarded because researchers have found conduction was the major component of cooling [32].

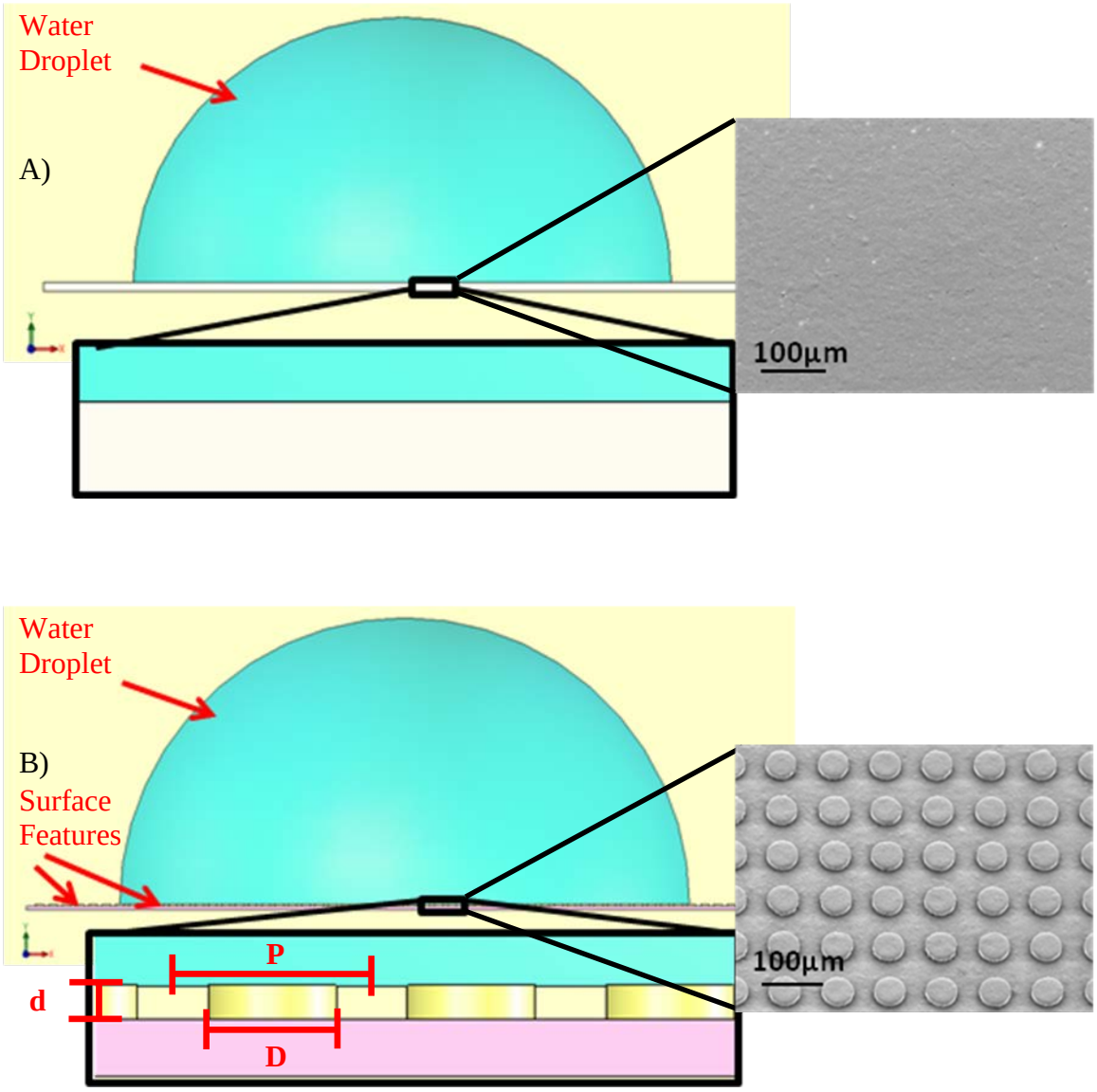

Figure 4.9 Diagram of a water droplet on A. Flat PU surface with SEM image magnification 200x. B. Pillared PU surface with SEM image magnification 200x.

Chapter 5: Conclusion and Future Work

5.1 Conclusion

This work shows a successful replication of 45 μm pillar diameters with various pitches on the surface of the PU. The PU surface features offer the advantage of providing the textured material with a superior hydrophobic surface. The WCA showed an increase of 60% on the replicated PU with the pillared features as compared to the flat PU. The WCA increase propelled the water from the surface, forcing the droplets to bead-up on the tops of the pillars. The increase of pitch spacing between the pillars showed no transition from the Cassie-Baxter to Wenzel state. This finding plays an important role on the freezing mechanism of the water on the surface. The water droplet was in less contact with the surface texture, thus the freezing mechanism of conduction was limited. The limit in contact area decreased the freezing time for a single droplet by 80%. The delay in droplet freeze time can enhance the prevention of glaze icing on a wind turbine. This method can be implemented in the wind turbine coating industry by applying a patterned template to the PU coating during the curing process.

5.2 Future Work

1. Creation of more functional surface features: In this work, it was shown that it was feasible to replicate surface features onto PU material. The method may be advanced through the replication of a dual hierarchy structure that more closely follows the dimensions of the lotus leaf. The additional submicron features can be created through a shot pinning of particles onto the replicated surface structure.

To gain a more hydrophobic surface, a chemical passivation of the surface can be accomplished with a low surface energy material such as Polytetrafluoroethylene (Teflon).

2. Characterization of how the water moves on the surface structure: This work gave detailed testing on the static WCA of the droplet on the surface of the PU. To fully understand how the water interacts while moving, a contact angle hysteresis must be measured. That is, the forward and receding contact angles during the movement of the droplet on the surface. Findings with low contact angle hysteresis (5-10°) show the water to be free flowing from the surface. This test could be furthered to show if the surface can be self cleaning (water picks up particles as it moves from the surface).
3. Fully characterize the static icing conditions: This work provided the fundamental measurements that proved the textured surface will delay ice freezing. The remainder of the surface features with the various pitch need to be analyzed for the freezing times of water on the surfaces. Tap water was initially used in this experiment and the final tests should be completed with rain water from the particular area the turbine is placed.
4. Testing of the dynamic icing conditions: This work studied the static conditions of a droplet freezing on the various created surfaces. A correlation to how the droplet will act on the blades surface can only be hypothesized. Dynamic testing of water impact velocities at various temperatures is needed to prove the coatings will act as a freezing inhibitor. Also, tests with rain water should be done because the different surface properties as compared with tap and DI water.

5. Explore the role of chemical functionalization on the surface of PU: This research surface texturing with nitric acid may have advertently left functional residues on the surface such as hydroxyl groups. More testing is required to prove these functional groups are preventing the formation of ice on the surface or as an attractive force to adhere the ice to the surface.

References

1. U.S. Department of Energy. Retrieved May 23, 2011, from http://www1.eere.energy.gov-/windandhydro/wind_how.html

2. Mohamed et al. (2010) Renewables Global Status Report. 53-54

3. Naturstrom-Euphorie. Retrieved May 23, 2011, from http://www.aweo.org/windsize.html

4. Noise and Health. Retrieved May 23, 2011, from http://concernedcitizens.homestead.com/-windfarms.html

5. Kensche et al. (2006). Fatigue of composites for wind turbines. *International Journal of Fatigue, 28*(10), 1363-74.

6. Kong et al. (2005). Structural investigation of composite wind turbine blade considering various load cases and fatigue life. *Energy, 30*(11-12), 2101-14.

7. Rumsey et al. (2008). Structural health monitoring of wind turbine blades. *Smart Sensor Phenomena, Technology, Networks, and Systems 2008, 6933* 69330-1.

8. Henrik. (1999). The wind turbine components and operation. Retrieved May 23, 2011, from http://www.windmission.dk/workshop/BonusTurbine.pdf.

9. Google Images. Retrieved May 23, 2011, from http://static.howstuffworks.com/gif/wind-power-wind-flow.gif

10. *The future of wind power*. Retrieved May 23, 2011, from http://windy-future.info/2009/10/17/wind-turbine-generator/

11. Knudsen et al. Corrosion protection of offshore wind turbines – long life protective coatings**.** *Materials and Chemistry*

12. Rudling et al. (2009). U.S. Patent application 20090246033. Washington, DC: U.S. Patent and Trademark Office

13. Parent et al. (2010). Anti-icing and de-icing techniques for wind turbines: Critical review. Cold Regions Science and Technology. Volume 65, Issue 1, January 2011, Pages 88-96

14. Seifert. Technical requirements for rotor blades operating in cold climate. Retrieved May 23, 2011, from http://www.dewi.de/dewi/fileadmin/pdf/publications/ - Magazin_26/boreas_vi_seifert_01.pdf

15. Kelly Aerospace thermal systems. Retrieved May 23, 2011, from http://www.kellyaerospace.com/wind_turbine_deice.html

16. Zhao et al. (2009). Research on fault mechanism of icing of wind turbine blades. *WNWEC 2009*, 4.

17. Hochart et al. (2008). Wind turbine performance under icing conditions. *Wind Energy, 11*(4), 319-33.

18. Petrenko et al. (1999). Reduction of ice adhesion to stainless steel by ice electrolysis. *Journal of Applied Physics, 86*(10), 5450-4.

19. Rolls et al. (2000). U.S. Patent 6,145,787. Washington, DC: U.S. Patent and Trademark Office

20. Battisti et al. (2006). Warm-air intermittent de-icing system for wind turbines. *Wind Engineering, 30*(5), 361-74.

21. LeMieux et al. (2007). U.S. Patent 7,217,091. Washington, DC: U.S. Patent and Trademark Office

22. Battisti et al. (2010). U.S. Patent 7,637,715 B2 Washington, DC: U.S. Patent and Trademark Office

23. Cao et al. (2009). Anti-icing superhydrophobic coatings. *Langmuir, 25*(21), 12444-12448.

24. Kuinich & Farzaneh. (2011). On Ice-releasing properties of rough hydrophobic coatings. Cold Regions Science and Technology. Volume 65, Issue 1, Pages 60-64

25. Kulinich & Farzaneh. (2009a). How wetting hysteresis influences ice adhesion strength on superhydrophobic surfaces. *Langmuir, 25*(16), 8854-8856.

26. Kulinich & Farzaneh. (2009b). Ice adhesion on super-hydrophobic surfaces. *Applied Surface Science, 255*(18), 8153-8157.

27. Safaee. (2008). Nanostructured metal surfaces and their Passivation for superhydrophobic and anti-icing applications.

28. Tourkine et al. (2009). Delayed Freezing on Water Repellent Materials. *Langmuir*, 25(13), 7214–7216

29. Zwieg et al. (2007). Novel Biomimetically Based Ice-Nucleating Coatings. International Journal of Materials Research 98.7: 597-602

30. Gou et al. (2008). Frost formation on a bionic super-hydrophobic surface under natural convection conditions. *Heat Transfer-Asian Research, 37*(7), 412-20.

31. Karmouch et al. (2009). Icephobic PTFE coatings for wind turbines operating in cold climate conditions. *2009 IEEE Electrical Power & Energy Conference (EPEC 2009)*, 6.

32. Kietzig et al. (2009). Ice friction: The effects of surface roughness, structure, and hydrophobicity. *Journal of Applied Physics, 106*(2), 024303 (7 pp.).

33. Matsumoto & Daikoku. (2009). Fundamental study on adhesion of ice to solid surface: Discussion on coupling of nano-scale field with macro-scale field. *International Journal of Refrigeration, 32*(3), 444-53.

34. Sarkar & Farzaneh. (2009). Superhydrophobic coatings with reduced ice adhesion. *Journal of Adhesion Science and Technology, 23*(9), 1215-37.

35. Wang et al. (2009). A facile superhydrophobic surface for mitigating ice accretion. *2009 IEEE 9th International Conference on the Properties and Applications of Dielectric Materials (ICPADM 2009)*, 150-3.

36. Park et al. (2010). Bioinspired holographically featured superhydrophobic and supersticky nanostructured materials. *Langmuir, 26*(3), 1468-1472.

37. Wang et al. (2009). Investigation on hydrophobicity of lotus leaf: Experiment and theory. *Plant Science* 176, 687–695

38. Vieru. (2009). Super Buoyant Material Can Hold a Horse. Retrieved May 30, 2011. from http://news.softpedia.com/news/Super-Buoyant-Material-Can-Hold-a-Horse-106674.shtml

39. Valli. (2008). 10 Product Designs that are Inspired by Nature. Retrieved May 30, 2011. from http://scienceray.com/technology/information/10-product-designs-that-are-inspired-by-nature/

40. Fearing. (2008). Smart Gecko Tape. Retrieved May 20, 2011. from http://robotics.eecs.berkeley.edu/~ronf/Gecko/interface08.html

41. Cohesive Blue, Inc. (2011). Retrieved May 23, 2011, from http://strider-ss.com/strider.html

42. Ecological Problems. (2007). Retrieved May 23, 2011, from http://ecological-problems.blogspot.com/2007/12/endangered-animals-sharks.html

43. Flickr. Retrieved from http://www.flickr.com/photos/macprohawaii/5300421907/

44. Clark. Sustainable Design Update. Retrieved May 23, 2011, from http://sustainabledesignupdate.com/2008/04/inspired-by-nature-biomimetics-update/

45. Liu et al. (2010). Recent developments in bio-inspired special wettability. *Chem. Soc. Rev.*, 39, 3240–3255

46. Song et al. (2007). Superhydrophobic surfaces by dynamic nanomasking and deep reactive ion etching. *Proceedings of the Institution of Mechanical Engineers, Part N (Journal of Nanoengineering and Nanosystems),* 221(2), 41-8.

47. Song et al. (2009) Superhydrophobic Surfaces Produced by Applying a Self-Assembled Monolayer to Silicon Micro/Nano-Textured Surfaces. *Nano Res* 2: 143 150

48. Noormohammed. (2009). Nanostructured Thin Films for Icephobic Applications

49. Dybbro & Mukha. (2003). Retrieved May 23, 2011. from http://bhs.smuhsd.org/sciencedept/marcan/apchemistry/cool_phase_changes_diagram.html

50. Askeland. (1994). *The Science and Engineering of Materials, Third Edition*. PWS Publishing Company

51. Ryzhkin & Petrenko. (1997). Physical mechanisms responsible for ice adhesion. *Physics and Chemistry of Ice 1996, 101*(32) 6267-70.

52. Dalili et al. (2009). A review of surface engineering issues critical to wind turbine performance. *Renewable and Sustainable Energy Reviews, 13*(2), 428-38.

53. Koleske. (1995). Paint and Coating Testing Manual: Fourteenth Edition of the Gardner-Sward Handbook. (pp. 89-95) The American Society for Testing and Materials

54. PPG, AUE-50000. (2009). Series wind turbine polyurethane topcoat. Retrieved May 23, 2011, from www.ppgcommercialcoatings.com

55. Khanna. (2008). *High Performance Organic Coatings*. (pp. 20-26) Woodhead and Maney Publishing

56. Hare. (1994). *Protective Coatings: Fundamentals of Chemistry and Composition*. (pp. 239-265) Technology Publishing Company

57. Riihe et al. (1993). Structure and Tribological Properties of Ultrathin Alkylsilane Films Chemisorbed to Solid Surfaces *Langmuir* 9, 2383-2388 2383

58. Formanek et al. (2006). Selective electroless plating to fabricate complex three-dimensional metallic micro/nanostructures *Applied Physics Letters* 88

59. Ahn & Roper. (2010). Periodic Nanotemplating by Selective Deposition of Electroless Gold Island Films on Particle-Lithographed Dimethyldichlorosilane Layers. *ACS Nano* 4(7), 4181–4189

60. Barberoglou et al. (2009). Bio-inspired water repellent surfaces produced by ultrafast laser structuring of silicon. *Applied Surface Science, 255*(10), 5425-9.

61. Mele et al. (2006). Polymeric distributed feedback lasers by room-temperature nanoimprint lithography. *Applied Physics Letters, 89*(13), 131109-131109-3.

62. Tang et al. (2008). Hydrophobic surface fabrication by laser micropatterning. *2008 IEEE PhotonicsGlobal@Singapore (IPGC)*, 4.

63. Zhou et al. (2010). Femtosecond laser induced superhydrophobic transformation on metal surface. *4th Pacific International Conference on Applications of Lasers and Optics, PICALO 2010, March 23, 2010 - March 25,*

64. Sun et al. (2005). Artificial Lotus Leaf by Nanocasting. *Langmuir 21,* 8978-8981

65. Lääniläinen. (2006). Soft Lithography for Surface Micropatterning

66. Yu et al. (2004). Measurement of parameters of tracks in CR-39 detector from replicas. *Radiat Prot Dosimetry 111(1): 93-96*

67. Thapa et al. (2003). Polymers with nano-dimensional surface features enhance bladder smooth muscle cell adhesion. *J Biomed Mater Res 67A*: 1374-1384

68. Chun et al. (2009). The role of polymer nanosurface roughness and submicron pores in improving bladder urothelial cell density and inhibiting calcium oxalate stone. *Nanotechnology* 20, 085104 (8pp)

69. Iopara inc. Retrieved May 23, 2011, from http://iopara.ca/softwares.html

70. Vereisung. Retrieved May 23, 2011, from http://www.meteotest.ch/en/business_fields/wind_energy/research/

71. Mills. (1998). *Heat Transfer*. Prentice Hall

Appendix A: Description of Research for Popular Publication

Engineering Following Nature

By: Clayton Schenk

Nature is the tenured faculty member in the science of life. Nature is able to develop solutions through the evolution of all species. Nanotechnology isn't a new subject for nature. A peacock has some of the most bright and beautiful features, developed through natures understanding of the zinc oxide nanoparticles band gap structure. Think structural design for nature is a problem? Trees have a novel design of a strong thick base that branch out to gain maximum sunlight. Wetting and self cleaning surfaces, no problem for nature! A lotus leaf grows in the ponds and lakes and is still not wet and very clean. Based on a superhydrophobic surface texture on the micro-nano scale, the lotus leaf propels the water from the surface which picks up dirt as it rolls off. Nature has tested and given us many creations that we should be as smart to imitate in design.

The question is why not design everything like nature? The answer is that nature doesn't have to worry about reliability of its creation. If one doesn't perform, there will be 10 more to take its place. Furthermore, humans require many different boundary conditions than nature, thus limiting the available solutions. However, there are many fundamental ideas that can be used. In the instance of a tree design, engineers have imitated this in the capping of oil wells at the subsea levels. For the simple reason, it is the most efficient way to funnel the high pressure of the oil from the well. Recently, the lotus leaf is being explored at the University of Arkansas. A surface texture on a lotus leaf inspired polyurethane surface maintains some of the same qualities.

The lotus leaf microscopic pillar like structures doesn't allow the water to stay in contact with the surface, says Clayton Schenk, a Master of Science student at the University of Arkansas. "When water touches the surface, the water remains in contact with only the tops of the pillars," Schenk says, "this is the unique nature's creation."

How have science and engineers further the understanding as from nature's creation? A study of heat transfer and the lotus leaf led to one such discovery. A lotus repels water by propelling the droplet from the surface. Can this be applied for anti-icing coatings? According to Fourier Law, a component of conduction is controlled by area of contact. Thus, creation of a surface similar structure to the lotus will limit the contact of water to the surface. Researchers have shown under laboratory conditions that indeed the ice formation onto such a surface can be delayed up to 80%!

The implementation of the surface texture has potential for a wide range of application. A similar surface texture could be used in painting projects for self cleaning. Or providing wind turbine blades with the ability to stay unfrozen.

Appendix B: Executive Summary of Newly Created Intellectual Property

The following list of new intellectual property items were created in the course of this research project and should be considered from both a patent and commercialization perspective.

1. A process based on soft lithography for forming micron sized features on the PU surface. The combination of materials chosen and methods utilized was novel.

Appendix C: Potential Patent and Commercialization Aspects of listed Intellectual Property Items

C.1 Patentability of Intellectual Property

There is no patentable intellectual property from this work.

C.2 Commercialization Prospects

There are no commercialization prospects from this work.

C.3 Possible Prior Disclosure of IP

On November 1st 2010, the idea of soft lithography was presented to the microEP community during a class presentation. The combination of materials and methods were not disclosed, rather it was presented as a concept to form superhydrophobic surfaces as explored by other researchers.

Appendix D: Broader Impact of Research

D.1 Applicability of Research Methods to Other Problems

The presented research problem and solution is present to solve the problem of icing accreditation on wind turbine blades. The initial idea of imprinting polymers to create different surface textures could have potential uses from the electronics industry to various other particular problems. Although the main polymer focus in this paper is polyurethane, it was experimentally found that PDMS can replicate sub micron features. Other materials that have the same basic viscous liquid to solid polymerization curing process can potentially have similar replication ability.

D.2 Impact of Research Results on U.S. and Global Society

The presented research has the potential to benefit and advance coating technologies by allowing multifunctional coatings from the modification of the surface structure. Further research, may lead to an easy application of a similar creation of a micro structure by roller based technology and widespread application to all coating technologies.

D.3 Impact of Research Results on the Environment

The creation of a tailored micro/nano-structured surface for wind turbines will allow the improved efficiency for continuous power generation. Adding functionality based on a surface texture poses no immediate harm to the environment.

Appendix E: Microsoft Project for MS MicroEP Degree Plan

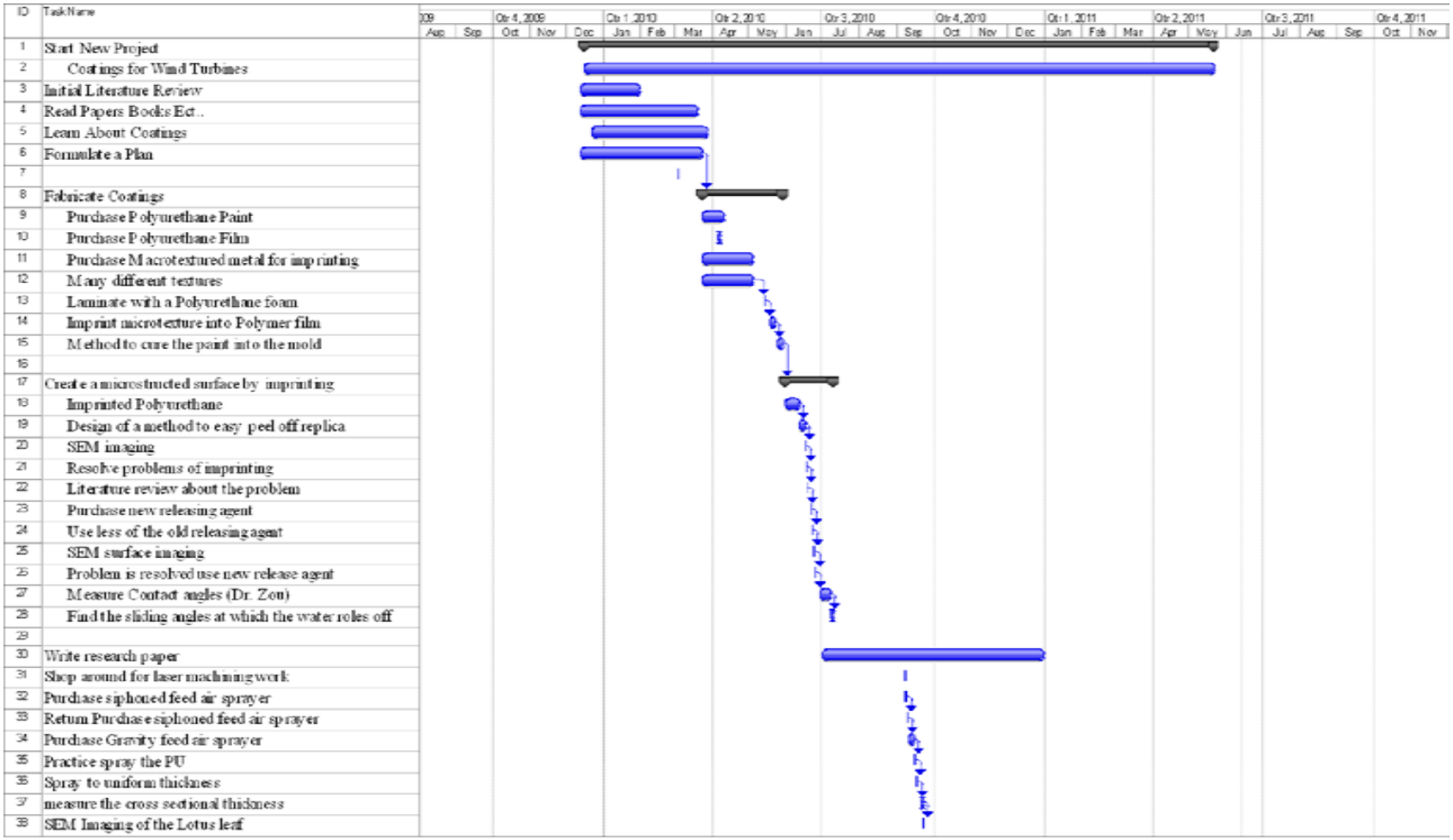

ID	Task Name
1	Start New Project
2	Coatings for Wind Turbines
3	Initial Literature Review
4	Read Papers Books Ect..
5	Learn About Coatings
6	Formulate a Plan
7	
8	Fabricate Coatings
9	Purchase Polyurethane Paint
10	Purchase Polyurethane Film
11	Purchase Macrotextured metal for imprinting
12	Many different textures
13	Laminate with a Polyurethane foam
14	Imprint microtexture into Polymer film
15	Method to cure the paint into the mold
16	
17	Create a microstructed surface by imprinting
18	Imprinted Polyurethane
19	Design of a method to easy peel off replica
20	SEM imaging
21	Resolve problems of imprinting
22	Literature review about the problem
23	Purchase new releasing agent
24	Use less of the old releasing agent
25	SEM surface imaging
26	Problem is resolved use new release agent
27	Measure Contact angles (Dr. Zou)
28	Find the sliding angles at which the water roles off
29	
30	Write research paper
31	Shop around for laser machining work
32	Purchase siphoned feed air sprayer
33	Return Purchase siphoned feed air sprayer
34	Purchase Gravity feed air sprayer
35	Practice spray the PU
36	Spray to uniform thickness
37	measure the cross sectional thickness
38	SEM Imaging of the Lotus leaf

Figure E 1. Coatings for wind turbine blades project file. Tasks: 1-38

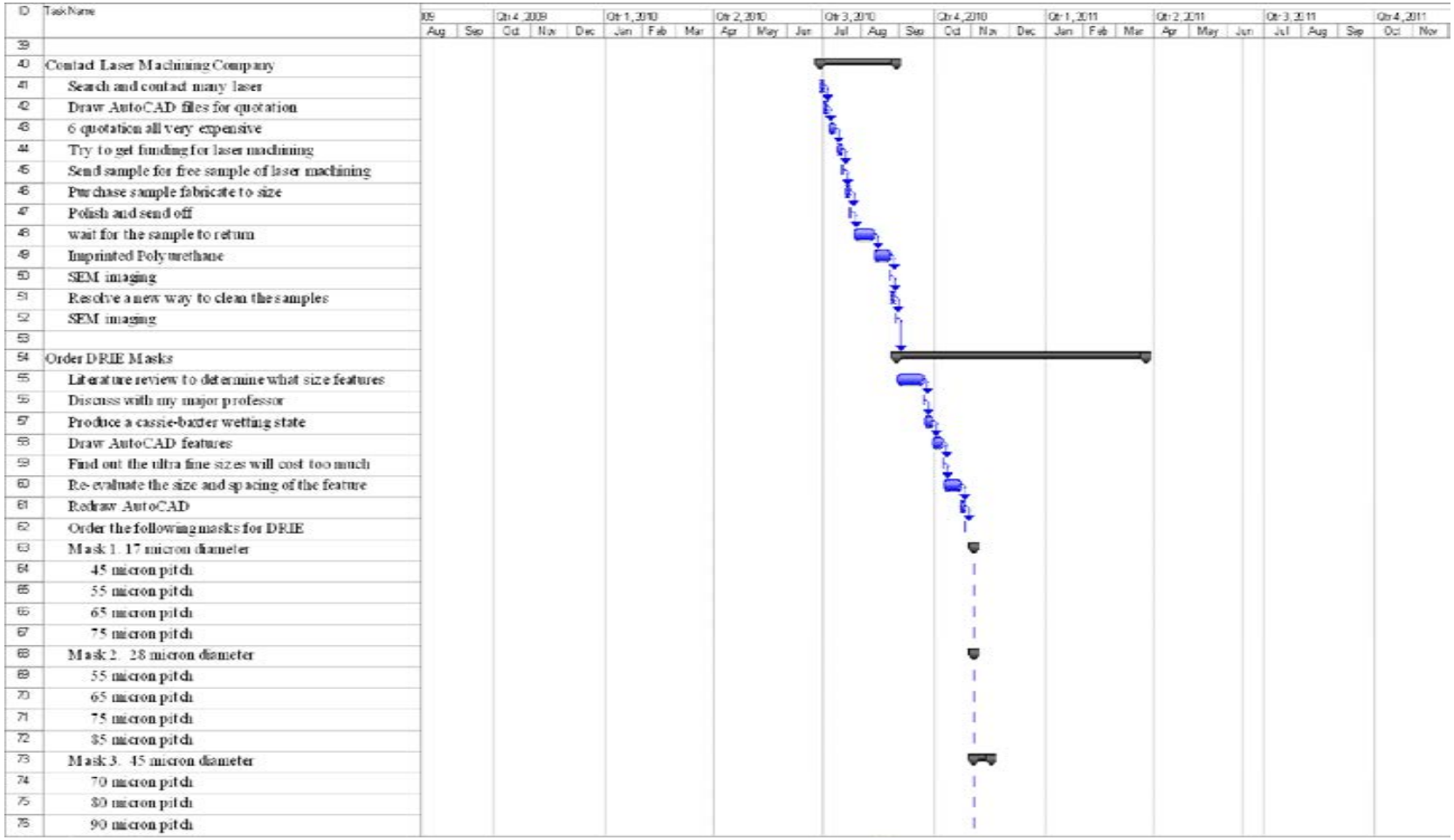

ID	Task Name
39	
40	Contact Laser Machining Company
41	Search and contact many laser
42	Draw AutoCAD files for quotation
43	6 quotation all very expensive
44	Try to get funding for laser machining
45	Send sample for free sample of laser machining
46	Purchase sample fabricate to size
47	Polish and send off
48	wait for the sample to return
49	Imprinted Polyurethane
50	SEM imaging
51	Resolve a new way to clean the samples
52	SEM imaging
53	
54	Order DRIE Masks
55	Literature review to determine what size features
56	Discuss with my major professor
57	Produce a cassie-baxter wetting state
58	Draw AutoCAD features
59	Find out the ultra fine sizes will cost too much
60	Re-evaluate the size and spacing of the feature
61	Redraw AutoCAD
62	Order the following masks for DRIE
63	Mask 1. 17 micron diameter
64	45 micron pitch
65	55 micron pitch
66	65 micron pitch
67	75 micron pitch
68	Mask 2. 28 micron diameter
69	55 micron pitch
70	65 micron pitch
71	75 micron pitch
72	85 micron pitch
73	Mask 3. 45 micron diameter
74	70 micron pitch
75	80 micron pitch
76	90 micron pitch

Figure E 2. Coatings for wind turbine blades project file. Tasks: 39-78

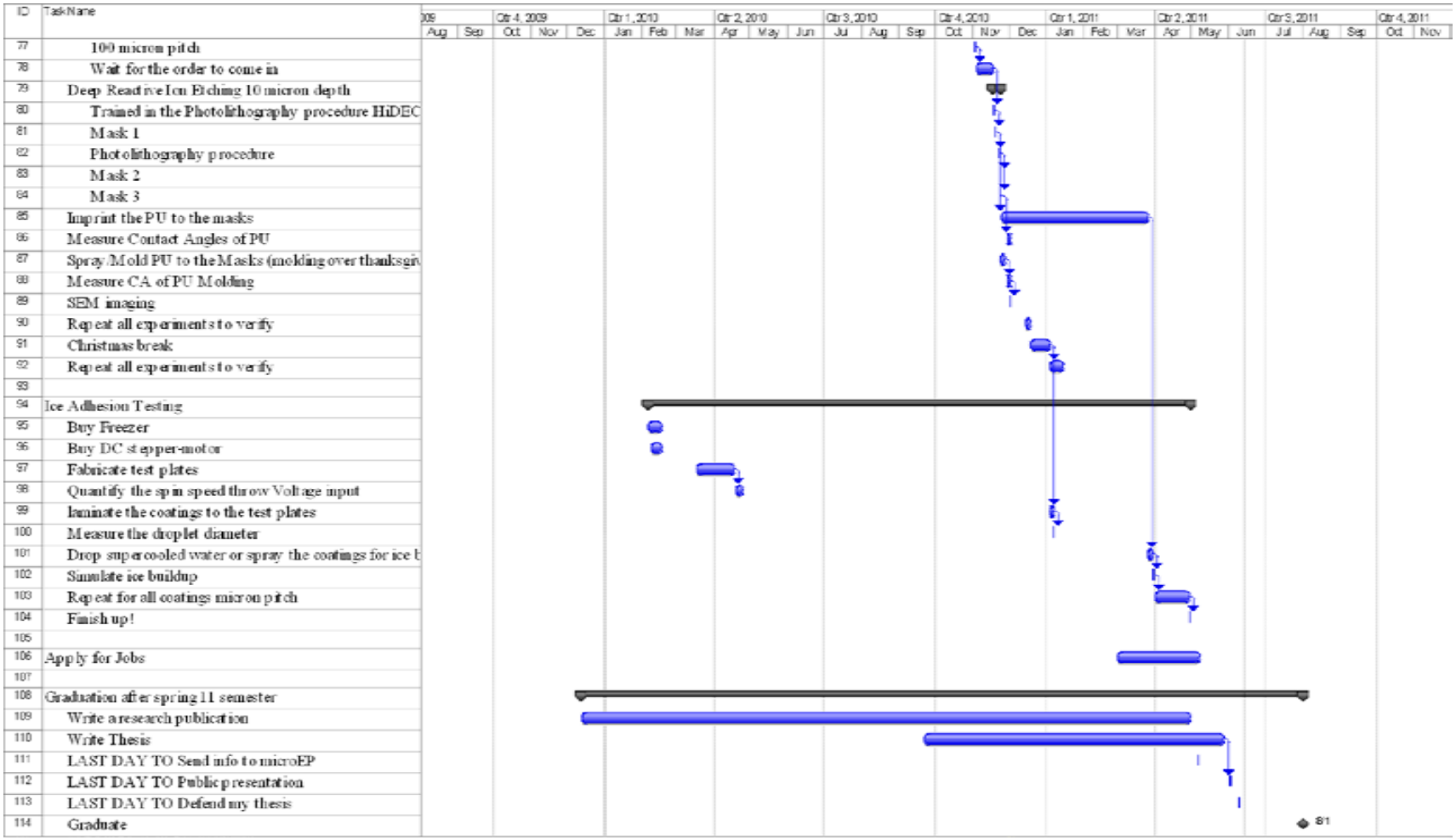

Figure E 3. Coatings for wind turbine blades project file. Tasks: 79-114

Appendix F: Identification of All Software Used in Research and Thesis Generation

Computer #1:
- Model Number: ASUS U81A
- Serial Number: 100583420341
- Location: Home Laptop
- Owner: Clayton Schenk

Software #1:
- Name: Microsoft Office Student 2007
- Purchased by: Clayton Schenk

Software #2:
- Name: Microsoft Project 2007
- Purchased by: University of Arkansas Site License

Software #3:
- Name: AutoCAD 2011
- Purchased by: Free Student Addition

Software #4:
- Name: Symyx Draw 4.0
- Purchased by: Free Version

Computer #2:
- Model Number: Dell 3TQKTH1
- Serial Number: 8328507445
- Location: Engineering Research Center University of Arkansas
- Owner: University of Arkansas (Dr. Ajay Malshe)

Software #1:
- Name: Solid Works
- Purchased by: University of Arkansas Mechanical Engineering Site License

Software #2:
- Name: Buehler Omnimet 9.0
- Purchased by: University of Arkansas (Dr. Ajay Malshe)

Computer #3:
- Model Number: Veeco
- Serial Number: 504120004
- Location: Engineering Research Center University of Arkansas
- Owner: University of Arkansas (Dr. Ajay Malshe)

Software #1:
- Name: Nanoscope
- Purchased by: University of Arkansas (Dr. Ajay Malshe)

Computer #4:

Model Number: Veeco
Serial Number: 20350
Location: Physics Building University of Arkansas
Owner: University of Arkansas (Dr. Gregory Salamo)

Software #1:

Name: Dektak 3
Purchased by: University of Arkansas (Dr. Gregory Salamo)

Computer #5:

Model Number: Dell Precision T3400
Serial Number: 27352389061
Location: Engineering Research Center University of Arkansas
Owner: University of Arkansas (Dr. Min Zou)

Software #1:

Name: SCA 202
Purchased by: University of Arkansas (Dr. Min Zou)

Appendix G: All Publications Published, Submitted and Planned

Publishing the results in Surface and Coatings Technology of the surface modified PU creation and WCA measurements is planned once the manuscript is finished.